WAVES AND SCALES IN HETEROGENEOUS ROCKS

A DISSERTATION
SUBMITTED TO THE DEPARTMENT OF GEOPHYSICS
AND THE COMMITTEE ON GRADUATE STUDIES
OF STANFORD UNIVERSITY
IN PARTIAL FULFILLMENT OF THE REQUIREMENTS
FOR THE DEGREE OF
DOCTOR OF PHILOSOPHY

By
Tapan Mukerji
August 1995

Abstract

The application of Rock Physics for the management of subsurface resources involves relating geophysical observables to physical properites of rocks and pore fluids. Seismic waves are used extensively to image the subsurface, and seismic observables such as traveltimes and velocities are interpreted in terms of rock properties of interest such as lithology, porosity, pore fluids, and conditions of saturation. The subsurface shows significant spatial heterogeneity in rock properties, and these heterogeneities exist over a broad range of scales. In heterogeneous rocks, scattering effects can cause seismic waves to be dispersive, with short wavelength velocities usually being faster than long wavelength velocities. Apart from heterogeneities, the viscoelastic effect of pore fluids can also give rise to velocity dispersion. Seismic waves at different frequencies travel with different velocities depending on the fluid effects, and the scale of the heterogeneities. Therefore an important issue for seismic imaging and interpretation is that the inferred velocities depend not only on the rock and fluid properties, but also on the scale and frequency of measurement. It becomes essential to understand and unravel the frequency-dependent fluid effects and the scale-dependent scattering effects, in order to integrate measurements made at widely varying frequencies and scales. The dissertation is a contribution towards this goal.

A simple technique is presented to relate high-frequency to low-frequency seismic velocity in saturated, anisotropic rocks. The two limits depend on the degree of isolation of cracks and pores with respect to fluid flow. At very low frequencies, the fluid can flow and equilibrate the wave induced pore pressure gradients. At very high frequencies, regions of unequilibrated pore pressures are isolated with respect to fluid flow, making the rock stiffer and increasing the wave velocity. The formulation avoids assumptions of idealized

crack geometries, and hence limitations of low crack densities, by utilizing the measured pressure dependence of dry rock compliances which automatically incorporates all crack interactions. The velocity is found to depend on the frequency, distribution of soft, crack-like porosity, intrinsic anisotropy, fluid compressibility, and effective pressure.

The scale-dependence of velocities in heterogeneous rocks is investigated by studying wave propagation in one-dimensional stratified media, and in two- and three-dimensional random heterogeneous media. The simplest example is that of normal incidence propagation in periodically layered media. Laboratory observations and numerical modeling confirm that measurable arrival times and velocities are controlled by λ/d, the ratio of wavelength to layer spacing. Velocities are faster in the short wavelength limit than in the long wavelength limit. The two limits may be explained by ray theory and effective medium theory. This is the difference between averaging seismic slownesses, in the short wavelength limit (ray theory), and averaging elastic compliances in the long wavelength limit (effective medium theory). In randomly layered media, with a distribution of scales or layer thicknesses relative to the wavelength, neither ray theory nor effective medium theory can accurately explain observed propagation times. A simple practical recipe that successively filters the medium using a running effective medium average, and then applies ray theory appears to accurately estimate the arrival time when neither ray nor effective medium theories can be used. This can be useful for upscaling velocities and traveltimes over a range of scales such as from logs to surface seismics.

In 2- and 3-dimensional heterogeneous media, in addition to the 1-dimensional scale effects, there is a further velocity shift at short wavelengths due to the path effect. Short wavelengths tend to diffract around the slower heterogeneities, biasing the traveltimes to lower values. The slowness inferred from the mean traveltime is smaller than the mean slowness of the random medium. This effect increases from two to three dimensions because of the increased choice of paths for minimizing the traveltime. The variance and correlation of the traveltime fluctuations contain information about the spatial variability of the heterogeneous medium. The short and long wavelength limits are modeled using results from asymptotic ray theory and effective medium theory, and numerical simulations

are used to study the transition between them. The theoretical predictions compare favorably with numerical simulations and with laboratory observations.

Depending on the scales of heterogeneities, and wave frequencies, different situations will require different interpretations of seismic waves.

Acknowledgements

The work described in the following pages was supported by the Stanford Rock and Borehole Geophysics Project (SRB), the Department of Energy, and the Gas Research Institute. For the first two years I was supported by the C. H. Green Fellowship. I wish to thank the members of my dissertation reading committee—Gary Mavko, Amos Nur, Norm Sleep, and Greg Beroza—for their guidance, helpful comments, and advice. I admire Amos Nur for creating SRB, and sincerely thank him for enticing me to Stanford, and for introducing me to my advisor and friend, Gary Mavko.

This dissertation is based on Gary's inspiration and has benefitted greatly from his insight, ideas, guidance, knowledge, and specially his threats—without his prodding it might never have been written. It gives me great pride and pleasure to be Gary Mavko's first Ph.D. student. Smarter ones may come and brilliant ones may go, but no one else will be the first! I specially wish to thank Gary for allowing me to work on many different problems and letting me take as many courses as I wanted (though towards the end I had to furtively shuffle incognito from class to class). Gary is all I could ever hope for in an advisor and teacher. However, when one of our papers gets clobbered by reviewers, we run to Amos. Thanks, Amos, for holding our hands.

Many of our research formulations started as half-baked, fuzzy speculations over pizzas—half Stromboli, half Hawaiian, but not half-baked—at Ramona's Too (by the way, their calzones aren't bad either). As we investigated the different scales of heterogeneity on the pizza toppings, Gary taught me rock physics research while I imparted to him the old Indian hot pepper trick. I enjoyed those crazy discussions. Thanks for the good times, Gary. My unending gratitude also to Dr. Barbara Mavko for her patience when I shifted gears, and for providing, during critical times of need, the absolute essentials for survival—pies, cookies,

and stuff.

Stanford and SRB are a slice of heaven, and Margaret Muir ensures that they remain so. She is a marvel at taking care of emergencies—keeping the printers fed with toner, getting computer supplies, arranging SRB parties, and handling all the administrative details. If you ever have problems with an administrative office at Stanford, sic Margaret on 'em. My sincere thanks to Margaret for her sound advice, academic and non-academic.

During my graduate studies at Stanford, my thoughts have been shaped and sharpened by many wonderful professors, by their courses, and their teaching styles. In the School of Earth Sciences I would like to mention (apart from Gary, who is a really entertaining lecturer, and Amos who tells a good story) Paul Segall, Jerry Harris, Mike McWilliams, Dave Pollard, Tom Hewett, André Journel, Keith Loague, and Steve Gorelick. Some good professors from other departments whose lectures I have enjoyed include Profs. Barnett, Ferziger, Moin, and late Prof. Simo from Mechanical Engineering, Profs. Bracewell, Gray, Inan, and Fraser-Smith from Electrical Engineering, Prof. Kitanidis from Civil Engineering, Prof. Homsy from Chemical Engineering, Prof. McCormack from Aero and Astro, and Prof. Fetter from Physics. Try their courses, you will like them. But above all I deeply acknowledge Prof. Joe Keller's wonderful, lucid, and succinct expositions of the methods of applied mathematics and wave propagation. A whole new world!

My graduate years at Stanford were made enjoyable by many other people, a few good friends, others allegedly so, and some amongst them deserve special mention—those who were lucky enough to be my officemates. The wild three, Nathalie Lucet, Diane Jizba, and Oona Scotti; Laura Alfonsi with her stress tensors and tiramisu; Hezhu Yin, who showed me how to cut cores and squeeze bits of rocks in the pressure vessel; Xina Chan, Li Teng, and Madhumita Sengupta who made sure I saw the dolphins and not just the rocks at Marine World. For brief periods I also shared office space with Yizhak Macovsky and Ran Bachrach, but what can one say about them? The less said the better—though Ran will argue with his version of the wave equation why that is not right. Special thanks to Xina for being such a cheerful friend, bringing in the comics section when needed, and helping me to remember Maxwell's equations. She was also a great help in deciphering complicated social mores, from green eggs and ham to ties and suits and tips and boots.

Words aren't enough to express my gratitude to my family members—amongst many

other things, to my Dad for teaching me Math in school, and to my Mom and sister for helping me to understand a little about transient and steady states. I got my love of Physics from my granddad, who showed me the everyday world through the lens of science, while my grandma—who has a healthy disrespect for all "academic" research, and can always tell when granddad is bluffing—gave me useful insights and tips about everyday life and Indian cooking.

Many of you will probably care to read only the acknowledgements section. I hope you enjoyed it. (You better! It almost took me more time to write than to put together the rest of the chapters). To those who would like to venture further, any resemblance to reality is purely intentional, and what might appear to be bugs in the derivations are obviously "features". Finally, the last, and definitely the least, for keeping me warm and comfortable during the cold winter nights, I thank the Pacific Gas and Electric Company.

Contents

List of Tables

List of Figures

Chapter 1

INTRODUCTION

The Earth's subsurface is heterogeneous over a broad range of scales. Seismic methods provide the primary geophysical tools for detecting and imaging subsurface heterogeneities. These heterogeneities include variations in lithology, porosity, pore fluid properties, and conditions of saturation, pore pressure, temperature, and stress. They occur over a broad range of scales, from submillimeter grain and pore scale, to the many-kilometer basin scale. Similarly, seismic measurement scales and frequencies range from high frequency, millimeter wavelengths in ultrasonic laboratory measurements, to tens of meters in low frequency surface seismic. An important issue for interpreting geophysical images is that the seismic wave propagation is itself affected in various ways by the heterogeneities. For example, seismic arrival times, from which velocities are determined, depend on the scale of heterogeneities relative to the seismic wavelength. Seismic velocities are also sensitive to the presence of pore fluids. Pore fluids tend to stiffen the rock, and give rise to velocity dispersion—seismic velocities in saturated rocks depend on the frequency. Velocity dispersion can also arise due to wave scattering in the presence of heterogeneities.

To be able to interpret and integrate measurements at different scales and widely varying frequencies, it is therefore important to understand both the frequency-dependent fluid effects, and the scale-dependent scattering effects on wave velocities. The rock physics relations between seismic observables and rock properties are frequency- and scale-dependent.

Chapter 2 focuses on the effect of pore fluids on seismic velocities and their frequency

dependence in anisotropic rocks. The dominant fluid mechanism for velocity dispersion in most crustal rocks is the local flow or "squirt" mechanism (Mavko and Nur, 1975; O'Connell and Budiansky, 1977). Fluid effects due to squirt are enhanced in the presence of cracks, and aligned cracks also give rise to seismic anisotropy. Consequently great care must be taken when interpreting observed velocity anisotropy; measurements at low frequencies, typical of insitu observations, will generally be different than at high frequencies, typical of the laboratory. For cracked media saturated with fluid, it is very important to differentiate the two limits or regimes of behaviour depending on the degree of isolation of the cracks with respect to fluid flow: a) low frequency or isobaric behaviour when the fluid may flow and equilibrate the pressure gradients induced by the passing wave, and b) high frequency or adiabatic behaviour when regions of unequilibrated pore pressures are effectively isolated with respect to fluid flow. The unequilibrated pore pressures always makes the rock stiffer in both compression and shear than the isobaric case.

A simple new technique is presented for predicting the high and low frequency saturated velocities in anisotropic rocks entirely in terms of measurable dry rock properties, without the need for idealized crack geometries. At low frequencies, our results reduce to those of Brown and Korringa (1975), which are an anisotropic extension of Gassmann's (1951) relation. At the high frequency limit, the saturated velocities depend on the distributions of crack orientation and crack compliances, and can be related to the change of dry rock compliance with pressure. This is an extension and generalisation of previous results for the isotropic case (Mavko and Jizba, 1991). Measurements of dry velocity vs. pressure and porosity vs. pressure contain all of the necessary information for predicting the frequency-dependent effects of fluid saturation. Furthermore, these measurements automatically incorporate all pore interaction, so there is no limitation to low crack density. The velocities are found to depend on five key interrelated variables: frequency, the distribution of compliant crack-like porosity, the intrinsic or non-crack anisotropy, fluid compressibility, and effective pressure. The theoretical predictions of high frequency saturated velocities compare favourably with laboratory measurements on transversly isotropic sandstone. This chapter has been published in Mukerji and Mavko (1994).

Chapter 3 addresses the simplest example of scale-dependence of velocity in heterogeneous media: 1-dimensional, normal incidence wave propagation in periodically layered media. Wave propagation in stratified media may be explained by ray theory, effective medium theory, or scattering theory depending on the scales of wavelength and layer spacing. A joint experimental and theoretical study was conducted to investigate velocity behavior at the transition from ray theory to effective medium theory in stratified media, and to understand the domain of applicability of long and short wavelength behavior.

The importance of distinguishing the two domains—ray theory (short wavelength) and effective medium (long wavelength)—and understanding the transition between them arises from the fact that one of the key issues in reservoir characterization is the assigning of appropriate average values of seismic velocities to the various sub-units of layers that make up the reservoir. Depending on scales of layering and wave frequencies, different situations will require different interpretations.

The laboratory measurements were made at Elf-Aquitane (Marion and Coudin, 1992). Velocity measurements were performed at 50 and 500 kHz on periodic media composed of steel and plastic discs. The ratio of wavelength to layer spacing, λ/d, spanned more than two orders of magnitude between 0.1 and 50. Our results confirm that velocities in stratified media are controlled by the ratio of wavelength to layer spacing. Velocities in the short wavelength limit are generally faster than velocities in the long wavelength limit. We find that the transition from ray to effective medium approximations occurs over a narrow range of λ/d at a value of about 10. The transition region of $\lambda/d \approx 10$ is consistent with predictions of scattering theory in one-dimensional layered media (Tang and Burns, 1992), and previous results, obtained experimentally (Melia and Carlson, 1984) and numerically (Carcione et al., 1991). Our numerically simulated waveforms are in close agreement with the experimentally observed delayed first arrival in the long wavelength limit and reduced amplitudes at the transition from short to long wavelength regime. This chapter was published as Marion et al. (1994).

Chapter 4 extends the results of chapter 3 to normal incidence wave propagation in randomly layered media. Randomly stratified media can have a distribution of scales or layer

thickness. Hence, at each point the wave propagation may not be describable with a single λ/d. Laboratory experiments on stacks of steel and plastic disks simulating a VSP were carried out by Dominique Marion at Elf-Aquitane. Analyses of the laboratory observations, and further studies on numerically generated randomly layered media were carried out in collaboration with Philippe Rio at Stanford.

Our laboratory-simulated VSP and numerical experiments show that neither ray nor effective medium theories can accurately explain wave propagation times in a randomly layered medium with a wide range of layer thicknesses relative to the seismic wavelength. We highlight some scale-related pitfalls of log and VSP interpretation and give a simple practical technique for upscaling travel-times and velocities over a range of scales—for example, when upscaling from logs to surface seismic and VSP. In practice, wave propagation in layered media is dispersive, ranging between the fast, short wavelength limit described by ray theory and the slower, long wavelength limit described by effective medium theory. Stratigraphic filtering methods, based on a stochastic description, such as those presented by Banik et al. (1985) and Shapiro et al. (1994), can account for the average dispersion over a very long path length, but cannot account for observed local fluctuations, such as a speed up when layers are thick and a slow down when thin. Furthermore, many of these formulations are limited to small material contrasts. A more flexible approach follows from the invariant imbedding formulation of Kennett (1974) and Frazer (1994). We have shown that this can predict quite well the laboratory-simulated VSP, as well as numerically-simulated travel times in Poisson, Gaussian, and fractal randomly layered media. A simple approximate recipe for predicting the scale-dependent travel time is suggested by successively filtering the medium using a running Backus average and then applying ray theory. It appears to accurately estimate the seismic arrival time when neither ray theory nor effective medium theory can be used, and predicts quite well both the laboratory and numerically-simulated travel times and velocity dispersion.

Finally, chapter 5 investigates scale-dependent velocity dispersion and scattering in 2- and three-dimensional random heterogeneous media. Again in general, the velocity inferred from arrival times is slower when the wavelength is longer than the scale of heterogeneity and faster when the wavelength is shorter. As shown in chapters 3 and 4, for normal

incidence propagation in stratified media, this is the difference between averaging seismic slownesses, in the short wavelength limit, and averaging elastic compliances, in the long wavelength limit. In two and three dimensions there is an additional increase in velocities at short wavelengths due to the path effect (Boyse, 1986; Roth et al., 1993). Shorter wavelengths tend to find faster paths, thus biasing the traveltimes to lower values. In the short wavelength limit, the slowness inferred from the average traveltime is smaller than the mean slowness of the medium. When the propagation distance is much larger than the scale of the heterogeneity, the path effect causes the velocity increase from long to short wavelength to be much larger in two dimensions than in one dimension, and even larger in three dimensions.

We investigated the scale dependence of measurable seismic velocities using finite-difference simulations of acoustic wave propagation in 2-dimensional random media. Daniel Mujica collaborated in the initial stages of this work. We show that the asymptotic ray theoretical results of Boyse (1986) can be used to predict observed velocity shifts at short wavelengths in 2- and 3-dimensional random heterogeneous media. The 2-dimensional simulations agree reasonably well with the theoretical predictions for 2-dimensional media while the predictions for three dimensions are consistent with observations in 3-dimensional laboratory samples. The long wavelength limit is modeled by effective medium theories (Berryman, 1980).

The velocity in random heterogeneous media depends on the variance of the fluctuations of the medium, its spatial autocorrelation, the seismic wavelength, and the path length. The predicted short wavelength velocity in three dimensions is faster than in two dimensions, which is, in turn, faster than in one dimension.

The numerical simulations also confirm the spatial fluctuations in traveltime, which can be modeled fairly well in the short wavelength limit using the theory of Müller et al.(1992). The fluctuations have practical implications for recording data and measuring velocities. When the receiver spacing is small enough and the array length is long enough to characterize the fluctuations, then the mean of the traveltimes will yield the fast ray theory velocities predicted by Boyse (1986). Furthermore, the variance of the fluctuations yields information on the slowness variance of the medium. The correlation length of the traveltime fluctuations is a measure of the spatial correlation length of the medium. When arrival

times are picked from the stacked trace, or equivalently the output trace of a large seismic group array or from a large laboratory transducer, then the first-break will tend to be even earlier than the mean traveltime. This chapter has been published as Mukerji et al. (1995).

REFERENCES

Banik, N. C., Lerche, I., Resnick, J. R., and Shuey, R. T., 1985, Stratigraphic filtering, part I & II, Geophysics, **50**, 2768-2783.

Berryman, J. G., 1980, Long-wavelength propagation in composite elastic media II. Ellipsoidal inclusions: J. Acoust. Soc. Am., **68**, 1820-1831.

Boyse, W. E., 1986, Wave propagation and inversion in slightly inhomogeneous media: Ph.D. dissertation, Stanford University.

Brown, R., and Korringa, J., 1975, On the dependence of the elastic properties of a porous rock on the compressibility of the pore fluid: Geophysics, **40**, 608-616.

Carcione, J. M., Kosloff, D., and Behle, A., 1991, Long-wave anisotropy in stratified media: Geophysics, **56**, 245-254.

Frazer, L. N., 1994, A pulse in a binary sediment, Geophys. J. Int., **118**, 75-93.

Gassmann F., 1951, Uber die elastizitat poroser medien: Vier. der Natur Gesellschaft, **96**, 1-23.

Kennett, B. L. N., 1974, Reflections, rays and reverberations, Bull. Seism. Soc. Am., **64**, 1685-1696.

Marion, D., and Coudin, P., 1992, From ray to effective medium theories in stratified media: an experimental study, 62nd Ann. Internat. Mtg., Soc. Expl. Geophys., Expanded Abstracts, 1341-1343.

Marion, D., Mukerji, T., and Mavko, G., 1994, Scale effects on velocity dispersion: from ray to effective medium theories in stratified media, Geophysics, **59**, 161 3-1619.

Mavko, G. and Nur, A., 1975, Melt squirt in the asthenosphere: J. Geophys. Res., **80**, 1444-1448.

Mavko, G. and Jizba, D., 1991, Estimating grain-scale fluid effects on velocity dispersion in rocks: Geophysics, **56**, 1940-1949.

Melia, P. J., and Carlson, R. L., 1984, An experimental test of P-wave anisotropy in stratified media: Geophysics, **49**, 374-378.

Mukerji, T., and Mavko, G., 1994, Pore fluid effects on seismic velocity in anisotropic rocks, Geophysics, **59**, 233-244.

Mukerji, T., Mavko, G., Mujica, D., and Lucet, N., 1995, Scale-dependent seismic velocity in heterogeneous media: Geophysics, **60**, 1222-1233.

Müller, G., Roth, M., and Korn, M., 1992, Seismic-wave traveltimes in random media: Geophys. J. Int., **110**, 29-41.

O'Connell, R., and Budiansky B., 1977, Viscoelastic properties of fluid-saturated cracked solids: J. Geophys. Res., **82**, 5719-5736.

Roth, M., Müller, G., and Sneider, R., 1993, Velocity shift in random media: Geophys. J. Int., **115**, 552-563.

Shapiro, S. A., Hubral, P., and Zien, H., 1994, Frequency-dependent anisotropy of scalar waves in a multilayered medium, J. Seis. Explor., **3**, 37-52.

Tang, X., and Burns, D. R., 1992, Seismic scattering and velocity dispersion due to heterogenous lithology: 62nd Ann. Internat. Mtg., Soc. Expl. Geophys., Expanded Abstracts, 824-827.

Chapter 2

FLUID EFFECTS ON VELOCITY DISPERSION

PORE FLUID EFFECTS ON SEISMIC VELOCITY IN ANISOTROPIC ROCKS

ABSTRACT

A simple new technique predicts the high and low frequency saturated velocities in anisotropic rocks entirely in terms of measurable dry rock properties, without the need for idealized crack geometries. Measurements of dry velocity vs. pressure and porosity vs. pressure contain all of the necessary information for predicting the frequency-dependent effects of fluid saturation. Furthermore, these measurements automatically incorporate all pore interaction, so there is no limitation to low crack density. The velocities are found to depend on five key interrelated variables: frequency, the distribution of compliant crack-like porosity, the intrinsic or non-crack anisotropy, fluid viscosity and compressibility, and effective pressure. The sensitivity of velocities to saturation is generally greater at high frequencies than at low frequences. The magnitude of the differences, from dry to saturated and from low frequency to high frequency, is determined by the compliant or crack-like porosity. Predictions of saturated velocities based on dry data for sandstone and granite show that compressional velocities generally increase with saturation and with frequency. However, the degree of compressional wave anisotropy may either increase or decrease upon saturation depending on the crack distribution, the effective pressure, and the frequency at which the measurements are made. Shear wave velocities can either increase or decrease with saturation, and the degree of anistropy depends on the microstructure, pressure, and frequency. Consequently great care must be taken when interpreting observed velocity anisotropy; measurements at low frequencies, typical of insitu observations, will generally be different than at high frequencies, typical of the laboratory.

2.1 INTRODUCTION

Most crustal rocks are found experimentally to be seismically anisotropic. This is usually understood as a combination of microstructural fabric (Jones, 1983), fine scale layering (Backus, 1962), and aligned microcracks (Nur and Simmons, 1969). Although each of these may be equally important, crack effects have been emphasized most in hydrologic, exploration, and tectonic studies, because of their sensitivity to stress (Nur, 1971; Lockner et al., 1977; Crampin, 1978) and their impact on permeability (Walls, 1983). Nur (1971) showed experimentally that nonhydrostatic stress can induce both P- and S-wave anisotropy in an otherwise isotropic rock, by preferentially closing cracks that are perpendicular or nearly perpendicular to the axis of greatest compression. Lockner et al. (1977) showed that increasing the differential stress to near failure can further increase anisotropy by creating new cracks. Numerous field studies have confirmed fracture-related anisotropy in situ (eg., Alford, 1986; Crampin et al., 1985; Willis et al., 1986; Winterstein and Meadows, 1991; Queen and Rizer, 1990)

Despite this emphasis, surprisingly few experimental (Jones, 1983; Lucet and Tarif, 1988; Tarif, 1986; Zamora and Poirier, 1990) and theoretical (Brown and Korringa, 1975; Hudson, 1980, 1981, 1991) studies exist on the critical anisotropic effects of *pore fluids and pore pressure*, which are most pronounced in cracked rocks.

The sensitivity of seismic velocity to pore fluids, in general, was demonstrated years ago in the laboratory for *isotropic* rocks (Nur and Simmons, 1969), and is the basis for modern direct seismic hydrocarbon detection and EOR monitoring (Nur, 1989). High reflectivity contacts between fluid-saturated and gas-saturated rocks are often detectable as "bright spots" on conventional P-wave stacked sections, and as amplitude vs. offset (AVO) anomalies on prestack data (Ostrander, 1982). High pore pressure (Spencer and Nur,1976; Jones, 1983), perhaps coupled with anisotropy (Lueschen, et al., 1990), may be the key to puzzling low velocity zones in the crust, and low-strength, low velocity fault zones (Raleigh

and Evernden, 1982).

Every one of these fluid effects is enhanced by compliant, crack-like porosity. Therefore, it can clearly be misleading to interpret in situ seismic anisotropy without a complete understanding of pore fluid effects in anisotropic cracked media. This is particularly true when cracks are superimposed on an intrinsically anisotropic mineral matrix.

Most previous analysis techniques (eg., Hudson, 1980, 1981; Crampin, 1984; Thomsen, 1986) for cracked anisotropic rocks share one or more features which can limit their usefulness, particularly when comparing laboratory and field data: (1) they are based on idealized (and unrealistic) crack geometries, such as ellipsoidal cracks, (2) they are therefore intrinsically limited to low crack densities, (3) they often ignore the anisotropic mineral matrix, and (4) Their treatment of frequency-dependent saturation effects is incomplete.

We present here a simple alternative technique for predicting the relation between dry and saturated velocities in anisotropic rocks entirely in terms of *measurable dry rock properties*, without the need for idealized crack geometries. Measurements of dry velocity vs. pressure and porosity vs. pressure contain all of the necessary information for predicting the frequency-dependent effects of fluid saturation. Furthermore, these measurements automatically incorporate all pore interaction, so there is no limitation to low crack density.

We find that the velocities depend on five key interrelated variables:

- Frequency
- The distribution of compliant, crack-like porosity
- The intrinsic or non-crack anisotropy
- Fluid viscosity and compressibility
- Effective pressure

The sensitivity of velocities to saturation is generally greater at high frequencies than at low frequences. The magnitude of the differences, from dry to saturated and from low frequency

to high frequency, is determined by the compliant or crack-like porosity.

At *low frequencies* our results reduce to those of of Brown and Korringa (1975), which are an anisotropic extension of Gassmann's (1951) relations. For *high frequencies*, we present a simple new method for predicting the amount of local flow or "squirt" dispersion (Mavko and Nur, 1975; O'Connell and Budianski, 1977), which is an extension of our previous results for the isotropic case (Mavko and Jizba, 1991).

Using this formulation, we show that velocities and velocity anisotropy in saturated rocks can be quite different at low (in situ) frequencies than at high (laboratory) frequencies. Consequently great care must be used when applying laboratory observations to the field, or when using laboratory observations to validate a model.

2.2 FLUID MECHANISMS

If a set of loads applied to a dry rock cause a decrease in pore volume, then saturating the rock with fluid will usually increase the rock's stiffness under the same set of loads. Under undrained conditions pore compression induces pore fluid pressure, which, in turn, resists the deformation. Gassmann (1951) quantified this for isotropic rocks with a simple expression relating the saturated rock bulk modulus to the dry rock bulk modulus:

$$\frac{1}{K_{dry}} - \frac{1}{K_{sat}} = \frac{(\frac{1}{K_{dry}} - \frac{1}{K_0})^2}{(\frac{1}{K_{dry}} - \frac{1}{K_0}) + \phi(\frac{1}{K_f} - \frac{1}{K_0})}, \tag{2.1}$$

where K_0, K_{dry}, K_{sat}, and K_f are the bulk moduli of the mineral grains, the dry composite, the saturated composite, and the pore fluid, and ϕ is the porosity. This result assumes isotropy, but is otherwise completely independent of pore geometry, and elastic interaction between pores is completely described. The result is limited to low frequencies so that

inertial and scattering effects can be ignored and so that the pore pressure induced by the externally applied compression has time to equilibrate throughout the pore space.

Brown and Korringa (1975) extended Gassmann's relation to anisotropic media:

$$S^{(dry)}_{ijkl} - S^{(sat)}_{ijkl} = \frac{(S^{(dry)}_{ij\alpha\alpha} - S^{0}_{ij\alpha\alpha})(S^{(dry)}_{kl\alpha\alpha} - S^{0}_{kl\alpha\alpha})}{(\beta_{dry} - \beta_0) + (\beta_f - \beta_0)\phi}, \tag{2.2}$$

$$\begin{aligned} \beta_{dry} &= S^{(dry)}_{\alpha\alpha\beta\beta} = 1/K_{dry}, \\ \beta_0 &= S^{0}_{\alpha\alpha\beta\beta} = 1/K_0, \\ \beta_f &= 1/K_f, \end{aligned}$$

where $S^{(sat)}_{ijkl}$ is the predicted saturated rock compliance, while $S^{(dry)}_{ijkl}$ and S^{0}_{ijkl} are the compliances of the dry rock and mineral material. This form again assumes that the frequencies are low, so that the induced pore pressures are everywhere equalized.

Biot's (1956a, b) formulation relaxed some of the requirements of Gassmann's low frequency theory, by including the dynamic coupling of fluid and solid stresses and the effects of contrasting inertial forces in the fluid and solid. The low frequency limit of Biot's formulation for bulk modulus is identical to Gassmann's, and a modest dispersion is predicted at higher frequencies. Biot (1962a, b) later extended this work to anisotropic media.

Measured seismic velocities in saturated rocks at ultrasonic frequencies (Winkler, 1985, 1986) are often much faster than predicted by either the Gassmann or Biot formulations. Both experiments (Murphy et al., 1984; Wang and Nur, 1988, 1990) and models (Mavko and Nur, 1979; O'Connell and Budiansky, 1974, 1977; Mavko and Jizba, 1991; Thomsen, 1985, 1986, 1991) suggest that the cause is related to the grain-scale microscopic flow field, refered to as "local flow" or "squirt" (Mavko and Nur, 1975). For most crustal rocks, particularly those with crack porosity, the Biot dispersion is small compared with squirt

dispersion, and can often be ignored.

To understand the squirt mechanism, consider a saturated rock sample with the pore space vented to zero pore pressure. When an increment of stress is applied to the rock at very low frequencies, pore fluid can easily flow in and out of every pore; the rock behaves as though it is drained, and its moduli are essentially the same as dry rock moduli. At higher frequencies, viscous and inertial effects cause the thinnest pores to be isolated with respect to flow from the larger drained pores, and the external stress induces increments of pore pressure. Stiff portions of the pore space tend to have relatively low induced pore pressure; the compliant pores have relatively high induced pore pressure. The unequilibrated pore pressures make the rock stiffer than at low frequencies.

Our formulation considers the saturated compliant, crack-like fraction of the pore space (which we sometimes also call the soft porosity) to be part of the viscoelastic rock frame (Biot, 1962a,b), separate from the larger, stiffer fraction of the pore space where "global" flow might occur. This is in contrast to the Biot-Gassmann-Brown-Korringa approach, which assumes that pore pressures are uniform throughout the pore space. We call the high frequency limit of this frame the "unrelaxed frame" and label its compliances $S_{ijkl}^{(wet)}$ which are different from $S_{ijkl}^{(sat)}$.

We proceed now to derive expressions for the *unrelaxed frame compliances*, $S_{ijkl}^{(wet)}$, in terms of the dry or relaxed compliance, $S_{ijkl}^{(dry)}$, at the same pressure, and the dry compliance at very high confining pressure, $S_{ijkl}^{(highP)}$. These unrelaxed frame compliances can then be substituted into the Brown and Korringa or Biot formulations in place of the dry compliances to predict $S_{ijkl}^{(sat)}$ and model the total dispersive behavior of the saturated rock.

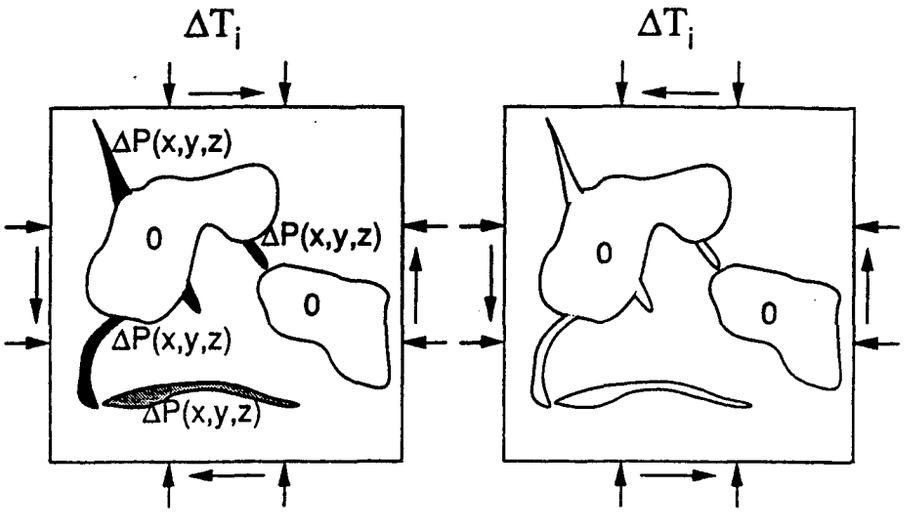

Figure 2.1: Two sets of tractions applied to the same rock sample. The rock on the left deforms with the unrelaxed frame compliance. The rock on the right deforms with the effective dry rock compliances.

2.3 DERIVATION OF UNRELAXED FRAME MODULI

We estimate the effect of the uneven pore pressure distribution on the unrelaxed frame compliance, $S_{ijkl}^{(wet)}$, using the Betti-Rayleigh reciprocity theorem (Walsh, 1965; Jaeger and Cook, 1969). Consider the two sets of tractions applied to a rock with total volume V, as shown in Figure 2.1.

The rock on the left is loaded by externally applied tractions $\Delta T_i = \Delta\sigma_{ij} n_j$, where n is the outward unit normal vector at each point on the surface, and $\Delta\sigma_{ij}$ is an arbitrary constant stress tensor corresponding to the incremental loading of a passing wave. Internally applied normal tractions, $\Delta P(x, y, z)$, (which are equal to the as yet unknown spatially variable incremental pore pressures induced by the wave) are applied to the unrelaxed compliant

fraction of the pore space. Zero internal tractions are assumed on the drained fraction of the pore space. Therefore, it has the appearance of a partially saturated rock with fluid in the thin, compliant pores only, and it deforms with the unrelaxed frame compliance. The rock on the right has the same tractions ΔT_i applied to the external surfaces and zero tractions applied to the internal surfaces, so it deforms with the effective dry rock compliances, $S_{ijkl}^{(dry)}$. Applying the reciprocity theorem, we can write:

$$\Delta\sigma_{ij}\Delta\sigma_{kl}S_{ijkl}^{(dry)}V - \sum_n \Delta P_n \Delta v_n = \Delta\sigma_{ij}\Delta\sigma_{kl}S_{ijkl}^{(wet)}V. \tag{2.3}$$

The summations result from separating the integrals of work done on the pore walls into the sum of integrals over subsets of the pore space having approximately equal induced pore pressure, ΔP_n. Correspondingly, v_n is the volume of that subset of pore space and Δv_n is the dry rock stress-induced change of pore volume.

The volume change Δv_n can be written in terms of an effective dry pore compliance, $W_{ijkl}^{(n)}$ that relates the average strain of the nth piece of pore space to the applied stress:

$$\Delta v_n = W_{\alpha\alpha kl}^{(n)}\Delta\sigma_{kl}v_n. \tag{2.4}$$

The induced pressure in the nth unrelaxed pore can be written as (see appendix):

$$\Delta P_n = \frac{W_{\alpha\alpha ij}^{(n)}\Delta\sigma_{ij}}{W_{\alpha\alpha\beta\beta}^{(n)} + (\beta_f - \beta_0)}, \tag{2.5}$$

where β_f and β_0 are the compressibilites of the pore fluid and of the rock without the soft pores. Combining equations (2.3), (2.4), and (2.5) and taking partial derivatives with respect to $\Delta\sigma_{ij}$ and $\Delta\sigma_{kl}$ leads to:

$$S_{ijkl}^{(dry)} - S_{ijkl}^{(wet)} = \sum_n \frac{\phi^{(n)} W_{\alpha\alpha ij}^{(n)} W_{\alpha\alpha kl}^{(n)}}{W_{\alpha\alpha\beta\beta}^{(n)} + (\beta_f - \beta_0)}, \tag{2.6}$$

where $\phi^{(n)}$ is the porosity of the nth pore. Equation (2.6) expresses the unrelaxed wet frame compliances entirely in terms of the dry rock properties and the pore fluid modulus. Since the low frequency relaxed frame is the same as the dry frame, the difference $S_{ijkl}^{(dry)} - S_{ijkl}^{(wet)}$ is also equal to the frame dispersion.

Following the work of Mavko and Jizba (1991), we now imagine that each piece of soft porosity is locally thin and "crack-like", but has otherwise quite general geometry. If we define local crack coordinate systems with the x_3 axis normal to the crack faces and transform the compliance tensor, $W_{ijkl}^{(n)}$, to that coordinate system, then equation (6) can be written as

$$S_{ijkl}^{(dry)} - S_{ijkl}^{(wet)} = \sum_m \frac{\overline{\phi}^{(m)} \overline{W}_{\alpha\alpha rs}^{(m)} \overline{W}_{\alpha\alpha tu}^{(m)}}{\overline{W}_{\alpha\alpha\beta\beta}^{(m)} + (\beta_f - \beta_0)} \beta_{ir}^{(m)} \beta_{js}^{(m)} \beta_{kt}^{(m)} \beta_{lu}^{(m)}, \tag{2.7}$$

where the $\beta_{ij}^{(m)}$ are the direction cosines between the crack coordinate axes and the global coordinate axes (not to be confused with β_f and β_0, the fluid and mineral compressibilities). We have grouped together into sets all pores having approximately the same orientation, so that $\overline{\phi}^{(m)}$ and $\overline{W}_{rstu}^{(m)}$ now refer to the porosity and average pore compliance of the mth set.

We now take a closer look at the dry pore deformation, $\phi^{(n)} W_{ijkl}^{(n)}$, again using the reciprocity theorem (Figure 2.2). The rock on the left has the same tractions ΔT_i applied to all exterior surfaces, as before. The inside surfaces are traction free, so that the rock deforms with the dry compliances. The rock on the right has the same tractions applied externally and to the inside surfaces of the soft pores, so that it deforms approximately as though the soft pores were not there – as though filled with mineral material, or compressed closed by high confining pressure – with effective high pressure dry compliances, $S_{ijkl}^{(highP)}$. Then we

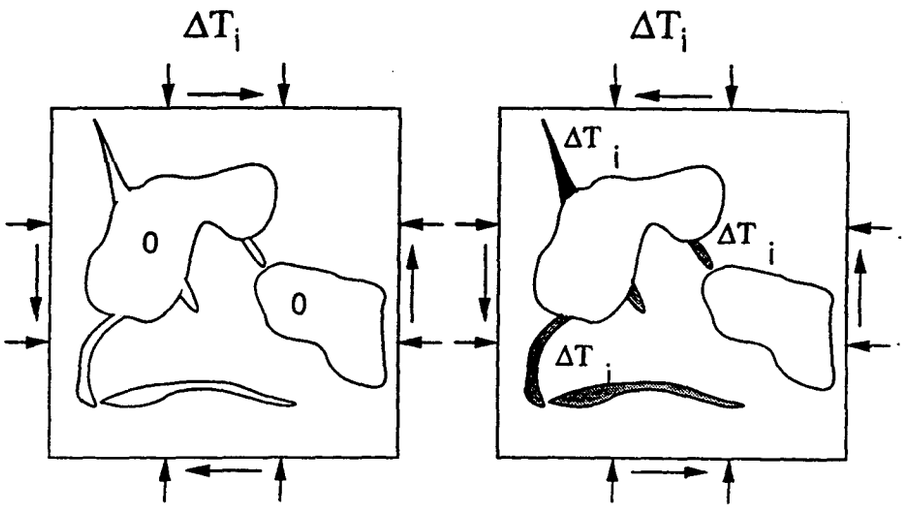

Figure 2.2: Two sets of tractions applied to the same rock sample. The sample on the left deforms with the effective dry rock compliances. The sample on the right deforms with the effective high pressure dry compliances as though the soft pores were compressed closed by high confining pressure.

can write:

$$\Delta\sigma_{ij}\Delta\sigma_{kl}S^{(dry)}_{ijkl}V - \sum_n \Delta\sigma_{ij}\Delta\sigma_{kl}W^{(n)}_{ijkl}v_n = \Delta\sigma_{ij}\Delta\sigma_{kl}S^{(highP)}_{ijkl}V, \tag{2.8}$$

which leads to

$$\Delta S^{(dry)}_{ijkl} = S^{(dry)}_{ijkl} - S^{(highP)}_{ijkl} = \sum_n \phi^{(n)}W^{(n)}_{ijkl}, \tag{2.9}$$

where $\Delta S^{(dry)}_{ijkl}$ is the change in dry compliance between the pressure of interest and very high confining pressure.

In terms of the crack-local coordinate systems, equation (2.9) can be written as

$$\Delta S^{(dry)}_{ijkl} = \sum_m \overline{\phi}^{(m)}\overline{W}^{(m)}_{rstu}\beta^{(m)}_{ir}\beta^{(m)}_{js}\beta^{(m)}_{kt}\beta^{(m)}_{lu}. \tag{2.10}$$

From equations (2.9) and (2.10) we see that, in principle, measurements of the change in dry rock compliances with pressure, $\Delta S^{(dry)}_{ijkl}$, contain information about the dry pore compliances $\phi^{(m)}W^{(m)}_{ijkl}$. When substituted into equations (2.6) and (2.7), they allow us to predict the high frequency, unrelaxed, wet compliances, in terms of the measured dry rock behavior. We illustrate this with examples of isotropic, transversely isotropic, and orthorhombic symmetries.

2.3.1 Isotropic

Approximating the summation in equation (2.10) as an integral over all crack orientations, and noting that for an isotropic rock all pore sets act similarly, equation (2.10) can be written

as:

$$\Delta S_{ijkl}^{(dry)} = \phi_{soft} \overline{W}_{rstu} \frac{1}{4\pi} \int \beta_{ir} \beta_{js} \beta_{kt} \beta_{lu} d\Omega, \tag{2.11}$$

where $\overline{W}_{rstu}$ is the representative average compliance of one crack set, averaged over all crack shapes, including all elastic interactions with the other cracks, and ϕ_{soft} is the total soft porosity – the porosity that closes under high confining pressure. Using this, the change in dry compressibility with pressure can be written as:

$$\Delta S_{\alpha\alpha\beta\beta}^{(dry)} = \phi_{soft} \overline{W}_{\alpha\alpha\beta\beta}. \tag{2.12}$$

To estimate the wet compliances, we similarly approximate the sum in equation (2.7) with an integral over all crack orientations, and use isotropy to bring the porosity and compliances outside of the integral:

$$S_{ijkl}^{(dry)} - S_{ijkl}^{(wet)} = \frac{\phi_{soft} \overline{W}_{\alpha\alpha rs} \overline{W}_{\alpha\alpha tu}}{\overline{W}_{\alpha\alpha\beta\beta} + (\beta_f - \beta_0)} \frac{1}{4\pi} \int \beta_{ir} \beta_{js} \beta_{kt} \beta_{lu} d\Omega. \tag{2.13}$$

For crack-like features we expect the $\overline{W}_{ijkl}$ to be sparse (see appendix), so that equation (13) can be simplified to

$$S_{ijkl}^{(dry)} - S_{ijkl}^{(wet)} \approx \frac{\phi_{soft} \overline{W}_{\alpha\alpha\beta\beta}}{1 + (\beta_f - \beta_0)/\overline{W}_{\alpha\alpha\beta\beta}} \frac{1}{4\pi} \int n_i n_j n_k n_l d\Omega, \tag{2.14}$$

where $\mathbf{n}$ is the unit normal to the crack faces. Values of the tensor $G_{ijkl} = (1/4\pi) \int n_i n_j n_k n_l d\Omega$ are given in Table 2.1. Combining with equation (2.12) gives

Table 1. Values of G^*_{ijkl}.

	ij	11	22	33	23	13	12
kl							
11		$\frac{1}{5}$	$\frac{1}{15}$	$\frac{1}{15}$	0	0	0
22		$\frac{1}{15}$	$\frac{1}{5}$	$\frac{1}{15}$	0	0	0
33		$\frac{1}{15}$	$\frac{1}{15}$	$\frac{1}{5}$	0	0	0
23		0	0	0	$\frac{1}{15}$	0	0
13		0	0	0	0	$\frac{1}{15}$	0
12		0	0	0	0	0	$\frac{1}{15}$

* Elements with any permutation of a given set, $ijkl$, are equal.

Table 2.1: Values of the tensor G_{ijkl} for the case of isotropic symmetry.

$$S^{(dry)}_{ijkl} - S^{(wet)}_{ijkl} \approx \frac{\Delta S^{(dry)}_{\alpha\alpha\beta\beta}}{1 + \phi_{soft}(\beta_f - \beta_0)/\Delta S^{(dry)}_{\alpha\alpha\beta\beta}} G_{ijkl}, \tag{2.15}$$

which shows that the difference between high frequency (unrelaxed) and low frequency (relaxed) frame compliances is a simple function of the change of dry compressibility with pressure. This agrees with the previous results of Mavko and Jizba (1991). Often the soft porosity correction term in the denominator is quite small and may be neglected, so that for practical purposes the above equation may be written as:

$$S^{(dry)}_{ijkl} - S^{(wet)}_{ijkl} \approx \Delta S^{(dry)}_{\alpha\alpha\beta\beta} G_{ijkl}. \tag{2.16}$$

2.3.2 Transversely Isotropic

A critical point to remember is that the measured *dry* compliances $\Delta S_{ijkl}^{(dry)}$ are affected by both the *volumetric* and *shear* components of crack deformation; the amount of the shear vs. volumetric effect depends on the orientation of each crack set relative to the applied field. In contrast, the change in *wet* compliance $\Delta S_{ijkl}^{(wet)}$ is affected only by the decrease in *volumetric* compliance when pore fluid is added. The compressional effect can be seen in equation (2.3) as the crack-by-crack products of pressure increment times volume change, and also in equation (2.6) as the product of volumetric pore strains $W_{\alpha\alpha ij}W_{\alpha\alpha kl}$. To extract only the volumetric part of the dry compliances, it is necessary to carefully treat the crack orientations. For the isotropic case this was very simple, because we assume that all orientations exist. But for anisotropic rocks, we must take more care.

For example, the simplest (though not necessarily correct) model for transversely isotropic rocks assumes that all of the soft, crack-like porosity is parallel. We leave general the crack geometries, crack density, crack interaction, etc. With only this single crack set, equation (10) simplifies to

$$\Delta S_{ijkl}^{(dry)} = \phi_{soft}\overline{W}_{ijkl}. \tag{2.17}$$

Equation (2.7) also simplifies for a single crack set and when combined with equation (2.17) gives

$$S_{ijkl}^{(dry)} - S_{ijkl}^{(wet)} = \frac{\Delta S_{\alpha\alpha ij}^{(dry)}\Delta S_{\alpha\alpha kl}^{(dry)}}{\Delta S_{\alpha\alpha\beta\beta}^{(dry)} + (\beta_f - \beta_0)\phi_{soft}}. \tag{2.18}$$

We now show how the measured dry compliances $\Delta S_{ijkl}^{(dry)}$ can be uniquely decomposed

into their volumetric and shear components for any general transversely isotropic crack distribution. This includes not only a single crack set or a superposition of a single set over an isotropic distribution but also any other rotationally symmetric distribution of cracks. The extracted volumetric component is then used to calculate the unrelaxed high frequency saturated compliances. We assume sparseness of the crack compliance tensor $\overline{W}^m_{ijkl}$ (see appendix) and also assume the ratio of the normal to shear crack compliance to be unknown, but the same for the m different crack sets. The measured change in the dry compliances with pressure, equation (2.10), can be resolved into a sum of as yet unknown volumetric and shear components G_{ijkl} and H_{ijkl} respectively as :

$$\Delta\overline{S}^{(dry)}_{ijkl} = \frac{\Delta S^{(dry)}_{ijkl}}{\Delta S^{(dry)}_{\alpha\alpha\beta\beta}} \approx G_{ijkl} + \alpha H_{ijkl}, \tag{2.19}$$

where

$$G_{ijkl} = \int f(\Omega)\beta_{i3}\beta_{j3}\beta_{k3}\beta_{l3}d\Omega, \tag{2.20}$$

$$\begin{aligned} H_{ijkl} \;=\; & \int f(\Omega)[(\beta_{i2}\beta_{k2} + \beta_{i1}\beta_{k1})\beta_{j3}\beta_{l3} + (\beta_{j2}\beta_{k2} + \beta_{j1}\beta_{k1})\beta_{i3}\beta_{l3} \\ & +(\beta_{i2}\beta_{l2} + \beta_{i1}\beta_{l1})\beta_{j3}\beta_{k3} + (\beta_{j2}\beta_{l2} + \beta_{j1}\beta_{l1})\beta_{i3}\beta_{k3}]d\Omega, \end{aligned} \tag{2.21}$$

and

$$\alpha = (\Delta\overline{S}^{(dry)}_{\alpha\beta\alpha\beta} - 1)/4, \tag{2.22}$$

where $f(\Omega)$ is the normalized crack orientation distribution function such that its integral over all angles equals unity. α, which is computed from the dry data, is the ratio of the representative shear to normal compliance of one crack set, including all elastic interactions with the other cracks. In the above expressions the bar is used to denote the normalized

change in dry compliances, and the β_{ij} are the components of the Euler rotation matrix that relates the crack coordinates to the laboratory coordinate frame. The tensor G_{ijkl} represents the fraction of total compliance that is due to volumetric deformation of cracks with different orientations, for a given externally applied load σ_{ij}.

Now making use of the orthonormality properties of the rotation matrix *viz.* $\beta_{i1}\beta_{j1} + \beta_{i2}\beta_{j2}+\beta_{i3}\beta_{j3} = \delta_{ij}$ and $\beta_{\alpha i}\beta_{\alpha j} = \delta_{ij}$ one can uniquely solve for the independent components of G_{ijkl} :

$$G_{1111} = \Delta\overline{S}^{(dry)}_{1111} - \frac{4\alpha}{1-4\alpha}(\Delta\overline{S}^{(dry)}_{1122} + \Delta\overline{S}^{(dry)}_{1133}), \tag{2.23}$$

$$G_{1122} = \Delta\overline{S}^{(dry)}_{1122}/(1-4\alpha), \tag{2.24}$$

$$G_{1133} = \Delta\overline{S}^{(dry)}_{1133}/(1-4\alpha), \tag{2.25}$$

$$G_{3333} = \Delta\overline{S}^{(dry)}_{3333} - \frac{8\alpha\Delta\overline{S}^{(dry)}_{1133}}{1-4\alpha}, \tag{2.26}$$

$$G_{2323} = \frac{\Delta\overline{S}^{(dry)}_{2323}}{(1-4\alpha)} - \frac{\Delta\overline{S}^{(dry)}_{1111} + \Delta\overline{S}^{(dry)}_{3333}}{4(1-4\alpha)} + \frac{G_{1111} + G_{3333}}{4}. \tag{2.27}$$

Having thus extracted the volumetric part we can calculate the high frequency wet compliances from equation (2.7) as:

$$S^{(dry)}_{ijkl} - S^{(wet)}_{ijkl} \approx \frac{\Delta S^{(dry)}_{\alpha\alpha\beta\beta}}{1 + \phi_{soft}(\beta_f - \beta_0)/\Delta S^{(dry)}_{\alpha\alpha\beta\beta}} G_{ijkl}, \tag{2.28}$$

where ϕ_{soft} is the total soft porosity – the porosity that closes under high confining pressure. Note that if the $\Delta S_{ijkl}^{(dry)}$ are isotropic, then G_{ijkl}^{TI} reduces to the isotropic form in Table 1. If there is a single crack set, then equation (2.28) reduces to a simplified form of equation (2.18). (For a single crack set, equation (2.18) allows a completely general crack compliance tensor W_{ijkl}, while equation (2.28) assumes a sparse W_{ijkl} as described in the appendix.)

2.3.3 Orthorhombic

For three mutually perpendicular crack sets superimposed on a general orthorhombic background equation (2.10) becomes:

$$\Delta S_{ijkl}^{(dry)} = \sum_{m=1}^{3} \overline{\phi}^{(m)} \overline{W}_{rstu}^{(m)} \beta_{ir} \beta_{js} \beta_{kt} \beta_{lu}. \tag{2.29}$$

Assuming crack-like behavior of each set (sparse W_{ijkl}) we get:

$$\begin{aligned} \Delta S_{ijkl}^{(dry)} &= \overline{\phi}^{(1)} \overline{W}_{\alpha\alpha\beta\beta}^{(1)} \delta_{i1}\delta_{j1}\delta_{k1}\delta_{l1} + \overline{\phi}^{(2)} \overline{W}_{\alpha\alpha\beta\beta}^{(2)} \delta_{i2}\delta_{j2}\delta_{k2}\delta_{l2} + \overline{\phi}^{(3)} \overline{W}_{\alpha\alpha\beta\beta}^{(3)} \delta_{i3}\delta_{j3}\delta_{k3}\delta_{l3} \\ &= \Delta S_{1111}^{(dry)} \delta_{i1}\delta_{j1}\delta_{k1}\delta_{l1} + \Delta S_{2222}^{(dry)} \delta_{i2}\delta_{j2}\delta_{k2}\delta_{l2} + \Delta S_{3333}^{(dry)} \delta_{i3}\delta_{j3}\delta_{k2}\delta_{l3}. \end{aligned} \tag{2.30}$$

Similarly the unrelaxed wet moduli, equation (2.7), become:

$$\begin{aligned} S_{ijkl}^{(dry)} - S_{ijkl}^{(wet)} \approx & \frac{\Delta S_{1111}^{(dry)}}{1 + \phi_{soft}^{(1)} (\beta_f - \beta_0) / \Delta S_{1111}^{(dry)}} \delta_{i1}\delta_{j1}\delta_{k1}\delta_{l1} \\ & + \frac{\Delta S_{2222}^{(dry)}}{1 + \phi_{soft}^{(2)} (\beta_f - \beta_0) / \Delta S_{2222}^{(dry)}} \delta_{i2}\delta_{j2}\delta_{k2}\delta_{l2} \end{aligned}$$

$$+\frac{\Delta S_{3333}^{(dry)}}{1+\phi_{soft}^{(3)}(\beta_f-\beta_0)/\Delta S_{3333}^{(dry)}}\delta_{i3}\delta_{j3}\delta_{k3}\delta_{l3}. \tag{2.31}$$

For more general orthorhombic crack distributions the nine independent elements of the G matrix are given by:

$$G_{1111}=\Delta\overline{S}_{1111}^{(dry)}-\frac{4\alpha}{1-4\alpha}(\Delta\overline{S}_{1122}^{(dry)}+\Delta\overline{S}_{1133}^{(dry)}), \tag{2.32}$$

$$G_{2222}=\Delta\overline{S}_{2222}^{(dry)}-\frac{4\alpha}{1-4\alpha}(\Delta\overline{S}_{1122}^{(dry)}+\Delta\overline{S}_{2233}^{(dry)}), \tag{2.33}$$

$$G_{3333}=\Delta\overline{S}_{3333}^{(dry)}-\frac{4\alpha}{1-4\alpha}(\Delta\overline{S}_{1133}^{(dry)}+\Delta\overline{S}_{2233}^{(dry)}), \tag{2.34}$$

$$G_{1122}=\Delta\overline{S}_{1122}^{(dry)}/(1-4\alpha), \tag{2.35}$$

$$G_{1133}=\Delta\overline{S}_{1133}^{(dry)}/(1-4\alpha), \tag{2.36}$$

$$G_{2233}=\Delta\overline{S}_{2233}^{(dry)}/(1-4\alpha), \tag{2.37}$$

$$G_{2323}=\frac{\Delta\overline{S}_{2323}^{(dry)}}{(1-4\alpha)}-\frac{\Delta\overline{S}_{2222}^{(dry)}+\Delta\overline{S}_{3333}^{(dry)}}{4(1-4\alpha)}+\frac{G_{2222}+G_{3333}}{4}, \tag{2.38}$$

$$G_{1313}=\frac{\Delta\overline{S}_{1313}^{(dry)}}{(1-4\alpha)}-\frac{\Delta\overline{S}_{1111}^{(dry)}+\Delta\overline{S}_{3333}^{(dry)}}{4(1-4\alpha)}+\frac{G_{1111}+G_{3333}}{4}, \tag{2.39}$$

$$G_{1212}=\frac{\Delta\overline{S}_{1212}^{(dry)}}{(1-4\alpha)}-\frac{\Delta\overline{S}_{1111}^{(dry)}+\Delta\overline{S}_{2222}^{(dry)}}{4(1-4\alpha)}+\frac{G_{1111}+G_{2222}}{4}, \tag{2.40}$$

and the unrelaxed wet frame compliances are calculated from equation (2.28). To predict the total dispersion these unrelaxed wet frame compliances computed from the squirt formalism are then taken as the effective dry compliances in the Brown and Korringa or Biot equations.

2.4 DISCUSSION

We have presented a technique for predicting the saturated velocities at both high and low frequencies in anisotropic rocks in terms of measureable dry rock velocities. At low frequencies, representative of in situ measurements of water saturated rocks, the saturated elastic compliances can be derived from the dry compliances and total porosity, using equation (2.2). At very high frequencies, as with ultrasonic laboratory measurements, the saturated compliances depend on the distributions of crack orientations and compliances, and can be related to the change of dry rock compliance with pressure, plus a correction proportional to the difference between the compressibilites of the liquid and the mineral. As pointed out by Mavko and Jizba (1991) this has the simple interpretation that filling a compliant pore or crack with unrelaxed fluid resists compression, similar to filling it with mineral, or equivalently, compressing it closed. The second order term compensates for the finite compressibility of the fluid.

The isotropic result, equations (2.15) and (2.16), is consistent with the results of Mavko and Jizba (1991). The tensor G_{ijkl} (Table 2.1) represents the fraction of total compliance due to volumetric deformation of cracks with different orientations, for a given externally applied load σ_{ij}. This form highlights the result found before that for an isotropic rock, the dispersions in bulk and shear are expected to be proportional, (Mavko and Jizba, 1990).

The first transversely isotropic result, equation (2.18), is appropriate when all of the soft, crack-like, porosity is aligned normal to the x_3 direction. This would be indicated

by little or no change of the $\Delta S_{1111}^{(dry)}$ and $\Delta S_{2222}^{(dry)}$ dry compliances with stress. The second transversely isotropic result, equation (2.28), would be appropriate when the dry measurements indicate transversely isotropic behavior, but with stress-induced changes in more than the 3333 component. The general analysis of crack distributions, using equations (2.23)-(2.27) will indicate that a single set of cracks predominates when $G_{3333} \rightarrow 1$ and $G_{1111}, G_{2222}, G_{1122}, G_{1133}, G_{2233} << G_{3333}$.

The orthorhombic result, equation (2.31), is appropriate when the crack-like porosity lies in 1, 2, or 3 perpendicular sets. This would be recognized when the change in dry compliances $\Delta S_{1122}^{(dry)}, \Delta S_{1133}^{(dry)}, \Delta S_{2233}^{(dry)}$ are much smaller than $\Delta S_{1111}^{(dry)}, \Delta S_{2222}^{(dry)}, \Delta S_{3333}^{(dry)}$.

The components of the G matrix for any of the symmetries are calculated directly from the dry data without assuming any specific crack orientation distribution function $f(\Omega)$. In computing these components, care must be taken to ensure that they always correspond to real cracks and not to anti-cracks ($f(\Omega) < 0$). We found that for real data (which are rarely perfect) better results are obtained by slightly damping the denominator in equations (2.23) to (2.27) and keeping the soft porosity correction term in equation (2.28).

Finally, we emphasize that equations (2.15), (2.16), (2.18), (2.28), and (2.31) are for the unrelaxed wet compliances, $S_{ijkl}^{(wet)}$ which describe the stiffening effect of pore fluid in the most compliant parts of the pore space. These must then be substituted into equation (2.2) in place of $S_{ijkl}^{(dry)}$ for the completely saturated behavior $S_{ijkl}^{(sat)}$.

For cracked media saturated with fluid, it is very important to differentiate the two limits or regimes of behaviour depending on the degree of isolation of the cracks with respect to fluid flow : a) low frequency or isobaric behaviour when the fluid may flow and equilibrate the pressure gradients induced by the passing wave, and b) high frequency or adiabatic behaviour when regions of unequilibrated pore pressures are effectively isolated with respect to fluid flow. The unequilibrated pore pressures always makes the rock stiffer in both compression and shear than the isobaric case.

Most crack models of rocks, that are based on idealized ellipsoidal inclusions (Eshelby, 1957; Walsh, 1965; O'Connell and Budiansky, 1974; Nishizawa, 1982) or scatterers (Kuster and Toksöz, 1974; Hudson, 1980, 1981), are high frequency theories in terms of *fluid effects*. This should not be confused with the fact that these models are often termed low frequency models as the wavelengths are assumed to be much larger than crack dimensions. For example, Hudson's (1980, 1981) model of anisotropic cracked rocks treats fluid filled cavities as isolated with respect to fluid flow. Therefore, Hudson's formulation for saturated rocks is best suited for high frequency laboratory conditions but is inappropriate for interpretation of field data. A better approach for low frequency (field) data is to use Hudson's dry rock formulation and then use equation (2.2) to predict the low frequency saturated velocities.

To illustrate this we make a comparison of the results obtained from Hudson's theory and the high frequency squirt model for saturated cracked rocks. Hudson's formulation is limited to small concentrations of highly idealized penny-shaped cracks, while our expressions are valid for *all* crack geometries and crack densities *including* idealized penny-shaped cracks. Therefore, Hudson's formulation can be considered a particular case of the more general formulation. As an example, we consider a rock with a single set of cracks with their normals aligned along the 3-axis. The dry stiffnesses were generated using Hudson's equations, and taken as the input for the squirt model to calculate the saturated stiffnesses which were then compared with those predicted from Hudson's theory. Figure (2.3) shows, for example, C_{33} as a function of crack density for both dry and saturated conditions. Figure (2.4) shows the quasi-P and two quasi-S velocity variation as a function of angle from the symmetry axis (3-axis), again for the dry and saturated cases. The saturated velocities (and stiffnesses) calculated from squirt and Hudson's theory agree very closely, as we expect them to do, since both are high frequency theories.

Figure (2.5) shows angular P and S velocity variation for a conical distribution of cracks i.e. randomly oriented cracks with all their normals at 30 degrees to the 3-axis. As in the previous example, dry stiffnesses were calculated using Hudson's model which were then

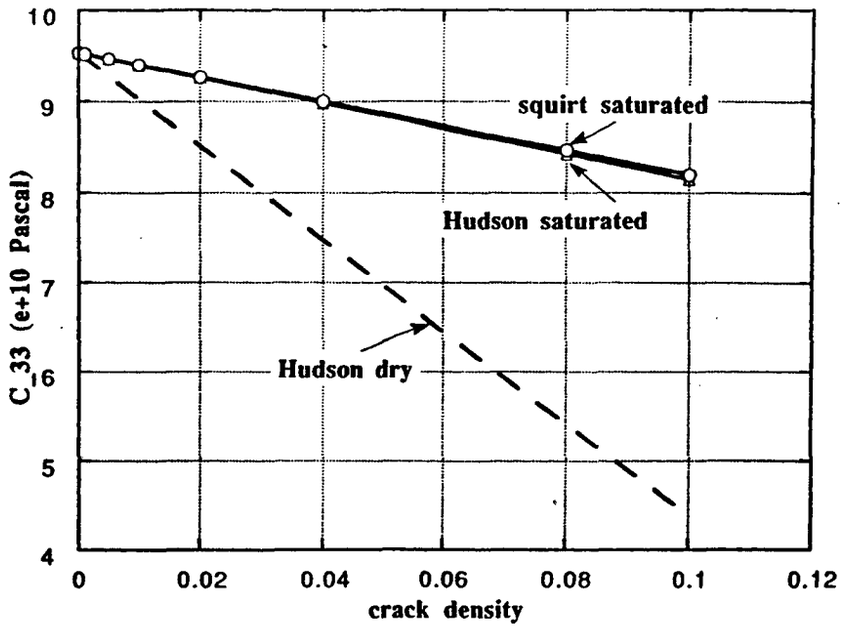

Figure 2.3: Comparision of high frequency predicted saturated C_{33} for transversely isotropic cracked rock for various crack densities. The dry stiffnesses (dashed line) are calculated from Hudson's theory. These are then used in the squirt theory to predict the high frequency saturated stiffnesses. The squirt predictions (circles) match very well with saturated stiffnesses calculated from Hudson's model (triangles).

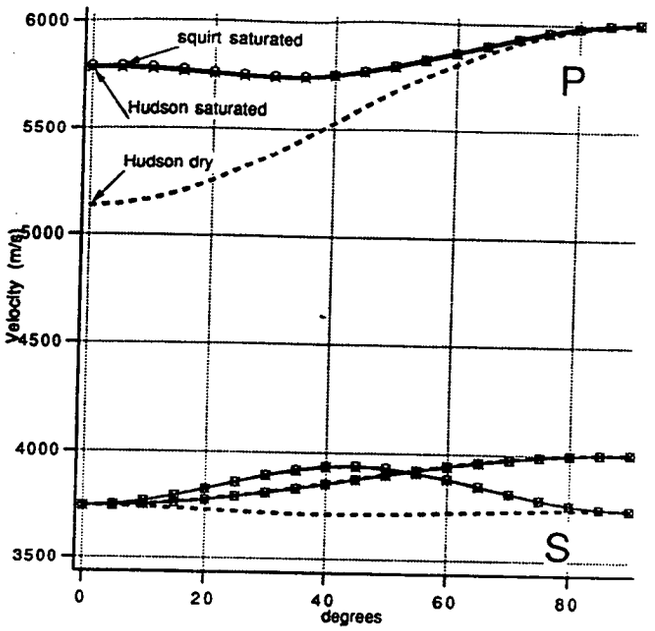

Figure 2.4: Comparision of high frequency saturated P (qP) and S (qS_1, qS_2) velocity variation as a function of angle from the symmetry axis (3-axis) for transversely isotropic cracked rock containing a single crack set with normals aligned along the 3-axis. The dry velocities (dashed line) are calculated from Hudson's theory. These are then used in the anisotropic squirt formalism to predict the high frequency saturated velocities. Saturated squirt predictions (circles); saturated Hudson's model (crosses).

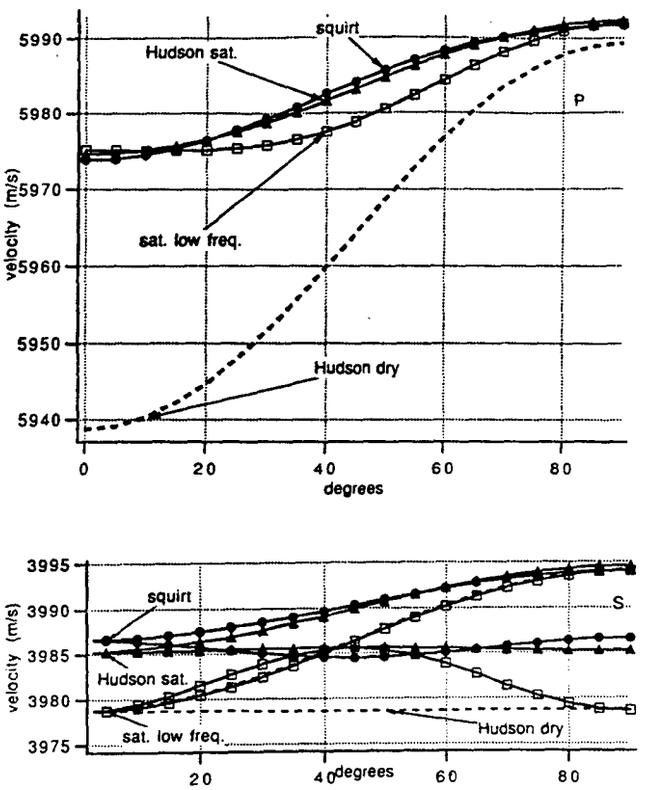

Figure 2.5: Angular P (qP) and S (qS_1, qS_2) velocity variation for conical crack distribution. Cracks randomly oriented with their normals all at 30° to the 3-axis. Dashed line: Hudson dry; squares: saturated low frequency; circles: squirt, high frequency saturated; crosses: Hudson saturated.

used as input for the squirt calculations, equation (2.28). The dashed lines represent dry P and S velocities. The saturated velocities from Hudson's theory and the high frequency squirt calculations are shown by crosses and open circles respectively. The low frequency saturated velocities, calculated from equation (2.2) are represented by squares. Once again we observe that the Hudson and squirt saturated velocities (crosses and open circles) show similar behaviour but, depending on direction of propagation, may be quite different from the low frequency saturated velocities (squares). This difference is more pronounced for the two S waves. The low and high frequency saturated velocities are different because various subsets of the cracks experience unequal induced pore pressures depending on the direction of wave propagation. At high frequencies, these unequilibrated pore pressures make the rock stiffer.

These examples emphasize the difference between high and low frequency saturated moduli (and velocities). They also show that idealized inclusion models (such as Hudson's) are high frequency models with respect to fluid effects, and can be considered to be a particular case of our more general formulation.

Next, we present results of modelling laboratory data using the anisotropic squirt formalism. Figure (2.6) shows V_{p1} and V_{p3}, the fast and slow P velocities in transversely isotropic Arizona sandstone under both dry and saturated conditions, measured at ultrasonic frequencies as a function of confining pressure, (Podio-Lucioni, 1968). The circles are the dry data, and triangles represent saturated measurements. As expected, the low frequency Brown and Korringa predictions are lower than the saturated high frequency measurements. The Biot velocities explain much of the dispersion at high pressure when most of the crack-like porosity is closed, but does a poor job at low pressures. The high frequency squirt predictions capture both the total dispersion and the pressure dependence of the high frequency saturated velocities.

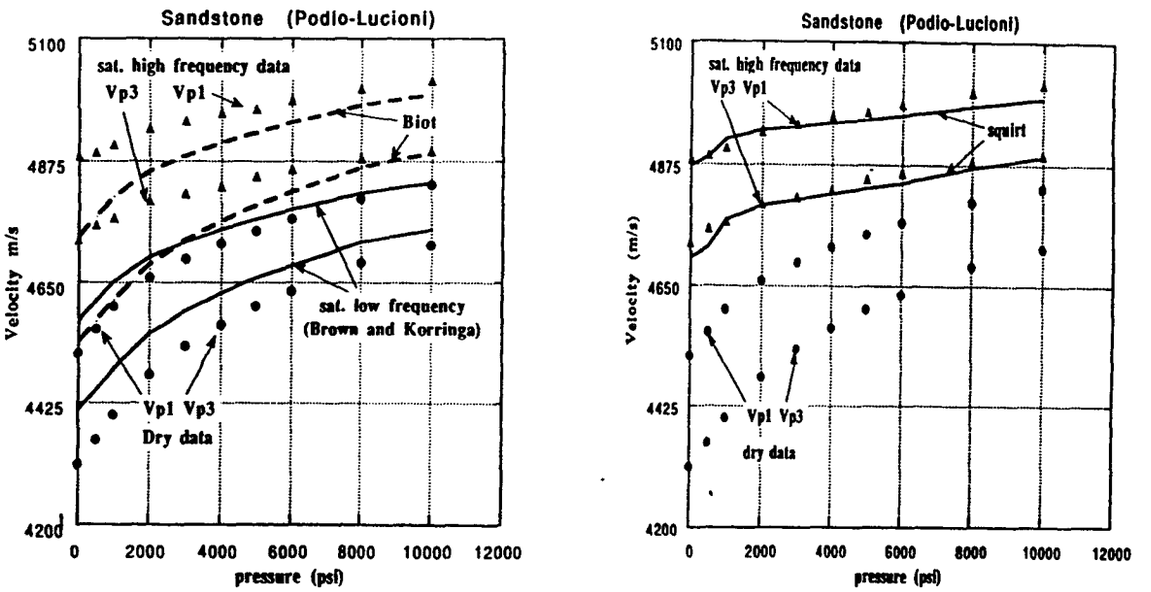

Figure 2.6: Comparision of predicted and measured saturated anisotropic velocities for transversely isotropic sandstone using ultrasonic measurements from Podio-Lucioni, 1968. Circles are the dry V_{p1} (fast) and V_{p3} (slow) measured velocities which are used to predict the measured saturated velocities (triangles). The Biot and Brown and Korringa predictions of saturated V_{p1} and V_{p3} are shown on the left while the anisotropic squirt predictions are represented by the curves on the right. Calculations based on the squirt theory does a much better job of explaining the high frequency saturated velocities.

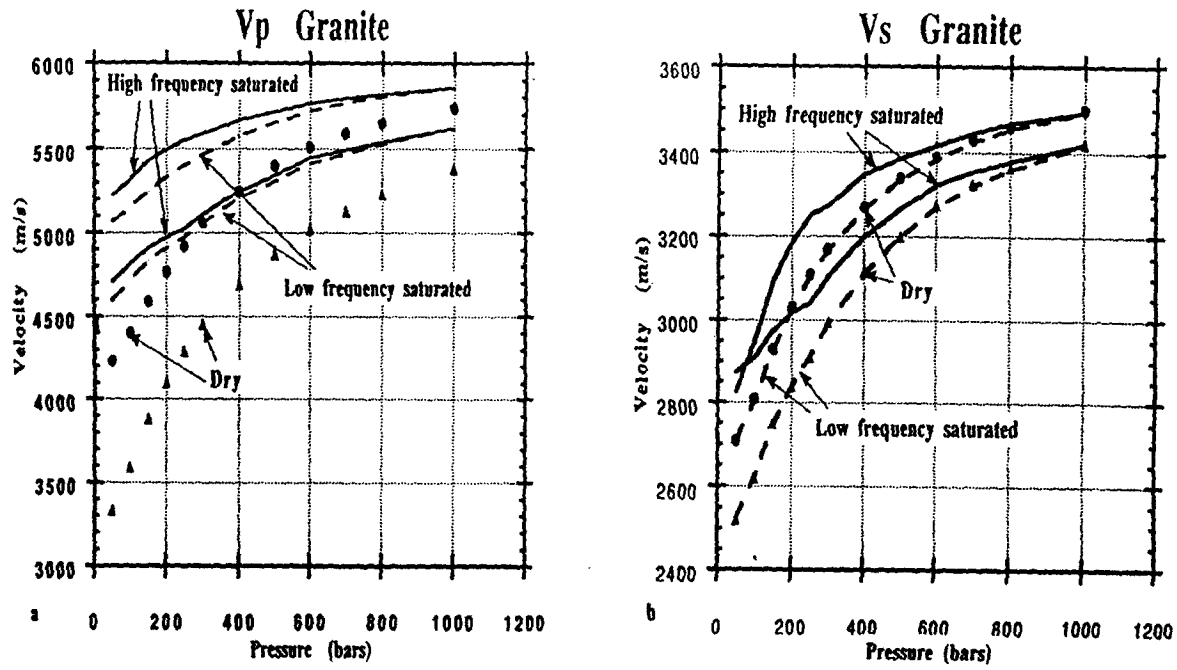

Figure 2.7: Comparision of low and high frequency predicted saturated velocities for transversely isotropic granite. a) P velocities and b) S velocities. The measured dry data from Lo, et al. (1986) are plotted as points and predicted values as curves. For P velocities, the triangles are the dry velocities in the slow x_3 direction and the circles are the dry velocities in the fast x_1 direction. For the shear velocities, the triangles are the dry velocities for one of the equivalent polarizations propagating in the slow x_3 direction, and the circles are the dry velocities propagating in the x_1 direction with the fast x_2 polarization. The dashed curves denote the low frequency predictions of saturated fast and slow velocities using equation (2.2) while the solid curves are the high frequency ones using equation (2.28).

Figure (2.7) compares low and high frequency saturated P and S velocities for transversely isotropic granite calculated using dry pressure-dependent data from Lo, et al. (1986). This data set did not have the measured saturated velocities, so we present the predicted saturated velocities for both low and high frequency regimes of fluid behaviour. The measured dry data are plotted as points, and the predicted values are plotted as curves. For the compressional velocities, the triangles are the velocities in the slow x_3 direction, and the circles are the velocities in the fast x_1 direction. For the shear velocities, the triangles are the velocities for one of the equivalent polarizations propagating in the slow x_3 direction, and the circles are the velocities propagating in the x_1 direction with the fast x_2 polarization. Note that the dry data show anisotropy, even at high pressure, when presumeably most of the cracks are closed. This intrinsic anisotropy accounts for much of the total anisotropy at the lower pressures. Therefore, interpretation of observed anisotropy entirely in terms of cracks can be misleading in rocks such as these.

The dashed curves show the low frequency prediction of saturated velocity, using equation (2.2), and the solid curves the high frequency prediction of saturated velocity, using equation (2.28). We found that for these rocks a single crack set, equation (2.17), was a poor representation of the crack-related anisotropy. The more complete analysis of the G_{ijkl} indicated a distributed range of crack orientations, and ignoring the distribution gave unrealistic results. As expected, the high frequency velocities are almost always faster than the corresponding low frequency values.

The low frequency theory predicts no change in the shear compliances ΔS_{2323} and ΔS_{1313} and hence a small drop in S velocities in the principal directions due to the density effect. For the low porosity granite (0.9%) the dry and low frequency saturated S velocities are barely distinguishable. Although not plotted, the low frequency shear compliances in the non-principal directions are predicted to stiffen with saturation. The high frequency theory predicts an increase in the saturated shear compliances relative to the low frequency

saturated values and therefore an increase in the S velocities. For the low porosity granite the high frequency velocity is always higher than the dry or low frequency saturated values. An interesting observation is the cross-over of the two high frequency saturated S velocity curves at low pressures . This suggests that at high frequencies, the observed velocity anisotropy can be smaller or even in the opposite sense of the anisotropy observed in dry rocks or in saturated rocks at low frequencies. Therefore, finding relatively low velocity anisotropy in the laboratory (at high frequencies) does not preclude finding higher anisotropy in the field.

The compressional velocities always increase from dry to saturated rocks and increase from low frequency to high frequency. At some pressures the saturated velocities have equivalent or slightly smaller anisotropy compared with the dry rocks; but we also find that the high frequency saturated anisotropy can be larger than the dry anisotropy. Therefore, it is not correct to say that saturation always decreases anisotropy.

We summarize some key points illustrated by these examples:

1. Velocities and velocity anisotropy in dry rocks are generally expected to be different than in saturated rocks.

2. Velocities and velocity anisotropy are generally expected to be different at low frequencies, typical of field measurements, and high frequencies typical of laboratory measurements. Therefore, care must be taken when extrapolating from the laboratory to field situations. Our formulation gives a simple method for doing so in a geometry-independent way.

3. A rotationally symmetric distribution of cracks may often be a better model of crack induced transversely isotropic rocks than just a single set of aligned cracks.

4. Assigning all of the observed anisotropy to the presence of cracks may not always be correct as a significant fraction of the anisotropy could be due to the background

matrix.

Finally, an often overlooked point is that inclusion models for velocity anisotropy, such as Hudson's (1980, 1981), are usually *high frequency* theories, in terms of fluid effects. Hudson treats fluid-filled cavities as isolated with respect to fluid flow. As we have discussed, at high frequencies compliant cracks are isolated from the stiff portions of the pore space and from compliant cracks at other orientations; the resulting unequilibrated pore pressures make the rock stiffer. At low frequencies, pore fluid has sufficient time to flow and equilibrate the induced pore pressures throughout the pore space and hence cracks and pores are effectively connected with respect to fluid flow. Consequently Hudson's work is best suited for describing ultrasonic laboratory measurements. Interpretations of low frequency field observations using Hudson's formulation of saturated cracks is inappropriate. A better approach would be to use a dry rock model and to predict low frequency velocities using our equation (2.2).

ACKNOWLEDGEMENTS

This work was supported by the Stanford Rock Physics and Borehole project and by the Department of Energy Contract No. DE-AC21-91MC28087.

REFERENCES

Alford, R. M., 1986, Shear data in the presence of azimuthal anisotropy: Dilley, Texas: Presented at the 56th Ann. Internat. Mtg., Soc. Expl. Geophys.

Backus, G.E., 1962, Long-wave elastic anisotropy produced by horizontal layering: J.Geophys. Res., **67**, 4427-4440.

Biot, M. A., 1956a, Theory of propagation of elastic waves in a fluid saturated porous solid. I. Low-frequency range: J. Acoust. Soc. Amer., **28**, 168-178.

Biot, M. A., 1956b, Theory of propagation of elastic waves in a fluid-saturated porous solid. II. Higher-frequency range: J. Acoust. Soc. Amer., **28**, 179-191.

Biot, M. A., 1962a, Generalized theory of acoustic propagation in porous dissipative media: J. Acoust. Soc. Amer., **34**, 1254-1264.

Biot, M. A., 1962b, Mechanics of deformation and acoustic propagation in porous media: J. Appl. Physics, **33**, 1482-1498.

Brown, R., and Korringa, J., 1975, On the dependence of the elastic properties of a porous rock on the compressibility of the pore fluid: Geophysics, **40**, 608-616.

Carmichael, R. S., 1981, Handbook of physical properties of rocks: CRC Press Inc.

Coyner, K. B., 1984, Effects of stress, pore pressure, and pore fluids on bulk strain, velocity, and permeability in rocks: Ph.D. thesis, Massachusetts Institute of Technology.

Coyner, K. B., and Cheng, C. H., 1985, New laboratory measurements of seismic velocities in porous rocks: Geophysics, **50**, 309.

Crampin, S., 1978, Seismic wave propagation through a cracked solid: polarization as a possible dilatancy diagnostic: Geophys. J. Roy. Astr. Soc., **53**, 467-496.

Crampin, S., 1984, Effective anisotropic elastic constants for wave propagation through cracked solids: Geophys. J. Roy. Astr. Soc., **76**, 135-145.

Crampin, S., Evans, R., and Ucer, S. B., 1985, Analysis of records of local earthquakes: the Turkish dilatancy projects (TDP1 and TDP2): Geophys. J.R. Astr. Soc., **83**, 1-16.

Eshelby, J. D., 1957, The determination of the elastic field of an ellipsoidal inclusion, and related problems: Proc. R. Soc. London, **A241**, 376-396.

Gassmann F., 1951, Uber die elastizitat poroser medien: Vier. der Natur Gesellschaft, **96**, 1-23.

Murphy, W.F., Winkler, K.W., and Kleinberg, 1984, Contact microphysics and viscous relaxation in sandstones, *in* Johnson, D. L., and Sen, P. N., Eds., Physics and Chemistry of Porous media: American Institute of Physics, New York.

Nishizawa, O., 1982, Seismic velocity anisotropy in a medium containing oriented cracks — transversely isotropic case: J. Phys. Earth, **30**, 331-347.

Nur, A. and Simmons, Gene, 1969, The effect of saturation on velocity in low porosity rocks: Earth and Planetary Science Letters, **7**, 183-193.

Nur, A., 1971, Effects of stress on velocity anisotropy in rocks: J. Geophys., Res., **76**, 2022-2034.

Nur, A., 1989, Four-dimensional seismology and (true) direct detection of hydrocarbons: the petrophysical basis: the Leading Edge, September, 30-36.

O'Connell, R., and Budiansky B., 1974, Seismic velocities in dry and saturated cracked solids: J. Geophys. Res., **79**, 5412-5426.

O'Connell, R., and Budiansky B., 1977, Viscoelastic properties of fluid-saturated cracked solids: J. Geophys. Res., **82**, 5719-5736.

Ostrander, W.J., 1982, Plane wave reflection coefficients for gas sands at non normal angles of incidence: Presented at the 52th Ann. Internat. Mtg., Soc. Expl. Geophys.

Podio-Lucioni, A., 1968, Experimental determination of the dynamic elastic properties of anisotropic rocks, ultrasonic pulse method: Ph.D. thesis, Univ. of Texas, Austin.

Pullin, N.E., Matthews, L.W., and Hirsche, W.K., 1986, Techniques applied to obtain very high resolution 3-D seismic imaging at an Athabasca tar sands thermal pilot: Presented at the 56th Ann. Internat. Mtg., Soc. Expl. Geophys.

Queen, J. and Rizer, W., 1990, An integrated study of seismic anisotropy and the natural fracture system at the Conoco borehole test facility, Kay County, Oklahoma: J. Geophys. Res., **95**, 11255-11274.

Raleigh, C. B. and Evernden, J., 1982, Case for low deviatoric stress in the lithosphere, *in* Carter, N. L., Friedman, M., Logan, J. M., and Stearns, D. W., Eds., Mechanical behaviour of crustal rocks: Am. Geophys. Union, Geophys. Mono., 173-186.

Spencer, J., and Nur, A., 1976, The effects of pressure, temperature and pore water on velocities in Westerly granite: J. Geophys. Res., **81**, 899-904.

Stoll, R. D., and Bryan, G. M., 1970, Wave attenuation in saturated sediments: J. Acoust. Soc. Am., **47**, 1440-1447.

Tarif, P., 1986, Mesure de l'Atténuation des ondes compressionelles dans les roches: Application à la mesure de l'anisotropie d'atténuation, Thèse de Doctorat de l'Université

Han. D., 1986, Effects of porosity and clay content on acoustic properties of sandstones and unconsolidated sediments: Ph.D. thesis, Stanford University.

Hudson, J. A., 1980, Overall properties of a cracked solid: Math. Proc. Cambr. Phil. Soc., **88**, 371-384.

Hudson, J. A., 1981, Wave speeds and attenuation of elastic waves in material containing cracks: Geophys. J. R. Astron. Soc., **64**, 133-150.

Hudson, J. A., 1991, Crack distributions which account for a given seismic anisotropy: Geophys. J. Int., **104**, 517-521.

Jaeger, J. C., and Cook, N. G. W., 1969, Fundamentals of rock mechanics: Chapman and Hall.

Jones, T.D., 1983, Wave propagation in porous rocks and models for crustal structure: Ph.D. thesis, Stanford University.

Keller, J. D., 1989, Acoustic wave propagation in composite fluid saturated media: Geophysics, **54**, 1554-1563.

Kuster, G. T. and Toksöz, M. N., 1974, Velocity and attenuation of seismic waves in two-phase media: part I. Theoretical formulations: Geophysics, **39**, 587-606.

Lo, Tien-when, Coyner, K.B., and Toksöz, M.N., 1986, Experimental determination of elastic anisotropy of Berea sandstone, Chicopee shale and Chelmsford granite: Geophysics, **51**, 164-171.

Lockner, D.A., Walsh, J.B., and Byerlee, J.D., 1977, Changes in velocity and attenuation during deformation of granite: J. Geophys. Res., **82**, 5374-5378.

Lucet, N.M., and Tarif, P.A., 1988, Shear wave birefringence and ultrasonic shear wave attenuation measurements: Presented at the 58th Ann. Internat. Mtg., Soc. Expl. Geophys.

Lueschen, E., Nolte, B., and Fuchs, K., 1990, Shear wave evidence for an anisotropic lower crust beneath the Black Forest, Southwest Germany: Tectonophysics, **173**, 483-493.

Mavko, G. and Nur, A., 1975, Melt squirt in the asthenosphere: J. Geophys. Res., **80**, 1444-1448.

Mavko, G. and Nur, A., 1979, Wave attenuation in partially saturated rocks: Geophysics, **44**, 161-178.

Mavko, G. and Jizba, D., 1991, Estimating grain-scale fluid effects on velocity dispersion in rocks: Geophysics, **56**, 1940-1949.

Paris 7.

Thomsen, L., 1985, Biot-consistent elastic moduli of porous rocks: low-frequency limit: Geophysics, **50**, 2797-2807.

Thomsen, L., 1986, Elastic anisotropy due to aligned cracks: Theoretical models: Trans. Am. Geoph. Union, **67** , 1207.

Thomsen, L., 1991, Elastic anisotropy due to aligned cracks in porous rocks, EAEG Mtg. Abstrs., **53**, 244.

Walls, J.D., 1983, Effects on pore pressure, confining pressure and partial saturation on permeability of sandstones: Ph.D. thesis, Stanford University.

Walsh, J., 1965, The effect of cracks on the compressibility of rock: J. Geophys. Res., **70**, 381-389.

Walsh, J., 1980, Static deformation of rock: Proc. ASME, **106**, 1005-1019.

Wang, Z., and Nur, A., 1988, Velocity dispersion and the "local flow" mechanism in rocks: 58th Ann. Internat. Mtg., Soc. Expl. Geophys., Expanded Abstracts, 928-930.

Wang, Z., and Nur, A., 1990, Dispersion analysis of acoustic velocities in rocks: J. Acoust. Soc. Am., **87**, 2384-2395.

Willis, H. A., Rethford, G. L. and Bielavski, E., 1986, Azimuthal anisotropy: occurrence and effect of shear wave data quality: Presented at the 56th Ann. Internat. Mtg., Soc. Expl. Geophys.

Winkler, K., 1985, Dispersion analysis of velocity and attenuation in Berea sandstone: J. Geophys. Res., **90**, 6793-6800.

Winkler, K., 1986, Estimates of velocity dispersion between seismic and ultrasonic frequencies: Geophysics, **51**, 183-189.

Winterstein, D. F., and Meadows, M. A., 1991, Shear wave polarizations and subsurface stress directions at Lost Hills field: Geophysics, **56**, 1331-1348.

Zamora, M., and Poirier, J.P., 1990, Experimental study of acoustic anisotropy and birefringence in dry and saturated Fontainebleau sandstone: Geophysics, **55**, 1455-1465.

APPENDIX

Stress Induced Pore Pressure

We derive the stress induced pore pressure in the *nth* pore using linear superposition, as shown in Figure 2.8. The change in volume, Δv_n, can be written as the sum:

$$\Delta v_n = v W^{(n)}_{ijkk}(\Delta\sigma_{ij} - \Delta P_n \delta_{ij}) + \Delta P_n \beta_0 v_n \tag{2.41}$$

Equating this with the volume change of the fluid within the pore, $\Delta v_n = \Delta P_n \beta_f v_n$, gives equation (2.5).

Sparse Crack Compliance Tensor

For crack like features we expect the intrinsic compliance tensor in the crack coordinate system, $\overline{W}_{ijkl}$, to be sparse. The largest components of the tensor are the normal compliance $\overline{W}_{3333}$ and the shear compliances $\overline{W}_{2323}$ and $\overline{W}_{1313}$. The other components are approximately zero. This is a general property of planar crack formulations and reflects an approximate decoupling of normal and shear deformation of the crack and decoupling of the in plane and out of plane compressive deformation. This allows us to write $\overline{W}_{\alpha\alpha\beta\beta} \approx \overline{W}_{3333}$ and $\overline{W}_{ij\alpha\alpha} \approx \overline{W}_{3333}\delta_{i3}\delta_{j3}$.

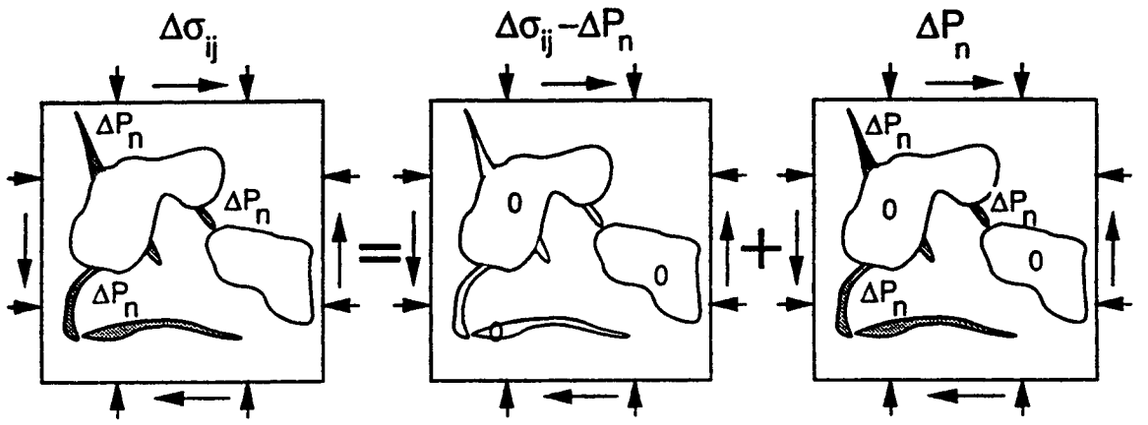

Figure 2.8: Decomposition of stresses applied to the saturated rock, in order to estimate the pore pressure induced in the nth pore.

Chapter 3

SCALE EFFECTS: 1-D PERIODICALLY LAYERED MEDIA

SCALE EFFECTS ON VELOCITY DISPERSION: FROM RAY TO EFFECTIVE MEDIUM THEORIES IN STRATIFIED MEDIA

ABSTRACT

Wave propagation in stratified media may be explained by ray theory, effective medium theory, or scattering theory depending on the scales of wavelength and layer spacing. In order to effectively integrate and utilize seismic data at different frequencies and widely varying scales, it is essential to understand the domain of applicability of long and short wavelength behavior and the transition between them. A joint experimental and theoretical study was conducted to investigate velocity behavior at the transition from ray theory to effective medium theory in stratified media. Velocity measurements were performed at 50 and 500 kHz on periodic media composed of steel and plastic discs. The ratio of wavelength to layer spacing, λ/d, spanned more than two orders of magnitude between 0.1 and 50, and the volume fraction of steel ranged from 9 to 89 percent by volume. Our results confirm that velocities in stratified media depend on composition and are controlled by the ratio of wavelength to layer spacing. Velocities in the short wavelength limit are generally faster than velocities in the long wavelength limit. We find that transition from ray to effective medium approximations occurs over a narrow range of λ/d at a value of approximately 10. The amount of velocity change increases with impedance contrast, but the value of λ/d at the transition is generally independent of the composition of the stratified medium. Our numerically simulated waveforms are in close agreement with the experimentally observed delayed first arrival in the long wavelength limit and reduced amplitudes at the transition from short to long wavelength regime.

3.1 INTRODUCTION

An almost universal feature of rock formations in sedimentary basins is that they tend to be layered and heterogenous at many scales. These heterogeneities include variations in lithology, porosity, permeability, pore fluid properties, and conditions of pore pressure, temperature, and stress. Heterogeneities determine the scales and variability of flow units and their bounding surfaces, and therefore impact the amounts and producibility of reservoir fluids. Consequently, imaging and characterizing these heterogeneities and their scales is the essential problem of reservoir characterization.

Layering and heterogeneity also impact wave propagation and the interpretability of seismic images. For example, waves propagating normal to layering are dispersive. When the ratio of seismic wavelength to layer spacing, λ/d, is small, ($\lambda/d \ll 1$), wave propagation may be described using ray theory with velocities that are faster than in the effective medium limit ($\lambda/d \gg 1$) (O'Doherty and Anstey, 1971; Schoenberger and Levin, 1974; Helbig, 1984; Marion and Coudin, 1992; Tang and Burns, 1992). Therefore, measured seismic velocities depend, not only on the rock and fluid properties that we wish to image, but also on the scale of our measurements relative to the scale of the geology.

This raises critical questions of the proper approach to modelling and interpreting velocities: When is ray theory appropriate? When is effective medium theory appropriate? Is there a transition when neither is valid, and what determines it? It is essential to understand these in order to properly upscale seismic velocities and to relate measurements at different frequencies and scales encountered in laboratory ($f \approx 10^6 Hz$, $\lambda \approx 5 \times 10^{-3} m$), logging ($f \approx 10^4 Hz$, $\lambda \approx 0.5m$), and seismic ($f \approx 10^2 Hz$, $\lambda \approx 50m$) measurements.

There have been numerous theoretical, computational, and experimental studies concerned with wave propagation in stratified media, (e.g. Postma, 1956; Backus, 1962; Sun et

al. 1968; O'Doherty and Anstey, 1971; Sve, 1971; Schoenberger and Levin, 1974; Christensen, 1975; Berryman, 1979; Helbig, 1984; Melia and Carlson, 1984; Carcione et al. 1991; Kerner, 1992; Marion and Coudin, 1992; Stanke and Burridge, 1993). Some have dealt with the effective properties of the stratified media in the long wavelength limit, while others have focussed on the velocity dispersion due to scattering effects ($\lambda/d \approx 1$). Both theoretical and experimental results indicate that when the wavelength is much larger than the layer spacing, layered media behave as homogenous (transversely anisotropic) media. However, the minimum value of λ/d for which the long wavelength approximation holds is still a matter of controversy and research, with $\lambda/d > 3$ (Helbig, 1984) from theoretical considerations, $\lambda/d > 5-8$ from numerical modeling (Carcione et al. 1991), and $\lambda/d > 10$ from experiments (Melia and Carlson, 1984; Marion and Coudin, 1992).

In this study, our objective is to investigate, both experimentally and theoretically, the velocity behavior in stratified media at the transition between long and short wavelength limits. Our purpose is not to emphasize the anisotropic properties of stratified media, but rather to look at normal incidence propagation as the simplest, one-dimensional illustration of scale effects on velocity. While layers in realistic exploration situations are rarely perfectly periodic, they can be thought of as a superposition of various spatial periods. Therefore, understanding scale effects in periodically layered media forms a framework for investigating scale effects in more complex layered geology. We restrict this study to periodic media and investigate specifically the influence of composition, volume fraction, layer spacing, and wavelength on velocities.

3.2 RAY THEORY AND EFFECTIVE MEDIUM BEHAVIOUR

In the long wavelength limit, $\lambda/d \gg 1$, where λ is seismic wavelength and d is the

scale of the layering, a stratified medium behaves as a homogenous effective medium with velocity of wave propagation normal to the layering given by:

$$V_{EMT} = \left(\frac{M_{EMT}}{\rho_{ave}} \right)^{1/2} . \tag{3.1}$$

The effective modulus, M_{EMT}, is obtained from the Backus average (Backus, 1962) of the elastic stiffness tensors C_{ijkl} of the constituents. For normal incidence propagation this is equivalent to the Reuss or iso-stress average:

$$M_{EMT} = \left[\sum_k \frac{f_k}{M_k} \right]^{-1} \tag{3.2}$$

or

$$\frac{1}{\rho_{ave} V_{EMT}^2} = \sum_k \frac{f_k}{\rho_k V_k^2} \tag{3.3}$$

where f_k, ρ_k, M_k, and V_k are the volume fractions, densities, moduli, and velocities of each constituent, respectively. M can be interpreted as C_{3333} for P waves and as C_{2323} for S waves. The average density, ρ_{ave}, is:

$$\rho_{ave} = \sum_k f_k \rho_k \tag{3.4}$$

In the ray theory or short wavelength limit ($\lambda/d \ll 1$), the total travel time for waves travelling perpendicular to the layers is the sum of the travel times through each layer. The ray theory average velocity through the medium is therefore:

$$\frac{1}{V_{RT}} = \sum_k \frac{f_k}{V_k} \tag{3.5}$$

Note that ray theory velocities, equation (3.5), involve averaging slownesses, while effective medium velocities, equations (3.2) and (3.3), involve averaging compliances (slowness squared). This results in the long wavelength (effective medium) velocity always being slower than the short wavelength (ray theory) velocity.

For a two-component layered medium with equal volume fractions of each constituent one can derive simple useful expressions relating the ratio of the two limiting velocities to the density ratio $\rho_r = \rho_1/\rho_2$ and one of three other ratios: the velocity ratio $V_r = V_1/V_2$, impedance ratio $Z_r = Z_1/Z_2$ or the modulus ratio $M_r = M_1/M_2$, where subscripts 1 and 2 designate the two constituents:

$$V_{RT}/V_{EMT} = \frac{1}{(1+V_r)}\sqrt{\frac{(1+\rho_r)(1+\rho_r V_r^2)}{\rho_r}} \tag{3.6}$$

$$V_{RT}/V_{EMT} = \frac{\sqrt{(1+\rho_r)(\rho_r+Z_r^2)}}{(\rho_r+Z_r)} \tag{3.7}$$

$$V_{RT}/V_{EMT} = \frac{\sqrt{(1+\rho_r)(1+M_r)}}{(\sqrt{\rho_r}+\sqrt{M_r})} \tag{3.8}$$

When $\rho_r \approx 1$ these may be further simplified to:

$$\begin{aligned} V_{RT}/V_{EMT} &\approx \frac{\sqrt{2(1+V_r^2)}}{1+V_r} \\ &\approx \frac{\sqrt{2(1+Z_r^2)}}{1+Z_r} \end{aligned}$$

$$\approx \frac{\sqrt{2(1+M_\tau)}}{1+\sqrt{M_\tau}} \tag{3.9}$$

3.3 EXPERIMENTAL PROCEDURE

Laboratory measurements were made to explore the dependence of velocity on λ/d in layered media and to establish the range of validity of both the long and short wavelength theories. The laboratory stratified media consisted of various proportions of plastic and steel discs stacked periodically, with spatial period ranging from 1 millimeter to a few centimeters. Thicknesses of the steel and plastic discs were 490 and 540 microns, respectively. The disc diameter was 4.726 centimeters. Thick layers (large effective period, d) were created by putting many plastic discs together, then many steel discs, and so on; thin layers (smaller effective d) were created with a small number of plastic discs next to a small number of steel discs, while keeping the total number of discs the same. Typically 90-100 discs were stacked for a total sample length of about 5cm. Coupling between discs was achieved using viscous coupling fluid that represented less than 1 percent by volume of the composite medium. The physical properties of the plastic and steel discs are listed in Table 3.1. These values do not correspond to pure compounds, as they were measured on stacked plastic and steel discs with coupling material between each disc. Densities of the samples were determined from their weights and volumes measured from their dimensions.

Compressional P-wave transducers were placed on each end of the stack, in order to measure propagation normal to the layering. Velocities were measured at 500 kHz and 50 kHz using the pulse transmission technique. A constant normal force was applied to the samples through the transducers to ensure good and repeatable contact between the sample and the transducers.

Average velocities were determined as the total measured sample length divided by the

Material	P-Velocity (m/s)	Density (g/cc)
Steel	5535	7.90
Plastic	2487	1.21

Table 3.1: Material properties of steel and plastic.

picked first break arrival time. The wavelength, λ, was taken as the measured velocity multiplied by the observed dominant period — the time from the first arrival pick to the second zero crossing.

3.4 THEORETICAL MODELLING

The dispersion relation for waves propagating normal to a periodic stratified medium made up of two constituents with phase velocities V_1 and V_2 and thicknesses d_1 and d_2 may be obtained from the well known Floquet solution for periodic media, (see e.g. Christensen, 1991):

$$\cos(\frac{\omega d}{V}) = \cos(\frac{\omega d_1}{V_1})\cos(\frac{\omega d_2}{V_2}) - \chi \sin(\frac{\omega d_1}{V_1})\sin(\frac{\omega d_2}{V_2}) \tag{3.10}$$

where

$$\chi = \frac{\rho_1 M_1 + \rho_2 M_2}{2\sqrt{\rho_1 \rho_2 M_1 M_2}} \tag{3.11}$$

and $d = d_1 + d_2$ is the spatial period, while ω is the angular frequency. Solution of the dispersion relation gives the phase velocity of propagation, V, as a function of frequency and the layer parameters. If the periodic spacing d is a multiple of one-half wavelength, multiple reflections are all in phase and add constructively. When this Bragg scattering

condition is satisfied a large total accumulated reflection results. The frequency at which this occurs is called Bragg frequency, and waves cannot propagate within a band of frequencies (stop-band) around any Bragg frequency, (Auld, 1991). The periodic medium thus acts as a wave filter.

One can show, by expanding the terms in equation (3.10) as a power series in ω and retaining only terms up to second order, that $V \rightarrow V_{EMT}$ as $\omega \rightarrow 0$. In the low frequency (long wavelength) range, $V \approx V_{EMT}$ as long as $\lambda/d > 2\pi$.

An approach for computing full waveform propagation in layered media (not restricted to periodic ones) is the use of propagator matrices, (Aki and Richards, 1980; Claerbout, 1985). The wave variables of interest at the top and bottom of a stack of layers are related by a product of propagator matrices, one for each layer. For waves travelling perpendicular to n layers:

$$\begin{bmatrix} S \\ W \end{bmatrix}_n = \prod_{k=1}^{n} A_k \begin{bmatrix} S \\ W \end{bmatrix}_1 \tag{3.12}$$

where S and W are the Fourier transforms of the wave variables σ and w, respectively. For normal incidence P-waves, σ is interpreted as the normal stress across each interface, and w is the normal component of particle velocity. For normal incidence S-waves, σ is the shear traction across each interface and w is the tangential component of particle velocity. Each layer matrix A_k has the form:

$$A_k = \begin{bmatrix} \cos(\frac{\omega d_k}{V_k}) & i\sqrt{\rho_k M_k}\sin(\frac{\omega d_k}{V_k}) \\ i\frac{1}{\sqrt{\rho_k M_k}}\sin(\frac{\omega d_k}{V_k}) & \cos(\frac{\omega d_k}{V_k}) \end{bmatrix} \tag{3.13}$$

We used this method to model wave propagation through the stratified media studied

in the laboratory, assuming plane waves travelling normal to layers of infinite lateral extent. Matrices A_k were constructed to represent the steel and plastic layers, respectively, and multiplied, as in equation (3.12), to simulate the desired sequence. S_1 is the Fourier transform of the input waveform at the top of the stack, which was set equal to the Fourier transform of the waveform recorded in the laboratory when the transducers were placed in contact without sample discs. Arrival times and periods were picked from the computed waveforms at the bottom of the stack in the same manner as for the laboratory waveforms.

3.5 RESULTS

Figure 3.1 shows recorded and calculated waveforms at 500 kHz for sample # 64 (32 plastic discs, and 64 steel discs). The solid lines are the experimentally observed waveforms; the dashed lines are the theoretically calculated ones. Picks of the first arrival times and the theoretical short (RT) and long wavelength (EMT) travel times are indicated. The picks pointing upwards are for the experimental traces, and those pointing down are for the theoretical ones. The stacks of plastic and steel layers were arranged to have different spatial periods to span the range from short to long wavelength behavior. The top trace is for the case when all 32 plastic layers are stacked together, next to all 64 steel discs, resulting in effectively two thick layers with a spatial period longer than the seismic wavelength. The next case corresponds to thinner layers with half of the plastic discs (16) next to half of the steel discs (32), etc. Each subsequent trace corresponds to decreasing the spatial period by a factor of two. Finally, the bottom trace corresponds to layer spacing much smaller than a wavelength. In each case the total number of discs and the total sample length are the same. Only the scale of the layering varies.

The theoretical and measured waveforms show two key features. First, the arrival times are systematically delayed from the small λ/d case to the large λ/d case. Second, there is a decrease in amplitude accompanied by a change in frequency content at the transition

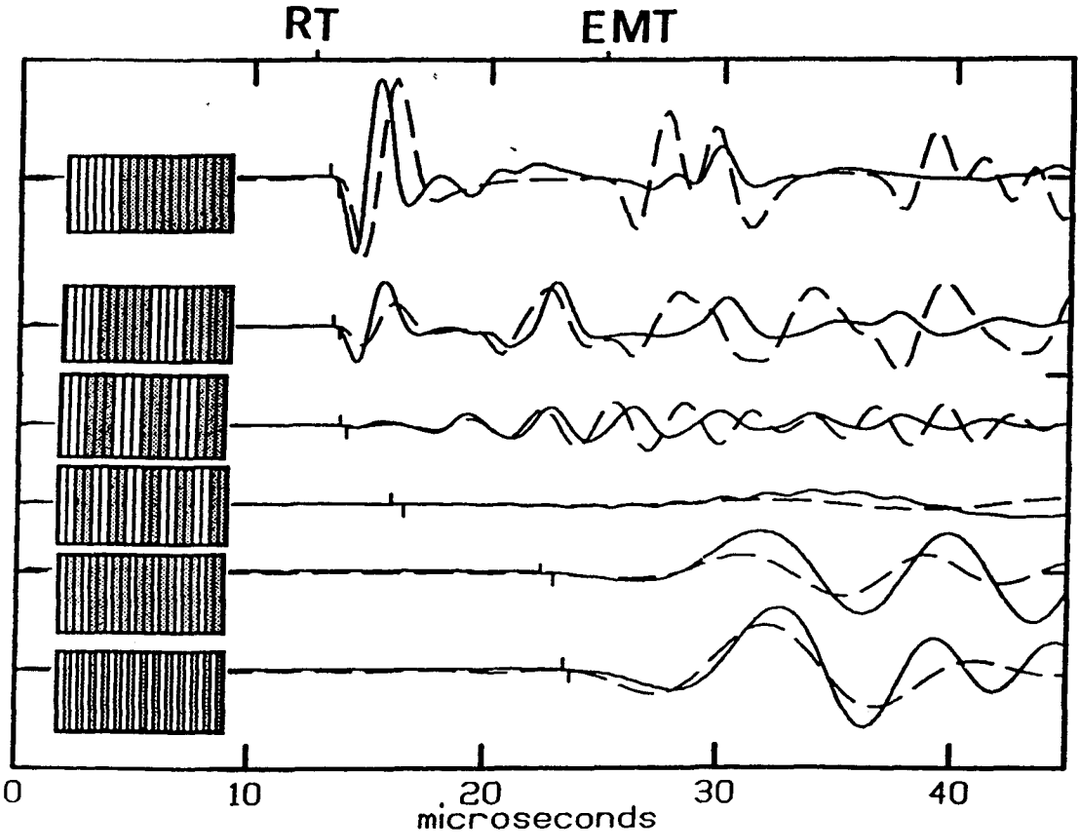

Figure 3.1: Experimentally observed (solid line) and computed (dashed lines) waveforms for periodic stacks of plastic and steel layers with different spatial periods, and a pulse frequency of 500 kHz. The top trace is for the case when the spatial period is much larger than the wavelength while the bottom one is for the situation when it is much smaller. The long wavelength (EMT) and short wavelength (RT) arrival time predictions and picks for each trace are indicated. Upper picks are for the experimental traces and lower picks are for the theoretical ones. Notice the delay in the first arrival at the long wavelength limit (bottom trace) and the attenuation of the amplitude at the transition from ray theory to effective medium behavior.

between the two domains. In all cases, the computations capture very well these essential features of the experimental observations. The decrease in amplitude is associated with the presence of stop bands mentioned above in our discussion of the Floquet solution for periodic media. The periodic medium acts as a filter to the input wavelet, transmitting selected frequencies in the finite-bandwidth wavelet and reflecting back other frequencies. This tuning effect contributes to the change in the frequency content of the received signal. Numerical calculations do not reproduce so well the later reflected arrivals in the wavetrain. We suspect that the differences result from neglecting the finite width of the sample and not modelling the transmission losses through the loading system at the ends of the sample.

To investigate the frequency dependence of velocity in stratified media, measurements were performed on the same sample # 64 at both 50 kHz and 500 kHz. In Figure 3.2a, velocities measured at 50 kHz and 500 kHz are plotted versus λ/d. The data at the two different frequencies fall along the same trends, and we can see that the relation between velocity and λ/d is independent of frequency. The parameter λ/d is defined here as the ratio of the dominant wavelength of the primary received signal to the spatial period of the periodic plastic-steel unit. We find on this data set that the experimentally observed transition from short to long wavelength behavior occurs in a very narrow range of λ/d between 10 and 15. In these (and many of the following) figures, smooth curves have been drawn through the data points to delineate the trend of the behavior.

Figure 3.2b shows velocities at 50 kHz and 500 kHz, picked from computed waveforms for sample # 64 and plotted as a function of λ/d. The transition from ray theory to effective medium behavior takes place at a smaller value of λ/d (≈ 7) for the numerical calculations than it does in the laboratory (≈ 10). The discrepancy is small, but is nevertheless consistent with previous theoretical and numerical modelling results that tends to place the transition always at a slightly smaller value than experimental observations (Berryman, 1979; Helbig, 1984; Melia and Carlson, 1984; Carcione et al., 1991). The theoretical velocities tend to be slightly slower than the measured ones.

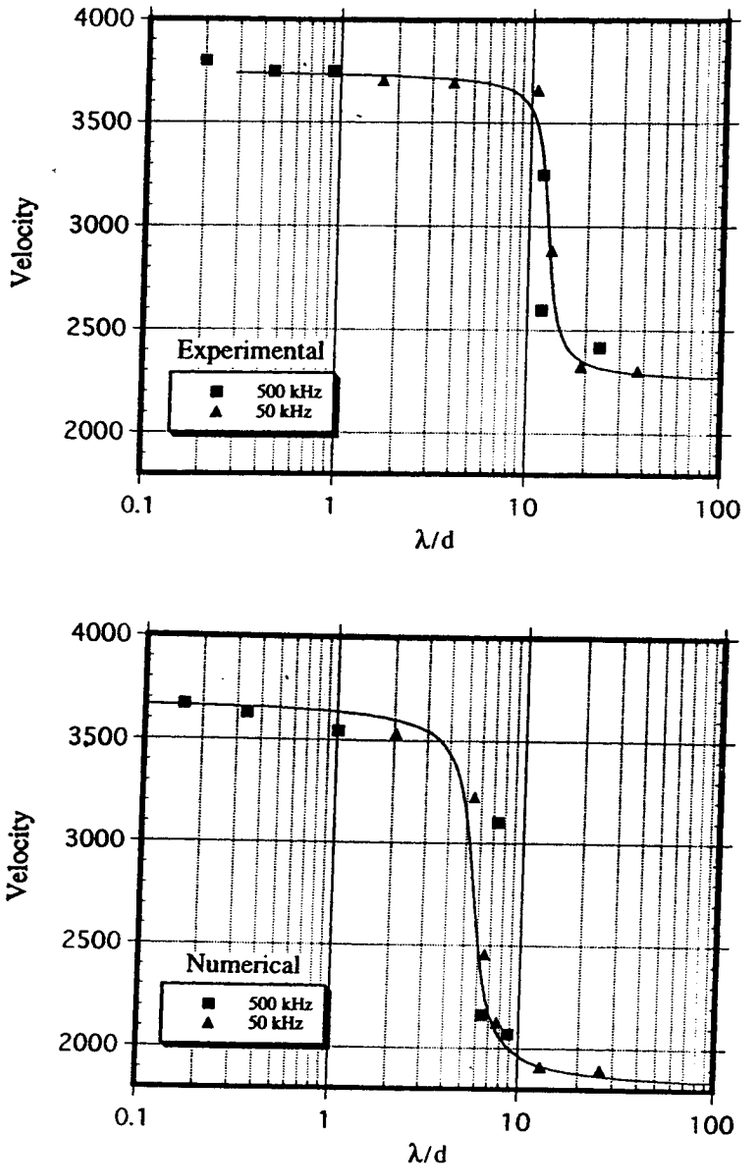

Figure 3.2: (a) Experimental velocity versus λ/d for sample # 64 (32 plastic discs and 64 steel discs) at the transition from short to long wavelength behavior. Squares and triangles represent measurements at 500 and 50 kHz, respectively. A smooth curve has been drawn through the data points to indicate the trend. (b) Theoretical velocities calculated from first arrivals as a function of the ratio of wavelength to layer spacing, λ/d, for sample # 64. Calculations for 500 kHz and 50 kHz are indicated by squares and triangles, respectively.

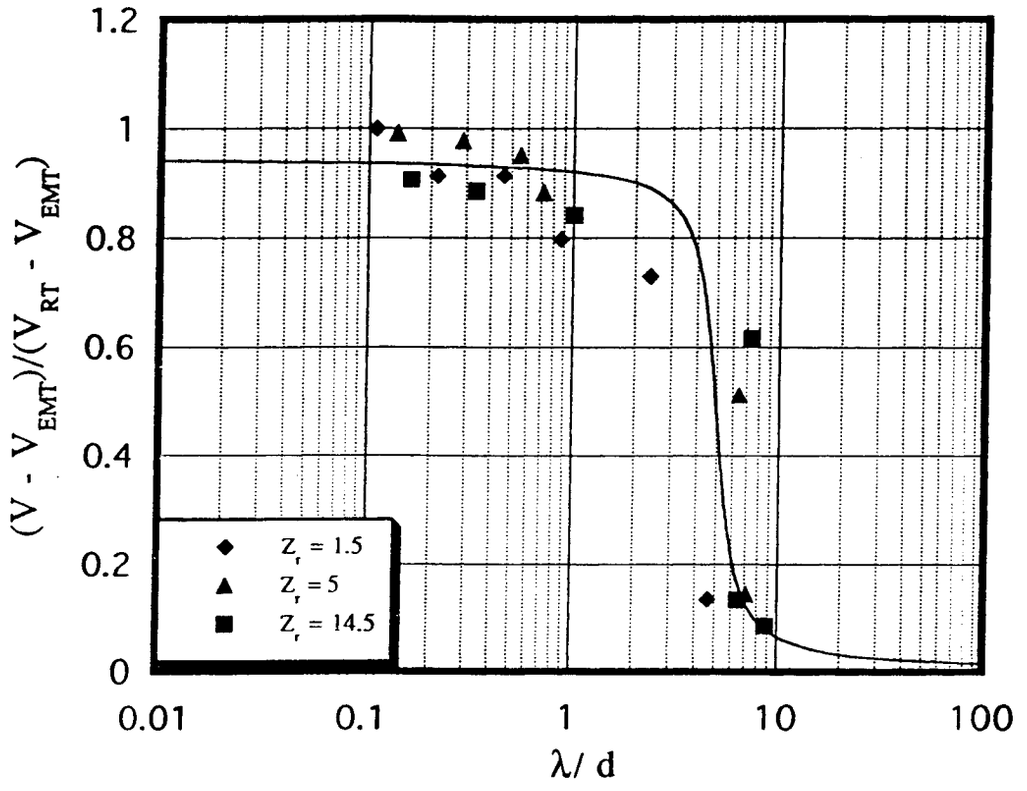

Figure 3.3: Calculated normalized velocities as a function of λ/d for various impedance contrasts between the layers. The value of λ/d above which effective medium theory is valid is not strongly dependent on the impedance contrast. The impedance contrast spans a range from 1.5 to 14.5.

We explored numerically the influence of varying composition and impedance contrasts between the constituent layers. Figure 3.3 shows a plot of normalized velocities, $(V - V_{EMT})/(V_{RT} - V_{EMT})$, versus λ/d for impedance contrasts of 1.5, 5, and 14.5 with the same geometry as sample # 64. The transition value of λ/d shows only a weak dependence on the material properties of the layers. The transition occurs at a slightly lower value of λ/d for smaller impedance contrast (1.5) than for larger impedance contrasts. However the difference between the short and long wavelength velocities increases with increasing contrast between the material properties of the layers. For a two-component layered medium with equal volume fractions of each component, the ratio of the short wavelength (ray theory) to long wavelength (effective medium) velocities, V_{RT}/V_{EMT}, can be expressed in terms of the ratio of the densities and velocities (or equivalently moduli or seismic impedances) of the two components, as given by equations (3.6), (3.7), and (3.8). Figure 3.4 shows a contour plot of equation (3.6), indicating the scale-dependent velocity dispersion that can be expected for various material contrasts. Typical values for sand/shale, shale/dolomite, and shale/coal layered sequences are indicated. There can be as much as 20 percent velocity dispersion due to scale effects alone in layered strata consisting of alternating shale and dolomite beds. Note the interesting case when the velocity ratio, V_r, is the reciprocal of the density ratio, ρ_r, then $V_{RT}/V_{EMT} = 1$.

To investigate the influence of volume fraction of the constituents on the velocity behavior at the transition from short to long wavelength behavior, velocity data measured for various fractions of plastic and steel were normalized to the theoretical short and long wavelength velocities, V_{RT} and V_{EMT}, respectively. Figures 3.5a and 3.5b show the experimental and theoretical dependences of normalized velocities on λ/d for five samples, corresponding to volume fractions of steel of 0.09, 0.31, 0.47, 0.64, and 0.89 respectively. On these figures, measurements at 500 kHz and 50 kHz are represented with filled and open symbols, respectively.

From these figures, one can divide the velocity behavior into three parts:

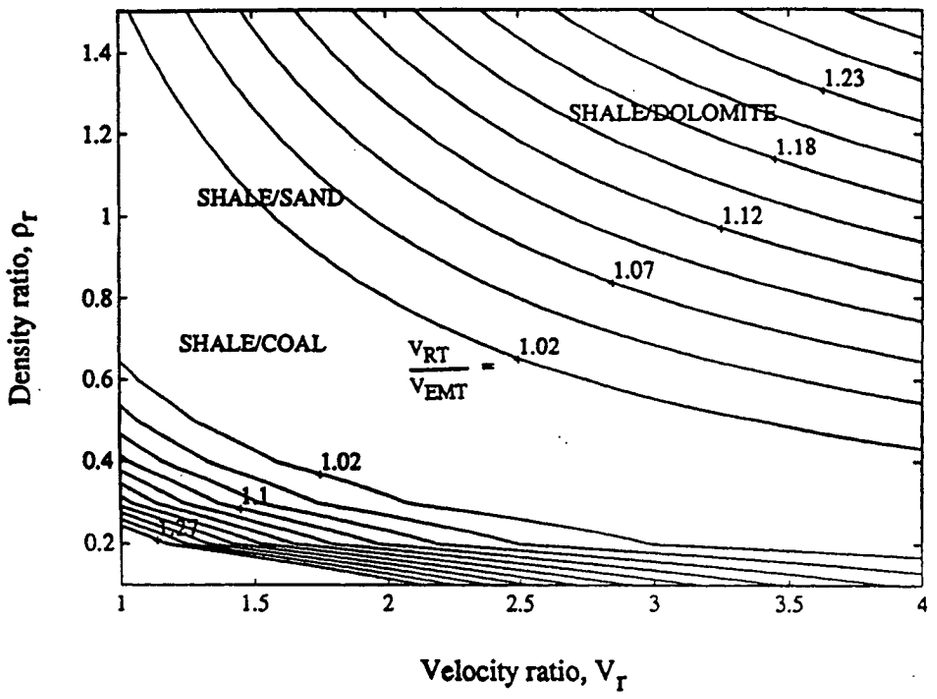

Figure 3.4: Contour plot of V_{RT}/V_{EMT} for a two-component layered medium with equal volume fractions of the two constituents. The difference between V_{RT} and V_{EMT} increases as the contrast in the velocities and densities of the two components increases.

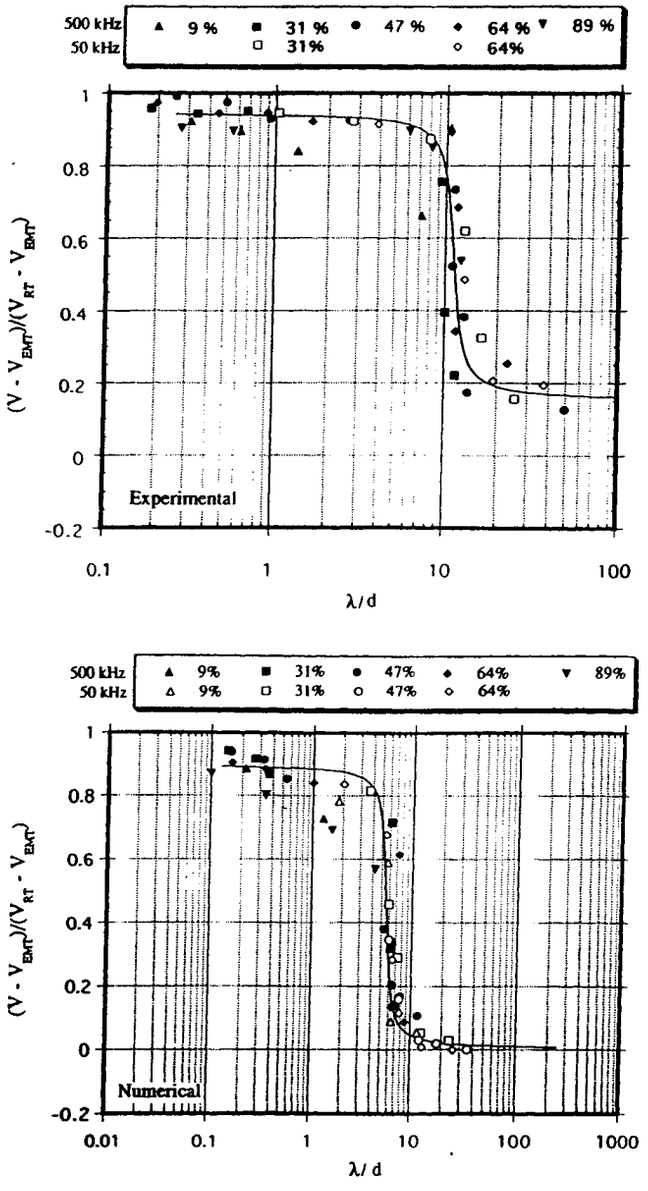

Figure 3.5: a) Experimentally observed dependence of normalized velocity on λ/d for five samples corresponding to fractions of steel of 0.09, 0.31, 0.47, 0.64, and 0.89 respectively. Measurements at 500 kHz and 50 kHz are represented by filled and open symbols respectively. b) Same as a) calculated theoretically.

1) For values of λ/d ranging between 0.1 and 10, velocity slightly decreases with increasing λ/d but remains close to the short wavelength limiting velocity. The experimental velocities are closer to the ray theory velocity than the calculated ones.

2) For values of λ/d greater than 15, velocity data are in reasonable agreement with the effective medium theory velocity. The experimentally measured velocities decrease slightly with increasing λ/d and tend asymptotically to the long wavelength limit. The theoretical velocities reach the effective medium (long wavelength) velocity at smaller values of λ/d than the observed velocities. The observed velocities remain slightly faster than the effective medium limiting velocity.

3) The transition between short and long wavelength behavior is almost independent of the fraction of plastic and steel and occurs in a narrow range of λ/d between 8 and 15. The extreme volume fractions (0.09 and 0.89) seem to show a transition at a slightly smaller value of λ/d than the midrange of compositions. The transition value of λ/d determined numerically is still always slightly smaller than the experimental one.

The dependence of velocity on fraction of steel and plastic is summarized in Figure 3.6 on a plot of velocity versus steel fraction. Open circles represent laboratory data. Theoretical relationships for short wavelength (ray theory) and long wavelength (effective medium) behavior are shown for reference. We also superposed curves of "iso λ/d" that were calculated based on an empirical fit to the data shown in Figure 3.5a. This figure confirms that for a given value of λ/d, velocity in stratified media is strongly dependent on volume fraction. Note that in this experiment, in which λ/d spanned more than two orders of magnitude (.1-50), we were able to approach the short wavelength behavior for velocity, whereas the long wavelength limit was never reached completely by the experimental data. However, the theoretical data points do reach the long wavelength limit, as shown in Figure 3.5b.

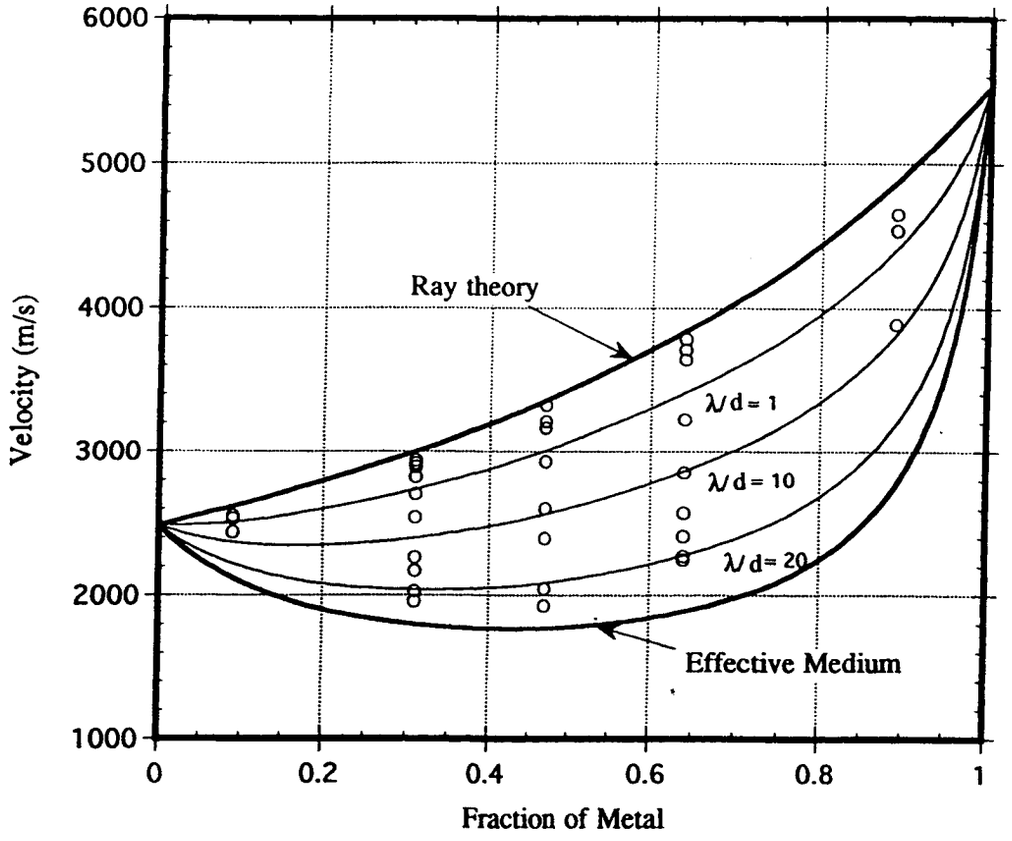

Figure 3.6: Experimentally observed velocity vs. volume fraction of steel, relative to the ray theory and effective medium theory limits. The three inner curves are empirical fits to the data at $\lambda/d = 1$, $\lambda/d = 10$, and $\lambda/d = 20$, respectively.

3.6 DISCUSSION AND CONCLUSION

In order to integrate seismic data acquired at several different scales and measurement frequencies it is essential to understand the scale-dependent effect of layering and layer spacing on wave propagation. Layered media give rise to velocity dispersion and attenuation due to scattering effects, causing wave velocities to be dependent on the ratio of wavelength to layer spacing, λ/d. We investigated this phenomenon by modeling results of laboratory experiments on periodic stacks of steel and plastic layers. Essential features of the observations could be modeled reasonably well as can be seen by a comparison of recorded and computed waveforms in Figure 3.1. Our study confirms that velocity behavior in stratified media depends on wavelength and layer spacing. We found that for plastic-steel composites, the transition from short wavelength to long wavelength behavior coincides with strong attenuation of the signal due to scattering and occurs over a narrow range of λ/d between 8 and 15. This is almost independent of relative fractions of steel and plastic, though the midrange of compositions show a transition at a slightly higher value than the extreme range of volume fractions. Previous results, obtained experimentally (Melia and Carlson, 1984) and numerically (Carcione et al., 1991) indicate that the transition takes place at a higher value for midrange of compositions. The transition region of $\lambda/d \approx 10$ is consistent with predictions of scattering theory in one-dimensional layered media (Tang and Burns, 1992). Similar behavior was also computed for other material compositions. Numerical modeling placed the transition at around $\lambda/d \approx 7$, which is consistent with the work of Carcione et al. (1991). This difference in modeling and laboratory experimental results needs to be further investigated.

We believe that the observed variation in travel time is a scale effect of λ/d, and not, for example, an accidental measurement of a bar wave because: (1) the sample length is comparable to the sample width; (2) the theoretical modeling, which reproduces the observed arrivals, assumed plane layers of infinite extent, and (3) the experiments were performed

keeping input frequency constant and only changing d, so that the ratio of input wavelength to sample dimension remained roughly the same.

It is important to realize when the difference between the ray theory and the effective medium theory velocities is large and when the difference between them might be safely ignored. An approximate estimate for the ratio of the two limiting velocities (V_{RT}/V_{EMT}) can be obtained from equation (3.6) (or its equivalents). As shown in the contour plot, Figure 3.4, for some values of density and velocity ratios of the constituent layers, it might be reasonable to ignore the dispersion effects of layered media while for some other values it could be quite important.

The importance of distinguishing the two domains — ray theory (short wavelength) and effective medium (long wavelength) — and understanding the transition between them arises from the fact that one of the key issues in reservoir characterization is the assigning of appropriate average values of seismic velocities to the various sub-units of layers that make up the reservoir. Depending on scales of layering and wave frequencies, different situations will require different interpretations, and it is not always correct just to use the Backus average.

ACKNOWLEDGEMENTS

This work was supported by the Stanford Rockphysics and Borehole Geophysics project, Gas Research Institute contract 5093-260-2703, and Department of Energy Grant DE-FG03-86ER13061. Dominique Marion and the laboratory work, which was performed with the assistance of Pierre Coudin, were supported by Elf-Aquitane. Thanks to Elf-Aquitane for permission to release the data. The authors acknowledge the many useful comments of the reviewers.

REFERENCES

Aki, K., and Richards, P. G., 1980, Quantitative seismology, theory and methods, W. H. Freeman and Co.

Auld, B. A., 1990, Acoustic fields and waves in solids, Robert E. Krieger Publ. Co.

Backus, G. E., 1962, Long-wave elastic anisotropy produced by horizontal layering: J. Geophys. Res., **67**, 4427-4440.

Berryman, J. G., 1979, Long-wave elastic anisotropy in transversely isotropic media: Geophysics, **44**, 896-917.

Carcione, J. M., Kosloff, D., and Behle, A., 1991, Long-wave anisotropy in stratified media: Geophysics, **56**, 245-254.

Christensen, R. M., 1975, Wave propagation in layered elastic media: J. Appl. Mech., **42**, 153-158.

Christensen, R. M., 1991, Mechanics of composite materials, Robert E. Krieger Publ. Co.

Claerbout, J. F., 1985, Fundamentals of geophysical data processing, Blackwell Scientific Publ.

Helbig, K., 1984, Anisotropy and dispersion in periodically layered media: Geophysics, **49**, 364-373.

Kerner, C., 1992, Anisotropy in sedimentary rocks modeled as random media: Geophysics, **57**, 564-576.

Marion, D., and Coudin, P., 1992, From ray to effective medium theories in stratified media : an experimental study: 62nd Ann. Internat. Mtg., Soc. Expl. Geophys., Expanded Abstracts, 1341-1343.

Melia, P. J., and Carlson, R. L., 1984, An experimental test of P-wave anisotropy in stratified media: Geophysics, **49**, 374-378.

O'Doherty, R. F., and Anstey, N. A., 1971, Reflections on amplitudes: Geophys. Prosp., **19**, 430-458.

Postma, G. W., 1955, Wave propagation in stratified medium: Geophysics, **20**, 780-806.

Schoenberger, M., and Levin, F. K., 1974, Apparent attenuation due to intrabed multiples: Geophysics, **39**, 278-291.

Stanke, F. E., and Burridge, R., 1993, Spatial versus ensemble averaging for modeling wave propagation in finely layered media: J. Acoust. Soc. Am., **93**, 36-41.

Sun, C. T., Achenbach, J. D., and Herrmann, G., 1968, Continuum theory for a laminated medium: J. Appl. Mech., **35**, 467-475.

Sve, C., 1971, Time-harmonic waves travelling obliquely in a periodically laminated medium: J. Appl. Mech., **38**, 477-482.

Tang, X., and Burns, D. R., 1992, Seismic scattering and velocity dispersion due to heterogenous lithology: 62nd Ann. Internat. Mtg., Soc. Expl. Geophys., Expanded Abstracts, 824-827.

Chapter 4

SCALE EFFECTS: 1-D RANDOMLY LAYERED MEDIA

VELOCITY DISPERSION AND UPSCALING IN A LABORATORY-SIMULATED VSP

ABSTRACT

A laboratory and numerical study was conducted to investigate the impact of scale-dependent seismic wave propagation in randomly layered media, as applied to sonic logs, surface seismic, and VSPs. Analysis of the laboratory results (1) confirmed the wavelength dependence of velocities inferred from travel times, (2) indicated that scale effects can introduce travel time errors when upscaling from logs to surface seismic and VSPs, and (3) illustrated that erroneous VSP interval velocities can result when layer thicknesses are smaller than about one tenth of the wavelength. A simple approximate recipe is presented for estimating these travel times by successively filtering the medium using a running Backus average and ray theory. The scale-dependent dispersion was also predicted well using a more rigorous invariant imbedding formulation. The predicted travel times, using the approximate recipe, compare well with the times observed in the laboratory stack of steel and plastic layers and in numerical studies of stratified media. The dispersion curves predicted by the approximate method also show the overall behavior computed with the more rigorous invariant imbedding formulation.

4.1 INTRODUCTION

The Earth's subsurface is heterogeneous over a broad range of scales. These heterogeneities result from variations in lithology, pore fluid, saturation, porosity, pore pressure, and stress. One problem for both seismic imaging and interpretation of these variations

is that wave propagation depends on the wavelengths used relative to the scale of the heterogeneities. Not only does the resolution depend on wavelength, but also the travel time. Hence, inferred velocities depend on the scale of measurement as well as rock and fluid properties. This chapter focuses on the geometrical heterogeneities due to layering and their influence on measurable wave velocities. Wave velocity dispersion and multiple scattering in layered media have been studied by various authors, including O'Doherty and Anstey (1971), Sve (1971), Helbig (1984), Banik et al. (1985), Resnick et al. (1986), Burridge et al. (1988), Shapiro et al. (1994), Sams and Williamson (1994), and Marion et al. (1994). Wave propagation in stratified media depends on parameters such as wave frequency, layer thicknesses, and rock properties (Marion et al., 1994 ; Mukerji et al., 1995). Depending on the ratio of seismic wavelength to layer thickness, λ/d, wave propagation varies between the fast ray theory limit ($\lambda/d \ll 1$) and the slow effective medium theory limit ($\lambda/d \gg 1$). This velocity dispersion and the accompanying attenuation due to scattering are sometimes described as a stratigraphic filtering effect (Richards and Menke, 1983; Banik et al., 1985; Frazer, 1994). The maximum value of λ/d under which ray theory is valid, and the minimum value of λ/d over which effective medium theory is valid, are still not very well defined.

Figure 4.1 shows an example of scale-dependent velocity, as discussed by Marion et al. (1994), for normal incidence propagation in periodic layered media made of plastic and steel with varying layer thicknesses. The velocity is defined as the ratio of the total length of the sample to the time for a P-wave to propagate through it (as determined from the first break time); λ is the dominant wavelength of the recorded trace, and d is the spatial period of the layering. As expected, the velocity decreases as λ/d increases. The transition between effective medium ($\lambda/d \gg 1$) and ray theory ($\lambda/d \ll 1$) behaviors occurs abruptly at around $\lambda/d \approx 20$. The same scaling behavior was found to hold for a broad range of frequencies and material volume fractions. The new experiments presented in this chapter are in randomly layered media, having a distribution (or superposition) of scales. Hence, at

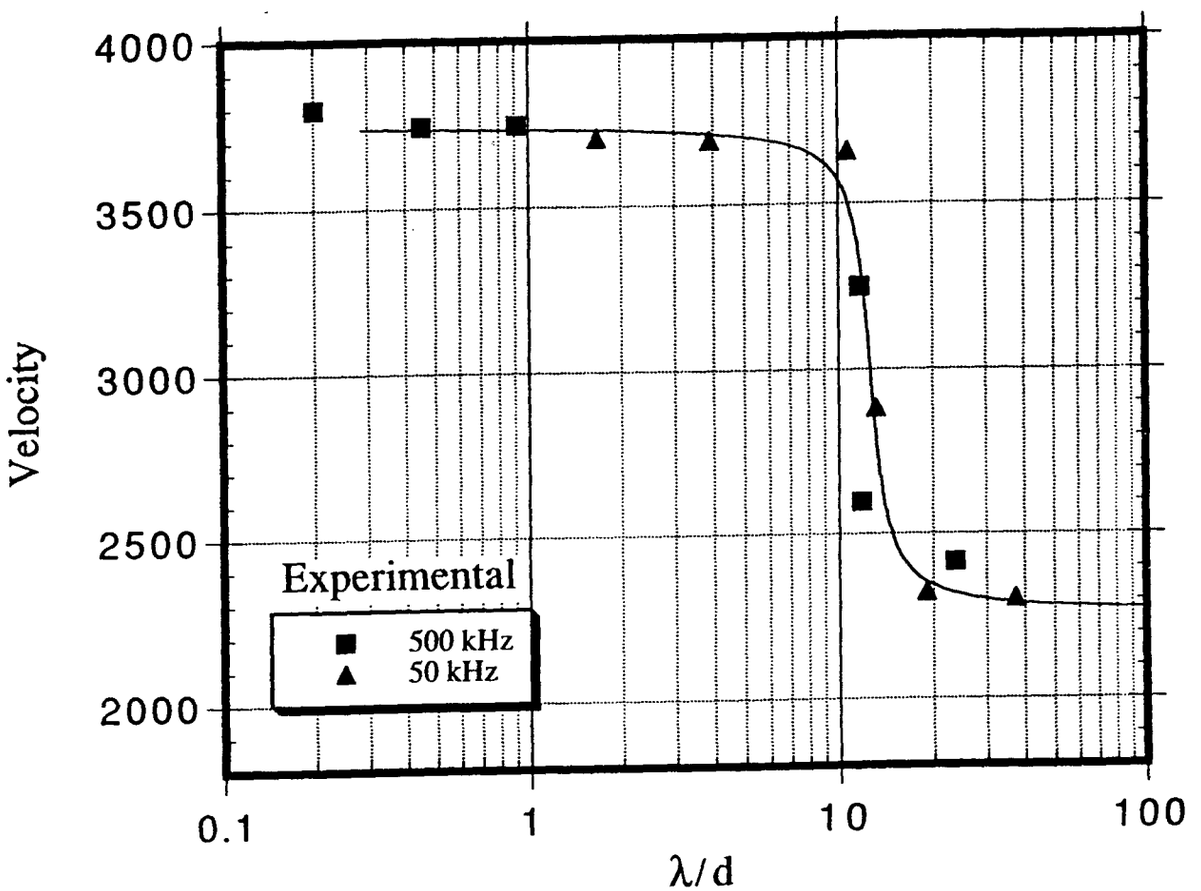

Figure 4.1: Laboratory measurements of velocity versus λ/d for a periodic layered medium made of steel and plastic (Marion et al., 1994). The smooth curve is drawn only to emphasize the trend.

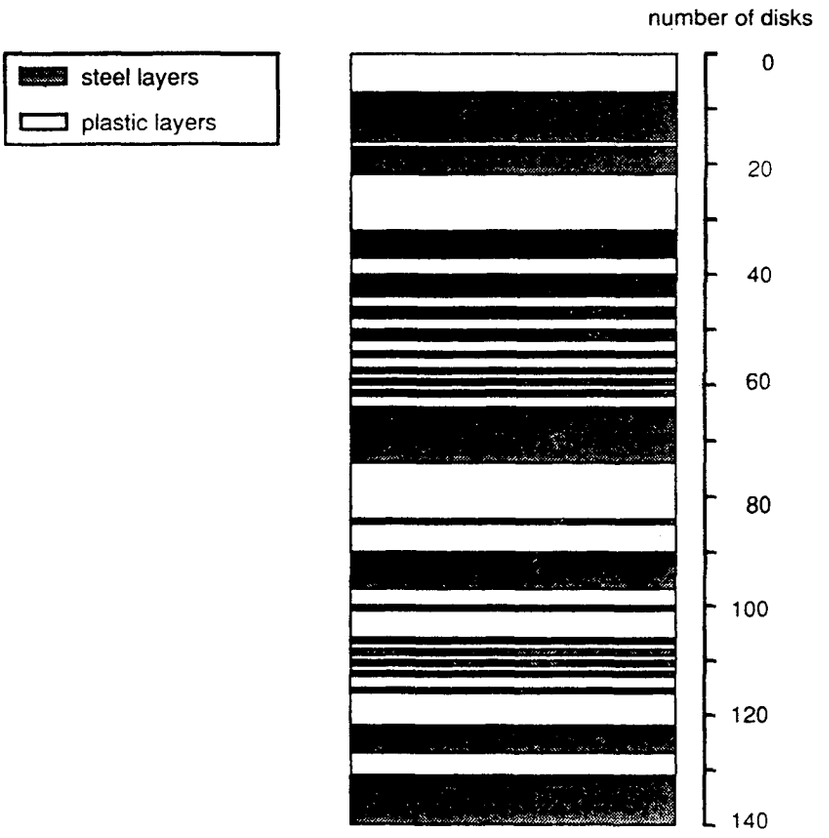

Figure 4.2: Random layered stack of steel and plastic disks used in the laboratory.

each point the wave propagation may not be describable with a single λ/d. The goals of this study were (1) to explore P-wave propagation times through a random layered medium as might be observed in VSP or surface seismic data, (2) to highlight some scale-related pitfalls of log and VSP interpretation, and (3) to develop a practical means for estimating travel times over a range of scales—for example, when upscaling from logs to surface seismic and VSP.

4.2 EXPERIMENTAL OBSERVATIONS

A layered medium for the simulated VSP was created by randomly selecting and stacking thin disks of plastic and steel (see Figure 4.2 and Table 3.1). The procedure was to begin with a single disk sandwiched between thin steel buffers. This sandwich was placed between two P-wave transducers (Panametrics 500 kHz), and the P-wave that propagated through the stack (normal to the layers) was recorded. The number of disks between the buffers was increased one by one up to a total of 140 disks. Plastic and steel disks were added in random order, resulting in a plastic-steel medium with random interval thicknesses, ranging from 1 to 10 layers ($\sim$ 0.5 to 5 mm). The probability of occurrence of each disk (plastic or steel) was independent of the previous disk, and was decided by tossing a fair coin. A total of 140 waveforms W(n) was recorded as the stack grew in size, simulating the waveforms of a VSP experiment in which the receiver moves through a range of depths. [Note: this ignores any dispersion that might result from the borehole, (Sams and Goldberg, 1990).] Honey was used between each pair of disks, and between disk and transducer, to ensure a good coupling. The volume fraction of honey in the total stack (as determined by length measurement) is about 0.8 percent. A constant normal pressure, applied by a torque wrench, held the disks together. Waveforms W(44) to W(84) are shown in Figure 4.3. Analysis of the recorded waveforms indicates a bandwidth of approximately 100-800 kHz with a dominant wavelength increasing from about 6 mm to about 24 mm (dominant frequency decreasing from 400 kHz to 100 kHz) as the wave propagates through the stack.

We estimated the travel times of the P-waves in two different ways. The first method was to pick the first break time, which we defined as the point at 5 percent of the first peak amplitude. The second method was to estimate the relative delay between each pair of adjacent traces; to do this, the waveforms were time-shifted by an amount $\Delta T = T_{exp}(n+1) - T_{exp}(n)$ that gave the best match of the waveforms in the first rise (first quarter cycle) of the wavelets. Then the total arrivals (for $n > 4$) were calculated by summing over the

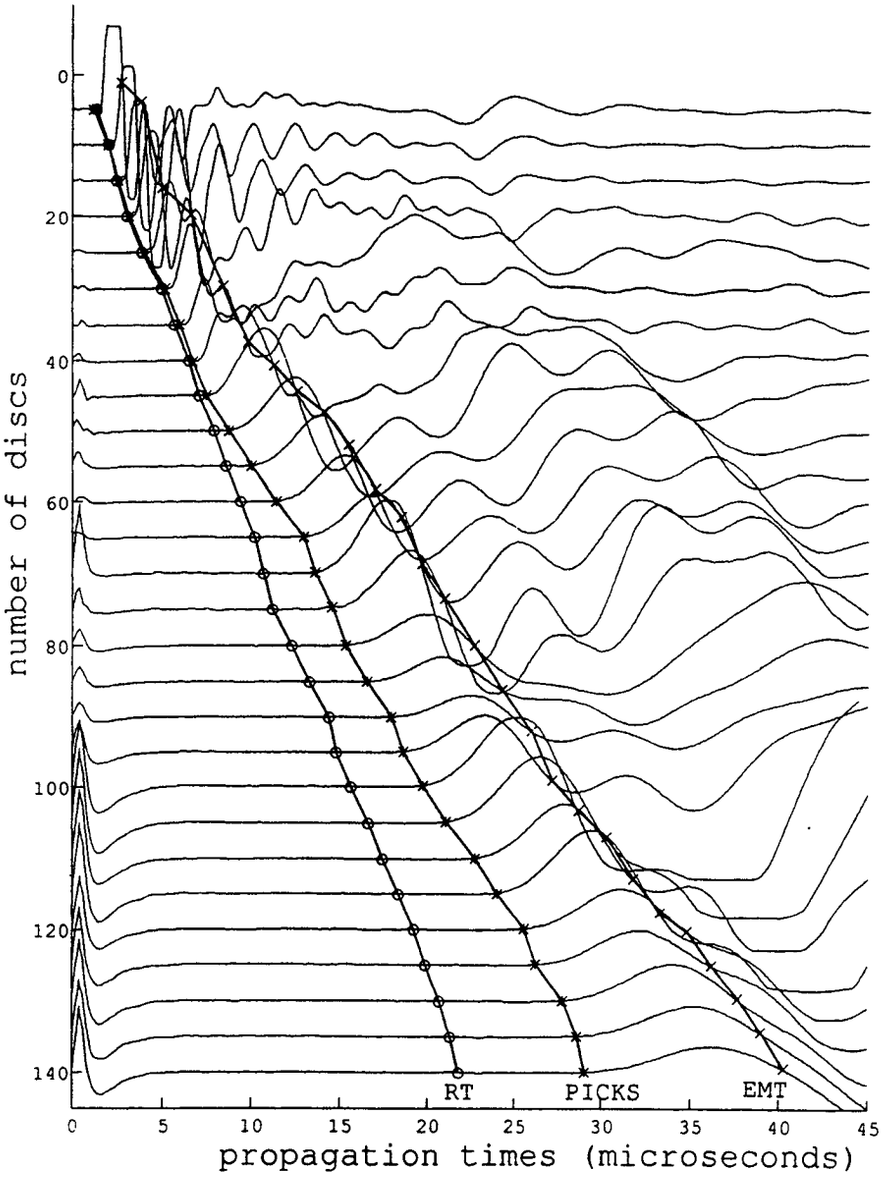

Figure 4.3: Waveforms W(44) to W(84) recorded through the plastic-steel layered medium. The picked first arrival times (5% of first peak value) and the times predicted by ray (RT) and effective medium theories (EMT) are superimposed.

relative travel times:

$$T_{exp}(n) = \left(\sum_{i=5}^{n}(T(i) - T(i-1))_{exp}\right) + T_{exp}(4) - T_{exp}(0), \tag{4.1}$$

where $T_{exp}(4)$ is measured by first break picking, and $T_{exp}(0)$ is the measured propagation time through the two steel buffers without additional layers between the two transducers. We found good agreement (less than 1 percent difference) between the two different estimates of travel time through the stack of 140 layers. The resulting picked arrival times are superimposed on the recorded waveforms in Figure 4.3. In the long wavelength limit ($\lambda/d \gg 1$), where d is some characteristic scale of the layering, we might expect the stratified medium to behave as a homogeneous effective medium. The effective medium velocity V_{emt} for plane waves propagating perpendicular to layers is given by the Backus (1962) average

$$\frac{1}{\rho_{ave}(n)V_{emt}^2(n)} = \sum_{i=1}^{n}\frac{f_i}{\rho_i V_i^2} \tag{4.2}$$

$$\rho_{ave}(n) = \sum_{i=1}^{n} f_i\rho_i, \tag{4.3}$$

where f_i are the volume fractions of the constituents (equal to the fractional layer thicknesses), ρ_i are their densities, and V_i are their velocities. The propagation time predicted by effective medium theory is given by

$$T_{emt}(n) = \frac{\sum_{i=1}^{n} l_i}{V_{emt}(n)} \tag{4.4}$$

where l_i are the thicknesses of the layers.

In the short wavelength or ray theory limit ($\lambda/d \ll 1$), the velocity is given by a harmonic average

$$\frac{1}{V_{rt}(n)} = \sum_{i=1} n \frac{f_i}{V_i}, \tag{4.5}$$

and the resulting propagation time is

$$T_{rt}(n) = \frac{\sum_{i=1}^{n} l_i}{V_{rt}(n)}. \tag{4.6}$$

Figures 4.3 and 4.4 show the experimental propagation times compared with those predicted by ray and effective medium theories, equations (4.4) and (4.6). The observed arrival time is bounded by the ray theory and effective medium theory predictions. Neither method predicts the arrival times very well after $n = 45$, although the slope of the observed times is close to the slope of the ray theory curve when the layers are thick, and is close to the slope of the effective medium theory curve when the layers are thin. This suggests that for short propagation paths, the medium can sometimes be described locally by ray or effective medium theory. However, for long paths, the observed travel time deviates from the ray theory predictions when the wave propagates through thin layers, and the cumulative deviations increase with increasing pathlength. This illustrates very clearly the following caveat: *large discrepancies can occur if we simply apply either ray theory or effective medium theory (the Backus average) to integrate a sonic log to estimate the arrival times of a VSP or surface seismic trace.*

4.3 INTERVAL VELOCITIES

Figure 4.5a shows apparent interval velocities in plastic layers. The apparent velocity

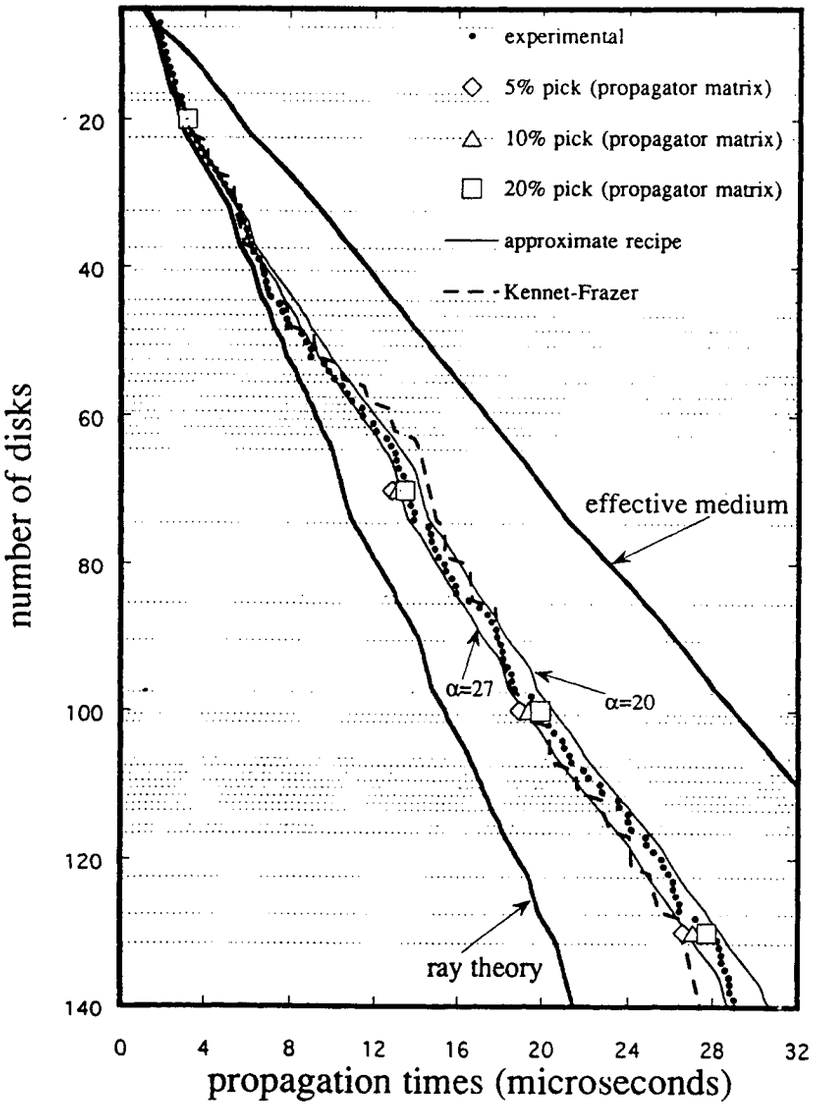

Figure 4.4: Experimental propagation times versus number of disks, compared with ray theory and effective medium theory predictions (same as Figure 4.3). Times computed with a propagator matrix method (picked at 5, 10, and 20 percent of the first peak) are shown at layers 20, 70, 100, and 130. Times predicted by the Kennett-Frazer theory and our approximate recipe are also shown. The dotted lines indicate the steel-plastic interfaces.

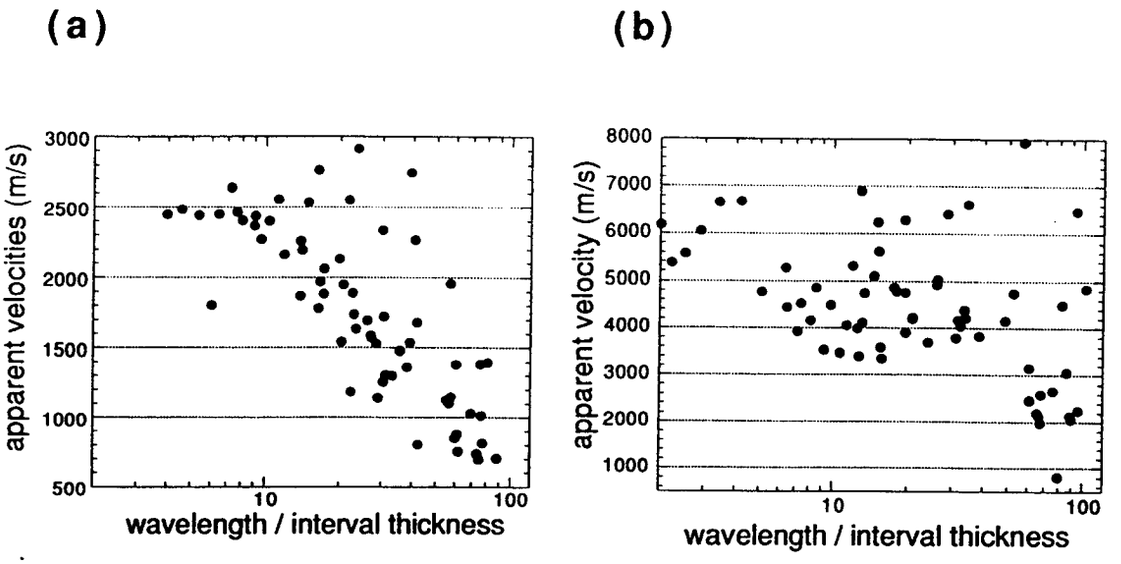

Figure 4.5: (a) Apparent velocities in plastic layers versus the ratio of wavelength to interval thickness. (b) Apparent velocities in steel layers versus the ratio of wavelength to interval thickness.

is estimated for each n-layered section of the stack that ends with plastic, and is given by the thickness of the plastic interval divided by the difference in picked arrival times of the waveforms at the beginning and end of the interval. Note that the apparent velocity generally gives a good estimate of the true interval velocity for plastic (2487m/s) when the interval thickness is larger than about $\lambda/10$, (where λ is the dominant wavelength of the recorded signal), but tends to seriously underestimate the interval velocity when the interval is thinner. This common method of estimating the apparent interval velocity is a ray theory estimate, and as shown in Figure 4.1, ray theory explains well the experimental apparent velocities only when $\lambda/d < 10$; for shorter intervals the propagation time is influenced also by the neighboring layers. At very short pathlengths, small uncertainties in the picks can cause large changes in the estimated apparent interval velocities.

Figure 4.5b shows the apparent interval velocities computed in the same way for steel layers. The interval estimates cluster roughly around the true interval velocity (5535 m/s) only for the intervals thicker than about $\lambda/10$. The velocities show much more scatter over the entire range than in Figure 4.5a, because in steel the interval travel times are smaller and are comparable to the errors in time picks.

4.4 UPSCALING

As illustrated in Figures 4.3 and 4.4, VSP and surface seismic travel times can not always be predicted from high resolution interval velocities (as might be inferred from sonic logs) with either ray theory or effective medium theory alone. The problem is that in a random medium both large and small scale heterogeneities are superimposed, and the wave simultaneously "senses" both.

One approach to this upscaling problem is to predict travel times using full waveform modeling, such as invariant imbedding and generalized ray methods (Kennett, 1974;

Resnick et al., 1986), finite difference (Kerner, 1992), finite element (Kuo and Teng, 1983), or propagator matrix (Tang et al., 1992; Marion et al., 1994) methods. Figure 4.4 shows arrival times computed with a propagator matrix code through the known laboratory plastic-steel sequence. These times were estimated by first computing the theoretical plane wave, normal incidence waveforms at 4 locations along the medium. The incident wavelet was taken to be the same as the laboratory input wavelet. Points at 5, 10, and 20 percent of the first peak amplitude were picked on the output waveforms and compared with the same points on the input waveform. The theoretical arrival times tend to be slightly earlier than the laboratory picks, but in general they agree quite well. The different methods of picking yield slightly different apparent velocities. We find from the synthetic waveforms that first break picks made at a very small fraction of the peak amplitude yield slightly faster velocities, that are close to the phase velocities inferred from the phase of the cross-spectrum (Jenkins and Watts, 1968) of the computed and input waveforms. Picks at a larger fraction of the peak amplitude or from cross-correlation of waveforms (not shown) yield slightly slower velocities. Nevertheless, in this case (Figure 4.4) the difference among the estimated arrival times is small relative to the difference between ray and effective medium theories, and all are clearly consistent with the result that neither ray theory nor effective medium theory can adequately predict the arrivals. We believe that this scale-dependent dispersion is one source of the mismatch of log and surface seismic travel times (sonic drift).

We used the propagator matrix method to compute normal incidence, plane wave seismograms in several synthetic random layered media. The three synthetic media, each consisting of 200 layers, were: (a) a Poisson sequence of fast and slow layers with interval thicknesses drawn from a Poisson distribution, (b) a randomly layered sequence with a Gaussian spatial autocorrelation, and (c) a fractal sequence with a spectral exponent of 0.8 ($1/f^{0.8}$). The standard deviations of the velocity fluctuations were 50 percent for the Poisson medium and about 30 percent for the Gaussian and fractal media. These types of layers

are representative of natural geologic stratification and have been used for modeling depositional sequences and well logs (Kerner, 1992; Hewett and Behrens, 1988; Hewett, 1992). The same input wavelet was used for all three synthetic models, with a dominant wavelength $\lambda \sim 25d$, where d is a characteristic length scale of the layering. For the Gaussian medium, this is the correlation length, while for the Poisson medium it is the mean layer thickness. The fractal sequence, of course, does not have any single intrinsic scale; therefore for the fractal medium d was taken as the thickness of a single layer. Figure 4.6 shows the computed waveforms propagated through the three synthetic media, along with the predicted ray theory and effective medium travel times. The first arrivals lie between the two limits, although for the Gaussian medium, with the chosen wavelength, they are very close to the ray theory predictions. Figure 4.7 shows the travel times estimated from first break picks (at 1 percent of peak amplitude) of the computed waveforms. The picks were found to be close to travel times estimated from the cross-spectrum phase of the input and output waveforms. We again observe that for the wavelengths chosen, the first break travel times fall between the ray theory and effective medium predictions.

When choosing a numerical method one should, of course, be cautious of waveform modeling packages that might have built-in high frequency (ray theory) approximations. Furthermore, strong material contrasts across very sharp boundaries can be numerically troublesome. Therefore it is advantageous to have a simple recipe for estimating travel times in layered media without having to compute and pick a whole suite of synthetic waveforms.

A number of authors have analyzed theoretically the velocity dispersion in stratified media. Shapiro et al. (1994) have presented analytic expressions for scale-dependent travel times in a randomly layered medium, based on a scattering and wave localization approach. The average dispersion is computed from the spatial correlation functions of the velocity and density of the medium. The limitations of these expressions are that (1) they are strictly valid only for infinite pathlengths, (2) they assume a statistically stationary geology along the entire travel path, and (3) they assume small perturbations in the material parameters.

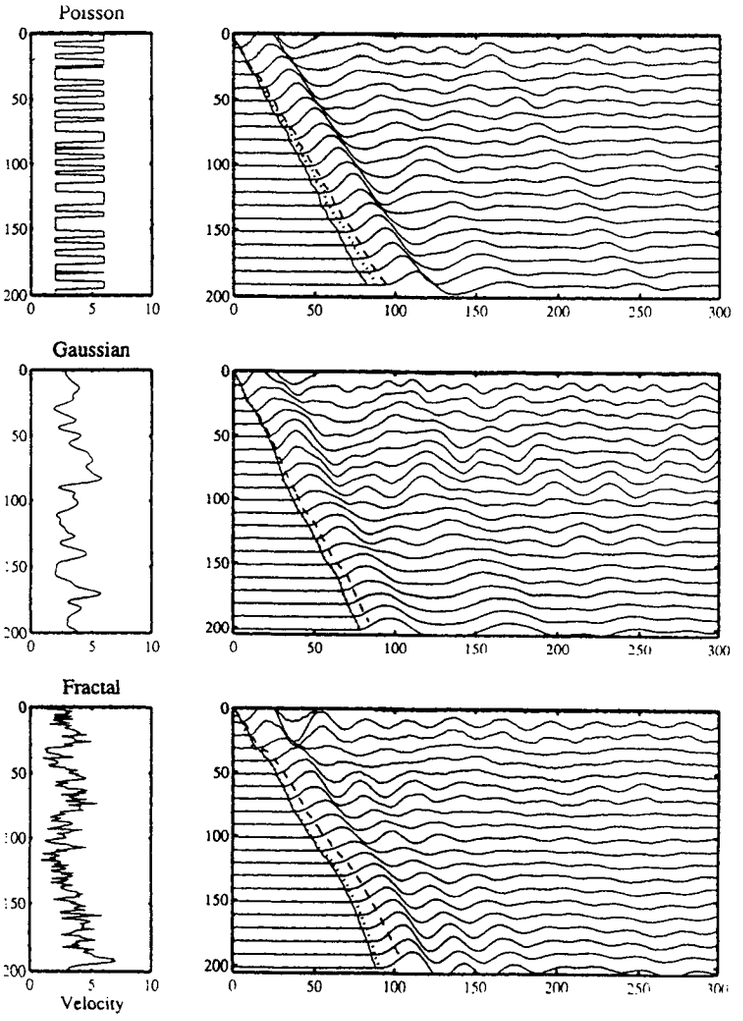

Figure 4.6: Synthetic waveforms computed in Poisson, Gaussian, and Fractal media. The picked first arrival time (dotted line) and the times predicted by ray (solid line) and effective medium (dashed line) theories are superimposed. (For the Gaussian medium, the picks and ray theory curve coincide.) Velocity versus depth functions are shown on the left for each model.

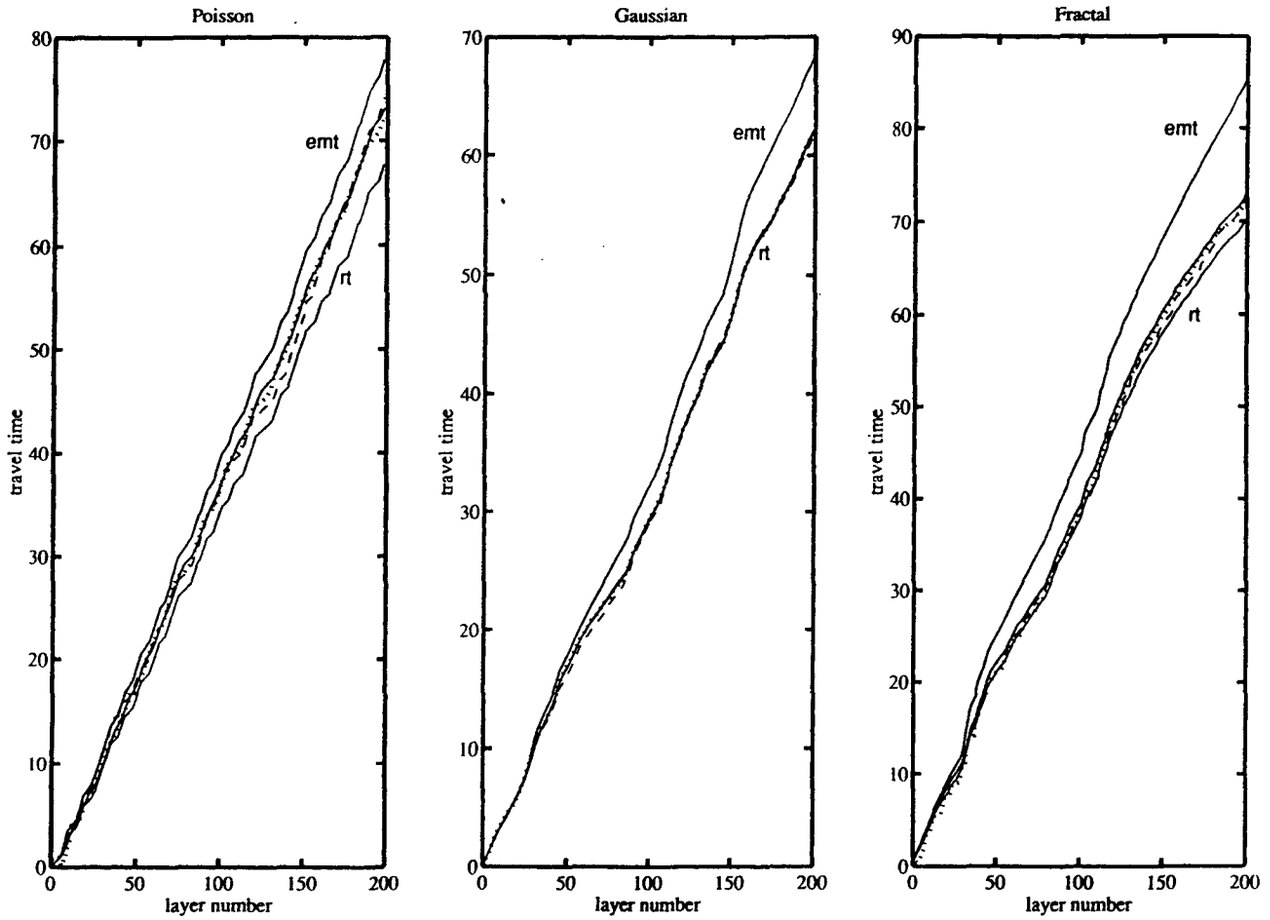

Figure 4.7: Arrival times (dotted line) picked from the synthetic waveforms in Figure 4.6, compared with predictions of effective medium (emt) and ray theories (rt), the Kennett-Frazer theory (dashed line), and our heuristic two-step recipe (solid line).

Our laboratory simulations have finite pathlengths and large material contrasts, so these expressions cannot be applied here. Banik et al. (1985), using Keller's (1960) mean field theory, presented a formulation for calculating the dispersion caused by thin layers, also limited to small material perturbations. This result is for the velocity of the ensemble averaged wavefield, which does not always give a good estimate of the first break time for a specific realization of the wave (Stanke and Burridge, 1992). Furthermore, since the Shapiro et al. (1994) and Banik et al. (1985) relations are based on a stochastic formulation, they predict the average dispersion over a long path and cannot predict the local fluctuations and non-stationary behavior that we observe in Figure 4.4.

A more flexible approach follows from Kennett's (1974) invariant imbedding formulation for the transfer function of a layered medium. The stratigraphic slowness and excess travel time that arise from multiple scattering of normal incidence waves in layered media are calculated iteratively (Frazer, 1994). The total travel time is $T = T_{rt} + T_{st}$ where T_{st} is given by (Frazer, 1994)

$$T_{st} = Re\left\{\frac{1}{i\omega}\sum_{j=1}^{n}\ln\left[\frac{t_j}{1 - R_j\theta_j^2 r_j}\right]\right\}. \tag{4.7}$$

As each new layer $j+1$ is added to the stack of j layers, R is updated according to:

$$R_{j+1} = -r_{j+1} + \frac{R_j\theta_{j+1}^2 t_{j+1}^2}{(1 - R_j\theta_{j+1}^2 r_{j+1})}, \tag{4.8}$$

(with $R_0 = 0$) and the term $\ln[t_{j+1}(1 - R_{j+1}\theta_{j+1}^2 r_{j+1})^{-1}]$ is accumulated in the sum. In the above expressions, t_j and r_j are the transmission and reflection coefficients

$$t_j = \frac{2\sqrt{\rho_j V_j \rho_{j+1} V_{j+1}}}{\rho_j V_j + \rho_{j+1} V_{j+1}}, \tag{4.9}$$

$$r_j = \frac{\rho_{j+1} V_{j+1} - \rho_j V_j}{\rho_{j+1} V_{j+1} + \rho_j V_j}, \tag{4.10}$$

where $\theta_j = \exp(i\omega l_j / V_j)$ is the phase shift for propagation across layer j, and ω is the radian frequency. This deterministic estimate of the travel time is not restricted to small perturbations in the material properties or statistically stationary geology. We find that the travel times computed from equations (4.7)-(4.10), for a frequency equal to the highest frequency present in the input wavelet, agree well with those picked in the laboratory (Figure 4.4) and for the synthetic media (Figure 4.7).

We used the Kennett-Frazer formulation to analyze also the velocity dispersion in the three synthetic layered media. Figure 4.8 shows the velocity dispersion curves (dashed) as a function of λ for each of these synthetic media. The curves were calculated using equations (4.7)-(4.10). As expected, at very short wavelengths, the velocities go to the ray theory value while at very long wavelengths they tend towards the effective medium value. However, the nature and slope of the transition is different for the different media. It is gradual for the Gaussian and fractal media, while the Poisson medium shows a more abrupt transition. Note also that the transitions occur at slightly different scales for the different types of medium. For the Poisson medium, the velocity departs from effective medium behavior at approximately $\lambda \approx 10d$, where d is the average layer thickness. For the Gaussian medium, the same point occurs at $\lambda \approx 100d$, where d is now the spatial correlation length. For the fractal medium, the transition occurs at an even larger wavelength, although for fractal media we cannot specify an intrinsic scale, so we took d to be the individual layer thickness.

We now suggest an even simpler, approximate technique for estimating normal incidence propagation times and dispersion in layered media that can have a wide range of layer

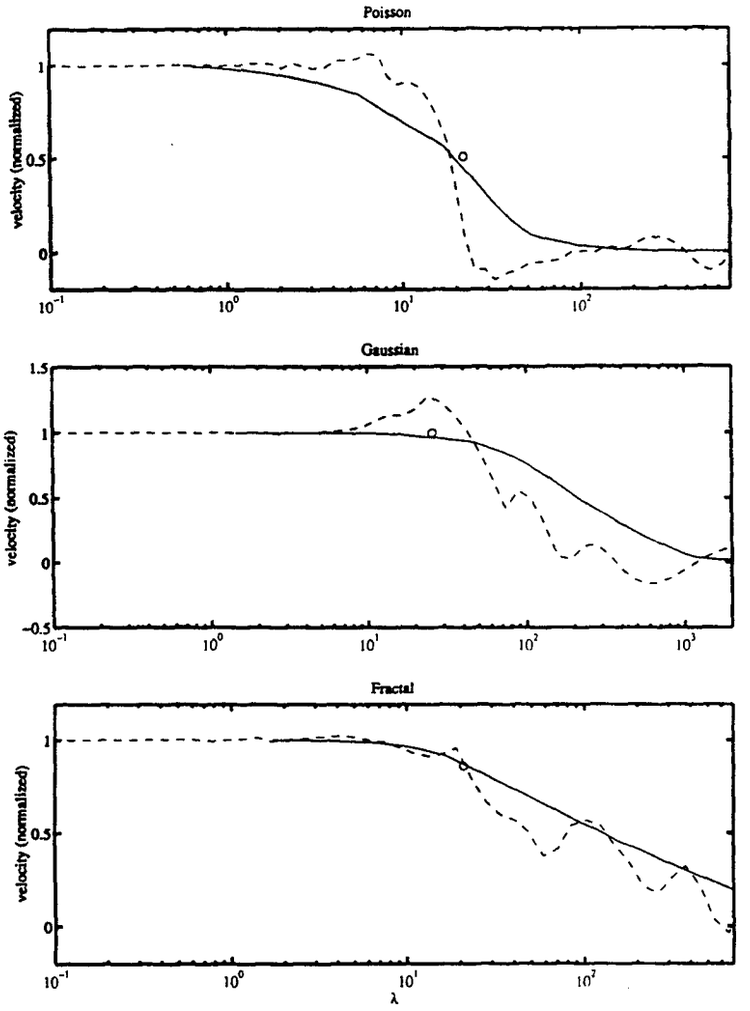

Figure 4.8: Velocity dispersion curves computed for the Poisson, Gaussian, and Fractal media using the Kennett-Frazer theory (dashed) and our approximate recipe (solid). The velocity obtained from the propagator matrix waveform (in Figure 4.6) at the end of the layers is indicated by the open circle. The normalized velocity is given by$(V - V_{EMT})/(V_{RT} - V_{EMT})$.

thicknesses and material contrasts. The method follows heuristically from Figure 4.1, where we note the abrupt transition from effective medium to ray theory behaviors at $\lambda/d = \alpha$, where in this case $\alpha \approx 20$. We imagine that at any point a seismic wave "senses" spatial scales that fall, for the most part, either into the ray or the effective medium domain. The recipe then proceeds in two steps. In the first step we eliminate (approximately) any spatial scales smaller than λ/α by applying a running Backus (1962) average of length $L = \lambda/\alpha$ over the medium. This is applied with a running average with uniform weights over the density, $\rho(z)$, and P-wave compliance depth series, $[M(z)]^{-1} = [\rho(z)V^2(z)]^{-1}$, yielding a smoothed modulus $\overline{M}(z)$, and density $\overline{\rho}(z)$ from which we calculate the smoothed velocity function $\overline{V}(z) = \sqrt{\overline{M}(z)/\overline{\rho}(z)}$. The new velocity function $\overline{V}(z)$ represents at every point the local effective medium equivalent of the original layered medium in a window of length$L$, as discussed by Kerner (1992). The next step is to estimate the travel time through the smoothed medium over the total path (generally longer than L) using ray theory:

$$T(n) = \sum_{i=1}^{n} \frac{l_i}{\overline{V}_i}. \tag{4.11}$$

Thus the recipe consists of two simple sequential filters applied on the velocity-depth series. It is somewhat analogous to the common practice of blocking a log before computing a synthetic seismogram. If we have only fine scales in the medium, then the running average results in a homogeneous effective medium; if there are only long scales in the medium then the running average has essentially no effect. In any case, the medium smoothed with effective medium theory can then be more appropriately treated with ray theory. Windowed Backus averaging was used by Sams and Williamson (1994) to study sonic drift.

The result of applying the recipe to the laboratory sequence is shown in Figure 4.4, where we find that an α between 20 and 30 reproduces the observed times quite well—essentially the same as the Kennett-Frazer prediction, and certainly much better than either

the ray theory or effective medium theory estimates. The filtering effect of the layered medium causes the dominant wavelength to increase with increasing path length. Therefore in this example we used an averaging window λ/α that increases with propagation distance. However, we found that a simple fixed length square window gives comparable results although the results using a variable window are slightly more consistent with the observed travel times. Other window shapes and types has been investigated by Sams and Williamson (1994).

We tested the recipe by comparing it with numerical simulations of wave propagation in the three different synthetic randomly layered media. Figure 4.7 shows that the travel time estimates using our recipe closely follow the observed propagation times, and agree quite well with the more rigorous Kennett-Frazer predictions. An α of order 30-50 gives good results for the Poisson medium, while an α of order 100-150 works well for the Gaussian and fractal media. Figure 4.8 shows the velocity dispersion as a function of wavelength using our approximate recipe (solid lines), compared with the Kennett-Frazer curves discussed earlier. An α of 40 was used for the Poisson medium while 100 and 120 were used for the Gaussian and fractal sequences, respectively. The figure also shows the velocity calculated from the propagator matrix waveform (shown in Figure 4.6) at the end of the stack of layers. The approximate curves reproduce the general trends quite well. When using the approximate recipe, there is the practical problem of picking the appropriate value of the Backus window length. We found empirically that for bi-modal velocity distributions (such as that in the laboratory medium and in the Poisson sequence) an α of 20 to 50 worked well, while for the continuous distributions (the Gaussian and fractal) an α of 100 to 150 worked well. This reflects the same shift in the scale of the transition from ray to effective medium behavior that is predicted by the Kennett-Frazer theory, and is apparently determined by the different types of medium.

4.5 CONCLUSION

Our laboratory-simulated VSP and numerical experiment show that neither ray nor effective medium theories can accurately explain wave propagation times in a randomly layered medium with a wide range of layer thicknesses relative to the seismic wavelength. In practice, wave propagation in layered media is dispersive, ranging between the fast, short wavelength limit described by ray theory and the slower, long wavelength limit described by effective medium theory. The results indicate that the scale effects can introduce travel time errors when upscaling from logs to surface seismic and VSPs, and is probably one cause of the often observed sonic drift. The results also indicate that erroneous interval velocities can result from VSP and seismic travel times when interval thicknesses are much smaller than the seismic wavelength. The travel time can be predicted with a full-waveform modeling method, such as finite difference or propagator matrix. However, it is advantageous to have some means of calculating the travel times without having to compute and pick a stack of synthetic waveforms. Some of the stratigraphic filtering methods, based on a stochastic description, such as those presented by Banik et al. (1985) and Shapiro et al. (1994), can account for the average dispersion over a very long path length, but cannot account for observed local fluctuations, such as a speed up when layers are thick and a slow down when thin. Furthermore, many of these formulations are limited to small material contrasts. A more flexible approach follows from the invariant imbedding formulation of Kennett (1974) and Frazer (1994). We have shown that this can predict quite well the laboratory- simulated VSP, as well as numerically-simulated travel times in Poisson, Gaussian, and fractal randomly layered media. Finally, a simple approximate recipe for predicting the scale-dependent travel time was suggested that successively filters the medium using a running Backus average and then applying ray theory. It appears to accurately estimate the seismic arrival time when neither ray theory nor effective medium theory can be used, and predicts quite well both the laboratory and numerically-simulated travel

times and velocity dispersion.

ACKNOWLEDGEMENTS

This work was supported by the Stanford Rock and Borehole Geophysics project, Elf-Aquitaine, and Gas Research Institute Contract: 5093-260-2703. Thanks to Elf-Aquitane for permission to release the data. The laboratory work was performed with the assistance of Olivier Crot at Elf. Ken Mahrer's suggestions for improving the manuscript, especially the abstract, were very helpful. We would also like to thank the reviewers, including Dan Ebrom, for their useful comments, and for bringing to our notice the work of Sams and Williamson.

REFERENCES

Backus, G. E., 1962, Long-wave elastic anisotropy in transversely isotropic media, Geophysics: **44**, 896-917.

Banik, N. C., Lerche, I., Resnick, J. R., and Shuey, R. T., 1985, Stratigraphic filtering, part I & II: Geophysics, **50**, 2768-2783.

Burridge, R., Papanicolaou, G., and White, B., 1988, One-dimensional wave propagation in a highly discontinuous medium: Wave Motion, **10**, 19-44.

Frazer, L. N., 1994, A pulse in a binary sediment: Geophys. J. Int., **118**, 75-93.

Helbig, K., 1984, Anisotropy and dispersion in periodically layered media: Geophysics, **49**, 364-373.

Hewett, T.A. and Behrens, R.A., 1988, Conditional simulation of reservoir heterogeneities with fractals, Proceedings SPE Annual Technical Conference and Exhibition, Houston, SPE Vol 1988, 645-660.

Hewett, T.A., 1992, Modelling reservoir heterogeneities with fractals: Proceedings of 4th International Geostatistics Congress Sept. 13-18, Lisbon, in Terra Abstracts, 4, Suppl. 3, 9.

Jenkins, G. M., and Watts, D. G., 1968, Spectral analysis and its applications: Holden-Day, San Francisco.

Keller, J. B., 1960, Wave propagation in random media: Proc. Symp. Appl. Math., **XIII**, 769-783.

Kennett, B. L. N., 1974, Reflections, rays and reverberations: Bull. Seism. Soc. Am., **64**, 1685-1696.

Kerner, C., 1992, Anisotropy in sedimentary rocks modeled as random media: Geophysics, **49**, 364-373.

Kuo, J. T., and Teng, Y. C., 1983, Three-dimensional finite element modeling of acoustic and elastic waves: Geophysics, **48**, 485.

Marion, D., and Coudin, P., 1992, From ray to effective medium theories in stratified media: an experimental study: 62nd Ann. Internat. Mtg., Soc. Expl. Geophys., Expanded Abstracts, 1341-1343.

Marion, D., Mukerji, T., and Mavko, G., 1994, Scale effects on velocity dispersion: from ray to effective medium theories in stratified media: Geophysics, **59**, 1613-1619.

Mukerji, T., Mavko, G., Mujica, D., and Lucet, N., 1995, Scale-dependent seismic velocity in heterogeneous media: Geophysics, **60**, 1222-1233.

O'Doherty, R. F., and Anstey, N. A., 1971, Reflections on amplitudes: Geophys. Prosp., **19**, 430-458.

Resnick, J. R., Lerche, I., and Shuey, R., 1986, Reflection, transmission and the generalized primary wave: Geophys. J. Int., **87**, 349-387.

Richards, P. G., and Menke, W., 1983, The apparent attenuation of a scattering medium: Bull. Seism. Soc. Am., **73**, 1005-1021.

Sams, M. S., and Goldberg, D., 1990, The validity of Q estimates from borehole data using spectral ratios: Geophysics, **55**, 97-101.

Sams, M.S., and Williamson, P. R., 1994, Backus averaging, scattering and drift: Geophys. Prosp., **42**, 541-564.

Shapiro, S. A., Hubral, P., and Zien, H., 1994, Frequency-dependent anisotropy of scalar waves in a multilayered medium: J. Seis. Explor., **3**, 37-52.

Shapiro, S. A., and Zien, H., 1993, The O'Doherty-Anstey formula and localization of seismic waves: Geophysics, **58**, 736-740.

Stanke, F. E., and Burridge, R., 1992, Spatial versus ensemble averaging for modeling wave propagation in finely layered media: J. Acoust. Soc. Am., **93**, 36-41.

Sve, C., 1971, Time-harmonic waves travelling obliquely in a periodically laminated medium: J. Appl. Mech., **38**, 467-475.

Tang, X., Reiter, E. C., and Burns, D. R., 1992, Estimating formation shear velocity from dispersive logging waveforms using a model-guided processing technique: 62nd Ann. Internat. Mtg., Soc. Expl. Geophys., Expanded Abstracts, 205-207.

Chapter 5

SCALE EFFECTS IN 2 AND 3-D

SCALE-DEPENDENT SEISMIC VELOCITY IN HETEROGENEOUS MEDIA

ABSTRACT

The measurable traveltimes of seismic events propagating in heterogeneous media depend on the geologic scale, the seismic wavelength, and the propagation distance. In general, the velocity inferred from arrival times is slower when the wavelength is longer than the scale of heterogeneity and faster when the wavelength is shorter. For normal incidence propagation in stratified media, this is the difference between averaging seismic slownesses, in the short wavelength limit, and averaging elastic compliances, in the long wavelength limit. In two and three dimensions there is also the path effect. Shorter wavelengths tend to find faster paths, thus biasing the traveltimes to lower values. In the short wavelength limit, the slowness inferred from the average traveltime is smaller than the mean slowness of the medium. When the propagation distance is much larger than the scale of the heterogeneity the path effect causes the velocity increase from long to short wavelength to be much larger in two dimensions than in one dimension, and even larger in three dimensions. The amount of velocity dispersion can be understood theoretically, but there is some discrepancy between theory and experiment as to what ratio of wavelength to heterogeneity scale separates the long and short wavelength limits. The scale-dependent traveltime has several implications for seismic measurement and interpretation: The measured velocity depends not just on the rock properties, but also on the scale of the measurement relative to the scale of the geology. When comparing measurements made at different scales, for example logs and surface seismic, it is not always correct simply to apply the Backus average; the correct procedure will vary from case to case with the scale of the geology. Scale effects must be included with other viscoelastic mechanisms of dispersion when comparing measurements made at different frequencies. The amount of observed scale-dependent dispersion also depends on the spatial resolution of the receiver array. For example, the first-break time of

the average trace from a stack, a large group array, or a large laboratory transducer may be earlier than the average of first-break times measured with individual small-scale receivers.

5.1 INTRODUCTION

Seismic methods provide the primary geophysical tools for detecting and imaging reservoir heterogeneities. These heterogeneities include variations in lithology, porosity, permeability, pore fluid properties, and conditions of pore pressure, temperature, and stress. They occur over a broad range of scales, from submillimeter grain and pore scale, to the many-kilometer basin scale. Similarly, seismic measurement scales range from millimeter wavelengths in ultrasonic laboratory measurements, to tens of meters in surface seismic. An important issue for interpreting geophysical images is that the seismic wave propagation is itself affected by the heterogeneities. For example, seismic arrival times, from which velocities are determined, depend on the scale of heterogeneities relative to the seismic wavelength. The distribution of arrival times along an array of receivers also depends on wavelength and receiver spacing relative to the scale of the medium.

Numerous theoretical, computational, and experimental studies have dealt with wave propagation in inhomogeneous media, both in one-dimensional layered media (e.g. Backus, 1962; Sun et al. 1968; O'Doherty and Anstey, 1971; Christensen, 1975; Helbig, 1984; Melia and Carlson, 1984; Carcione et al. 1991; Kerner, 1992; Marion and Coudin, 1992; Stanke and Burridge, 1993; Marion et al., 1994) and in two and three-dimensional random media, (e.g. Chernov, 1960; Keller, 1964; Ishimaru, 1978; Sobczyk, 1985; Frankel and Clayton, 1986; Müller et al., 1992). In random media, the scale of the heterogeneities is often described in terms of the spatial correlation length, a, of the medium. Some of the

studies have dealt with the effective properties of heterogeneous media in the long wavelength limit, $\lambda/a \gg 1$, where λ is the seismic wavelength (Berryman, 1979, 1980; Carcione et al., 1991; Ikelle et al., 1993); others have focussed on the attenuation due to scattering effects which are largest when $\lambda/a \approx 1$ (Wu and Aki, 1985; Jannaud et al., 1991; Roth and Korn, 1993; Shapiro and Kneib, 1993); and still others have investigated the ray-theoretical aspects when $\lambda/a \ll 1$ (Boyse, 1986; Frankel and Clayton, 1986; Müller et al., 1992).

Measurable velocities in the short wavelength limit, ($\lambda/a \ll 1$), are generally faster than in the long wavelength limit ($\lambda/a \gg 1$). In the simple case of normal incidence propagation in layered media, this is the difference between averaging seismic slownesses versus averaging elastic compliances (Marion et al., 1994). However in two and three dimensions there is also the path effect: as the wavelength shortens, waves tend to find fast paths, diffracting around slower inhomogeneities, thus biasing the traveltimes to lower values (Wielandt, 1987; Nolet, 1987; Petersen, 1990; Müller et al., 1992; Korn, 1993). This is sometimes referred to as the "Wielandt effect", "fast path effect" or "velocity shift". The value of λ/a that separates the long and short wavelength limits is still a matter of controversy and research, with $\lambda/a \sim 3$ (Helbig, 1984) from theoretical considerations, $\lambda/a \sim 5 - 8$ from numerical modeling (Carcione et al. 1991), and $\lambda/a \sim 10$ from experiments (Melia and Carlson, 1984; Marion and Coudin, 1992). The value also depends on the nature of the spatial correlation function (Rio et al., 1995), and in some cases may be of the order of 100 to 1000 (Kerner, 1992).

In this chapter we explore theoretically, numerically, and experimentally the scale-dependence of observable velocities in heterogeneous media, and in particular the transition between the long and short wavelength limits. We start by reviewing normal incidence propagation in layered media, the simplest one-dimensional system illustrating the decrease of traveltime with decreasing wavelength. Next, we consider two-dimensional and three-dimensional behavior, where the path effect can cause a much larger speed-up with decreasing wavelength. Finally, we discuss implications for laboratory and field measurements of

seismic traveltime.

In seismic measurements we almost never measure elastic constants or velocities directly. Instead we most often measure times of wave arrivals, and infer the velocities from the ratio of distance to traveltime. Therefore, our emphasis here is on *measurable* scale-dependent arrival times of band-limited events, as we would encounter in the lab or in the field. The long and short wavelength limiting behavior is easily understood theoretically in terms of phase and group velocities, but we will infer the transition behavior primarily from the physical and numerical modeling studies.

5.2 RAY THEORY AND EFFECTIVE MEDIUM BEHAVIOR — 1-DIMENSION

In a recent paper Marion et al., (1994) explored normal incidence wave propagation in stratified media as the simplest, one-dimensional illustration of scale effects on velocity. In the long wavelength limit, $\lambda/a \gg 1$, where λ is seismic wavelength and a is the scale of the layering, a stratified medium behaves as a homogeneous effective medium with velocity of plane wave propagation normal to the layering given by:

$$V_{EMT} = \left(\frac{M_{EMT}}{\rho_{ave}} \right)^{1/2} . \tag{5.1}$$

The effective modulus, M_{EMT}, is obtained from the Backus average (Backus, 1962) of the elastic stiffness tensors C_{ijkl} of the constituents. For normal incidence propagation this is equivalent to the harmonic average:

$$M_{EMT} = \left[\sum_k \frac{f_k}{M_k}\right]^{-1} \tag{5.2}$$

or

$$\frac{1}{\rho_{ave} V_{EMT}^2} = \sum_k \frac{f_k}{\rho_k V_k^2} \tag{5.3}$$

where f_k, ρ_k, M_k, and V_k are the volume fractions, densities, moduli, and velocities of each constituent, respectively. M can be interpreted as C_{3333} for P-waves and as C_{2323} for S-waves. The average density, ρ_{ave}, is:

$$\rho_{ave} = \sum_k f_k \rho_k. \tag{5.4}$$

In the ray theory or short wavelength limit ($\lambda/a \ll 1$), the total traveltime for plane waves travelling perpendicular to the layers is the sum of the traveltimes through each layer. The ray theory average velocity through the medium is therefore:

$$\frac{1}{V_{RT}} = \sum_k \frac{f_k}{V_k}. \tag{5.5}$$

Note that ray theory velocities, equation (5.5), involve averaging slownesses, while effective medium velocities, equations (5.2) and (5.3), involve averaging compliances (slowness squared). This results in the long wavelength (effective medium) velocity always being slower than the short wavelength (ray theory) velocity. In these two limiting cases, phase and group velocities are the same for normal incidence propagation although they differ in the transition region. Thus, both the phase and the group velocities are faster in the short

wavelength limit, [equation (5.5)], than in the long wavelength, effective medium limit [equation (5.1)]. An important point to note is that the exact Floquet solution for normal incidence phase velocity for wave propagation in periodic layered media predicts a scale dependence and goes to the effective medium velocity [equation (5.1)] in the long wavelength limit (Christensen, 1991).

Figure 5.1 shows the scale-dependent change in measured velocity obtained from experimental observations (Figure 5.1a) and numerical modelling (Figure 5.1b) of band-limited waves propagating in periodic layered media (Marion et al., 1994). In both cases the velocities were determined from picked first-break arrival times. The parameter λ/a is defined here as the ratio of the dominant wavelength of the primary signal to the spatial period of the medium. The observed velocities confirm the theoretical dependence on λ/a, approaching the ray theory and effective medium theory values in the limits. The transition from short to long wavelength behavior occurs in a narrow range of λ/a around 10. In these figures, smooth curves have been drawn through the data points to delineate the trend of the behavior, but these are only empirical.

In the normal incidence one-dimensional case, there is no path effect, since all wave energy must traverse the same layers. Thus the change in velocity from one limit to another is due to the difference in the way the wave "sees" the layers—which in the limits is easily quantified as averaging slowness [equation (5.5)], versus compliance [equations (5.1) and (5.2)]. In this chapter we will refer to this as the "simple scale effect". Marion et al. (1994) discuss more completely the dependence on frequency, contrast of material properties, and volume fraction.

An obvious and important conclusion is that when comparing velocities at different measurement scales—for example sonic logging versus surface seismic—it is not always correct simply to apply the Backus average. The proper method of upscaling varies from case to case and depends on the geologic scale, the wavelength, and the path length.

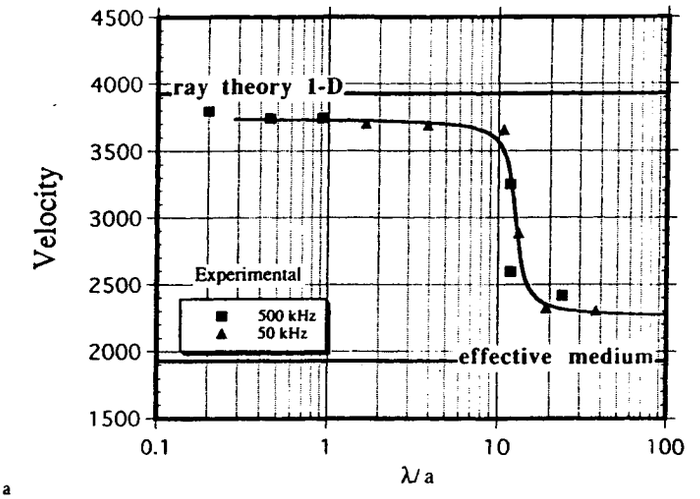

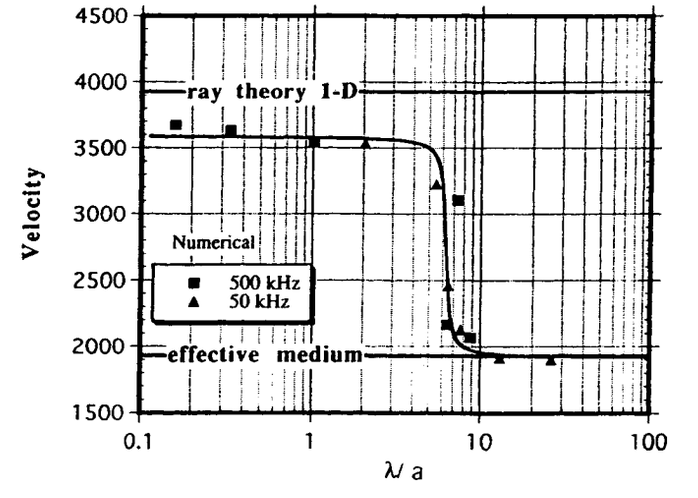

Figure 5.1: (a) Experimental and (b) numerically simulated velocities vs. λ/d for normal incidence propagation through a stratified sample of plastic and steel layers (one-third plastic and two-thirds steel by volume) at the transitions from short to long wavelength behavior. Squares and triangles represent measurements at 500 and 50 kHz, respectively. Smooth empirical curves have been drawn through the data points to highlight the trends (Marion et al., 1994).

5.3 RAY THEORY AND EFFECTIVE MEDIUM BEHAVIOR IN 2 AND 3-DIMENSIONS

Wave propagation problems in deterministic two and three-dimensional heterogeneous media are usually not amenable to exact analytical solutions except in very special cases. Modelling the inhomogeneous medium as a spatial random field allows one to treat whole classes of inhomogeneous media statistically and determine various statistical properties of the wavefield. Wave propagation in random media has been studied both theoretically and numerically by a number of authors, (Keller, 1964; Boyse, 1986; Frankel and Clayton, 1986; Müller et al., 1992; Kneib and Kerner, 1993; Korn, 1993; Shapiro and Kneib, 1993). Typically, the random medium is characterized by a spatially varying slowness field, $n(\mathbf{r}) = n_0 + \epsilon n_1(\mathbf{r})$, where $\mathbf{r}$ is the position vector, $n_1(\mathbf{r})$ is a small fluctuation with zero mean superposed on the background slowness, n_0, and $\epsilon \ll 1$, is a small perturbation parameter. This can represent, for example, grain-to-grain inhomogeneities, lenses of different lithologies or variations in saturation. A small fluctuation model would be less reliable for large contrasts in material properties as between empty pores and mineral grains. The spatial structure of the heterogeneities is described by the spatial autocorrelation function $\langle \epsilon n_1(\mathbf{r_1}) \epsilon n_1(\mathbf{r_2}) \rangle = \epsilon^2 \langle n_1^2 \rangle N(\|\mathbf{r_1} - \mathbf{r_2}\|)$, where
$\langle\ \rangle$ denotes the expectation operator, and $\epsilon^2 \langle n_1^2 \rangle$ is the variance of the slowness fluctuations.

Wavefields in such a stochastic medium are themselves random functions with travel-time and amplitude fluctuations. Statistical moments of these fluctuations can be related to the moments of the slowness fluctuations of the medium, (Ishimaru,1978; Müller et al., 1992; Korn, 1993; Shapiro and Kneib, 1993). Numerical finite-difference calculations indicate that the velocity inferred from the average of picked arrival times for short wavelengths is faster than the velocity inferred from the average slowness of the medium. This effect has been termed "velocity-shift" (Müller et al., 1992; Korn, 1993; Roth et al., 1993), and

has been explained in terms of multiple scattering and preferrential propagation of wave energy along "fast paths" through the medium.

5.3.1 Ray Theory Limit

A little-known formulation that quantifies the velocity shift was developed by Boyse (1986), using an asymptotic ray-theoretical approach. More recently, Roth et al. (1993) used a ray-perturbation method to obtain similar predictions of the velocity shift. We summarize some of Boyse's key results. The criterion for validity of his expressions is that ka is large, where k is the wavenumber and a is the characteristic length of the medium. The wavefield, U, is assumed to be of the form:

$$U(\mathbf{r}) = A(\mathbf{r})e^{ikT(\mathbf{r})}, \tag{5.6}$$

where A and T are the amplitude and phase functions, respectively, and U could describe acoustic, elastic or electromagnetic wavefields. The amplitude and phase are determined by the method of Bergmann (1946) which bypasses ray calculations and gives results in terms of spatial position. This is in contrast to the method utilized by Chernov (1960) and Keller (1964), which first determines the rays and then calculates A and T along the ray, giving results in terms of arc length along the rays. The spatial description of the first method is more suitable for calculating expectations and spatial autocorrelations of the fluctuations.

The traveltime $T(\mathbf{r})$ of the asymptotic wavefield satisfies the eikonal equation:

$$(\nabla T)^2 = n^2. \tag{5.7}$$

Expressing T as a power series in ϵ, $T(\mathbf{r}) = T_0(\mathbf{r})+\epsilon T_1(\mathbf{r})+\epsilon^2 T_2(\mathbf{r})/2+O(\epsilon^3)$, substituting

it into the eikonal equation, and keeping terms up to second order gives:

$$\nabla T_0 \cdot \nabla T_0 = n_0^2, \tag{5.8}$$

$$\nabla T_0 \cdot \nabla T_1 = n_0 n_1, \tag{5.9}$$

$$\nabla T_0 \cdot \nabla T_2 = n_1^2 - (\nabla T_1)^2. \tag{5.10}$$

For waves in an isotropic medium that are initially plane and propagating along the x-direction such that $T(x = 0, y, z) = 0$, the solutions are (Boyse, 1986):

$$T_0(\mathbf{r}) = n_0 x, \tag{5.11}$$

$$T_1(\mathbf{r}) = \int_0^x n_1(\xi, y, z) d\xi, \tag{5.12}$$

$$T_2(\mathbf{r}) = -n_0^{-1} \int_0^x \int_0^\xi \int_0^\xi \nabla_\perp n_1(\zeta_1, y, z) \cdot \nabla_\perp n_1(\zeta_2, y, z) d\zeta_1 d\zeta_2 d\xi, \tag{5.13}$$

where $\nabla_\perp$ is the gradient transverse to the x direction. The expected traveltime (spatial average) at a distance x is then given as (Boyse, 1986):

$$\langle T \rangle = n_0 \left[x + \alpha \epsilon^2 \frac{\langle n_1^2 \rangle}{n_0^2} \int_0^x (x - \xi)^2 \frac{N'(\xi)}{\xi} d\xi \right] + O(\epsilon^3), \tag{5.14}$$

where $\alpha = 1, (1/2), 0$ for three, two, and one dimension, respectively, and the prime denotes differentiation. We obtained the expressions for one and two dimensions by taking limiting

cases of the 3-D Boyse theory. When the wave has travelled a large distance compared to the correlation length of the medium, ($x \gg a$), and when the correlation function is such that $N(\xi) \ll N(0)$ for $\xi > a$, the above expression simplifies to (Boyse, 1986):

$$\langle T \rangle \sim n_0[x - \alpha x^2 \sigma_n^2 D], \tag{5.15}$$

where D is defined to be:

$$D \equiv -\int_0^\infty \frac{N'(\xi)}{\xi} d\xi > 0, \tag{5.16}$$

and

$$\sigma_n = \frac{\epsilon\sqrt{\langle n_1^2 \rangle}}{n_0} \tag{5.17}$$

is the coefficient of variation or the normalised standard deviation of the slowness fluctuations. Thus the expected traveltime for the wave in the random medium is less than or equal to the traveltime in the expected (mean) medium. The slowness calculated from the average ray theory traveltime is given by $n_{rt} = \langle T \rangle / x$. Scaling the distance by the correlation length a in the definition of D, we can derive:

$$\frac{n_{rt}}{n_0} = 1 - \alpha\sigma_n^2(\frac{x}{a})\overline{D}, \tag{5.18}$$

where $\overline{D}$ is defined similarly to D, [equation (5.16)], but with the autocorrelation function of unit correlation length. For a Gaussian correlation function $\overline{D} = \sqrt{\pi}$. This brings out the dependence of n_{rt} on the variance of the slowness fluctuations and the path length. For one dimension ($\alpha = 0$) we get the result obtained in our discussion of stratified media that

in the ray theory limit the traveltime is the distance times the average slowness. In two and three dimensions the path effect appears, described by the term $(\alpha\sigma_n^2(x/a)\overline{D})$ in equation (5.18). In this case, rays diffract around slower heterogeneities, preferentially seeking the faster material, resulting in wave arrivals that are on average faster in the random medium than in a uniform medium having the same mean slowness. Furthermore, the expected traveltime in three dimensions is less than that in two dimensions, which in turn is less than that in one dimension. This is because in higher spatial dimensions more admissible paths are available to minimize the traveltime. Roth et al. (1993) have obtained a similar result using a different approach of ray perturbation and ensemble averaging. This seems to explain the observed velocity shift in the numerical calculations of Müller et al. (1992) and is also consistent with our own computations which we present in the next section. We will see that for the same slowness fluctuations, the path effect in two and three dimensions can give velocity dispersion an order of magnitude greater than the simple scale effect that we observed in one dimension.

Müller et al. (1992) have established ray-theoretical results relating the autocorrelation function of the slowness fluctuations, $N(\mathbf{r})$, to the autocorrelation function of the traveltime fluctuations around the mean traveltime. Using first order straight-ray theory they show that:

$$\phi(\zeta) = 2X \int_{\zeta}^{\infty} N(\xi) \frac{\xi}{\sqrt{\xi^2 - \zeta^2}} d\xi, \tag{5.19}$$

where $\phi(\zeta)$ is the autocorrelation function of the traveltime fluctuations observed in the plane $x = X$. Here ζ is the lag vector transverse to the x-direction. Thus for a random medium with Gaussian autocorrelation function, $N(r) = e^{-r^2/a^2}$, the variance of the traveltime fluctuations, $\phi(0)$, can be related to the variance of the slowness fluctuations as (Müller et al., 1992):

$$\phi(0) = \sqrt{\pi} X a \epsilon^2 \langle n_1^2 \rangle. \tag{5.20}$$

An important point is that the expected traveltime of the wavefield in the random medium is distinct from the traveltime of the expected wavefield in the random medium. As discussed above, the expected traveltime of the wavefield in the random medium is less than the traveltime of the wavefield in the average medium. In contrast, it was shown by Keller (1964) and also by Boyse (1986) that the traveltime (or equivalently, phase) of the expected wave is larger than the traveltime of the wave in the average medium. The expected wave, which is an ensemble average of the wavefield over all possible realizations of the random medium, travels slower than the wavefield in the average medium. Thus:

$$\langle T(U(n)) \rangle \leq T(U(\langle n \rangle)) \leq T(\langle U(n) \rangle). \tag{5.21}$$

While ergodicity arguments are often used to equate ensemble averages with spatial averages, the ensemble averaged wavefield may not be an appropriate description of the wavefield in any one particular realization and may in fact be unrealizable (Stanke and Burridge, 1993). Therefore care must be taken when comparing predictions of ensemble averages with data which themselves are not ensemble averages but come from a particular realization.

5.3.2 Effective Medium Limit

We now consider the effective medium or long wavelength limit, when the seismic wavelength is much larger than the characteristic length of the inhomogeneities. In this case the heterogeneous medium can be modelled as a homogeneous (possibly anisotropic) medium

with an effective elastic modulus and seismic velocity. There exists a large body of literature on long-wavelength or quasi-static theories for estimating effective moduli, and bounds on effective moduli of heterogeneous mixtures (see e.g. Watt et al., 1976; Berryman, 1980, 1993b; Wang and Nur, 1992 and references therein). The simplest upper and lower bounds on effective moduli of elastic media are given by the Voigt and Reuss averages, respectively. The Voigt velocity, V_{voigt}, is given by $V_{voigt} = \sqrt{M_{voigt}/\rho_{ave}}$, where ρ_{ave} is the volume average density and M_{voigt} is the volume average of the moduli M_i of the constituents: $M_{voigt} = \sum f_i M_i$ with f_i being the volume fractions of the constituents. The lower bound, the Reuss velocity, is given by $V_{reuss} = \sqrt{M_{reuss}/\rho_{ave}}$. M_{reuss} is obtained from the volume average of the compliances, or equivalently, the harmonic mean of the moduli: $1/M_{reuss} = \sum(f_i/M_i)$. It can be shown that (Berryman, 1993a):

$$V_{reuss} \leq \langle \frac{1}{V} \rangle^{-1} \leq \langle V \rangle \leq V_{voigt}. \tag{5.22}$$

While tighter bounds on the effective moduli of heterogeneous elastic media certainly exist (Watt et al., 1976; Berryman, 1993b), the differences among the various methods are quite small for media with small fluctuations and are often of much less importance than the speed-up at short wavelengths due to the path effect. Hill (1963) showed that when all the constituents in an isotropic composite have the same shear modulus (as in an acoustic medium where shear modulus is zero), the effective compressional-wave compliance β_{emt} is given exactly by the volume average of the compliances β_i of each constituent, $\beta_{emt} = \sum f_i \beta_i$. This is equivalent to Wood's (1955) formula for immiscible fluid mixtures and to the Reuss bound for elastic media. Then the long wavelength effective medium slowness for acoustic propagation is:

$$n_{emt} = (\rho_{ave}\beta_{emt})^{1/2}. \tag{5.23}$$

Note that while this is an upper bound on slowness for general heterogeneous elastic materials, it is an exact expression for acoustic media. This effective medium slowness is always larger than the mean slowness (Berryman, 1993a), which in turn is larger than the slowness obtained from the mean traveltime in the ray theory limit, equation (5.14). For small density fluctuations with zero mean, $\rho = \rho_{ave} + \rho_1$, it is easy to show that up to second order, n_{emt}/n_0 is given by:

$$\frac{n_{emt}}{n_0} \approx 1 + \frac{\sigma_n^2 + \sigma_\rho^2}{2} - \frac{\langle n_1 \rho_1 \rangle}{n_0 \rho_{ave}}, \tag{5.24}$$

where σ_ρ is the normalized standard deviation of the density fluctuations. If the density fluctuations are correlated with the slowness fluctuations such that $\rho_1/\rho_{ave} = \gamma n_1/n_0$ where γ is a constant, then:

$$\frac{n_{emt}}{n_0} \approx 1 + \frac{(1-\gamma)^2}{2}\sigma_n^2, \tag{5.25}$$

which for a medium with constant density, ($\gamma = 0$), reduces to $n_{emt}/n_0 \approx 1 + \sigma_n^2/2$. Using equations (5.18) and (5.25) we can get an estimate of the total velocity dispersion due to scale and path effects:

$$\frac{n_{emt} - n_{rt}}{n_0} \equiv \frac{\Delta n}{n_0} \approx \sigma_n^2 \left[\frac{(1-\gamma)^2}{2} + \alpha(\frac{x}{a})\overline{D} \right]. \tag{5.26}$$

Thus for a constant-density medium with a Gaussian spatial autocorrelation function of

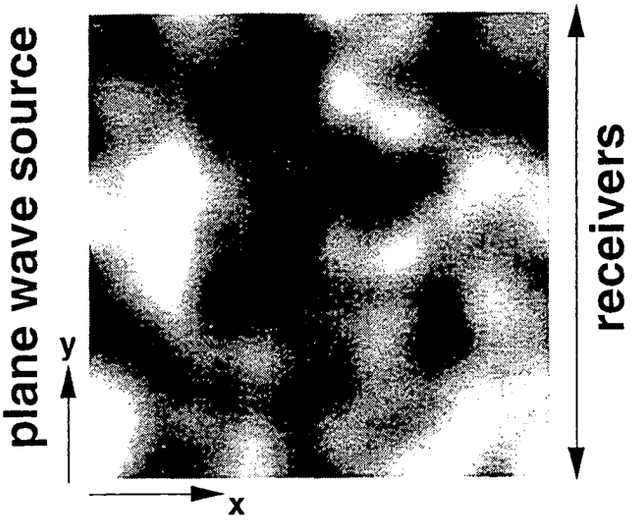

Figure 5.2: Two-dimensional synthetic random velocity model with variance of velocity fluctuations of three percent, and a Gaussian spatial autocorrelation function.

the slowness fluctuations we get $\Delta n/n_0 \approx \sigma_n^2[0.5 + \alpha(x/a)\sqrt{\pi}]$. Again, equation (5.26) is exact for acoustic media, while for elastic media it represents the difference between the ray theory slowness and the upper bound of the effective medium slowness.

5.4 NUMERICAL MODELLING

We now present some of the results of numerical simulations in which we explore the measurable velocity as a function of λ/a. Two-dimensional synthetic random media with Gaussian autocorrelation $N(r) = e^{-r^2/a^2}$ were generated with a standard deviation of 3 percent in the slowness fluctuations. Figure 5.2 shows one realization of the random medium. Waves that were initially plane were propagated across a 2048 by 2048 node grid using an

acoustic finite-difference scheme, (Claerbout, 1985), with zero-slope side boundary conditions and free-surface conditions at the top and bottom. The dominant wavelength of the input wavelet was varied over a range of λ/a ratios from 0.3 to about 20. The length of the medium was taken to be more than 10 times the correlation length (i.e. 200 grid points per correlation length). In a laboratory setting this might correspond to a rock sample of 5 cm length with heterogeneities at the scale of 0.5 cm, while in a cross-well experiment this might represent a well-to-well distance of 500 m with inhomogeneities of the order of 50 m. First arrival times were picked from the synthetic seismograms recorded after the wave had propagated through the random medium. An amplitude picking criterion was chosen at 0.1 percent of the first peak amplitude. Figure 5.3 shows the synthetic seismograms computed at the far edge of the grid for $\lambda/a = 0.3$, (Figure 5.3a), and $\lambda/a = 9.7$, (Figure 5.3b), along with the picked arrival times. (The scale along the x-axis is not the same for Figure 5.3a and Figure 5.3b.) As expected, the short wavelength ($\lambda/a = 0.3$) wavefield shows more scattering effects and development of coda compared to the long wavelength one which is much more uniform.

Figure 5.4 shows the velocities calculated from the arrival times for each trace versus spatial position transverse to the direction of propagation, for the same two values of λ/a . We also show the velocities calculated from the average of the picked traveltimes (which is not the same as the average velocity) in each case and the theoretical predictions for: (1) the acoustic effective medium theory limit, determined from the average compliance [equation (5.23)]; (2) the one-dimensional ray theory limit determined from the average slowness [equation (5.14) with $\alpha = 0$]; (3) the Voigt upper bound calculated from the average moduli; and (4) the two-dimensional ray theory limit, determined from equation (5.14) with $\alpha = 1/2$. The variations in traveltimes, and velocities inferred from traveltimes, persist at $\lambda/a \sim 10$ indicating that even longer wavelengths are required before the heterogeneous medium can be replaced by a homogeneous effective medium. One dimesional studies of Kerner (1992) and Rio et al. (1995) suggest that for Gaussian media, fluctuations can persist up to

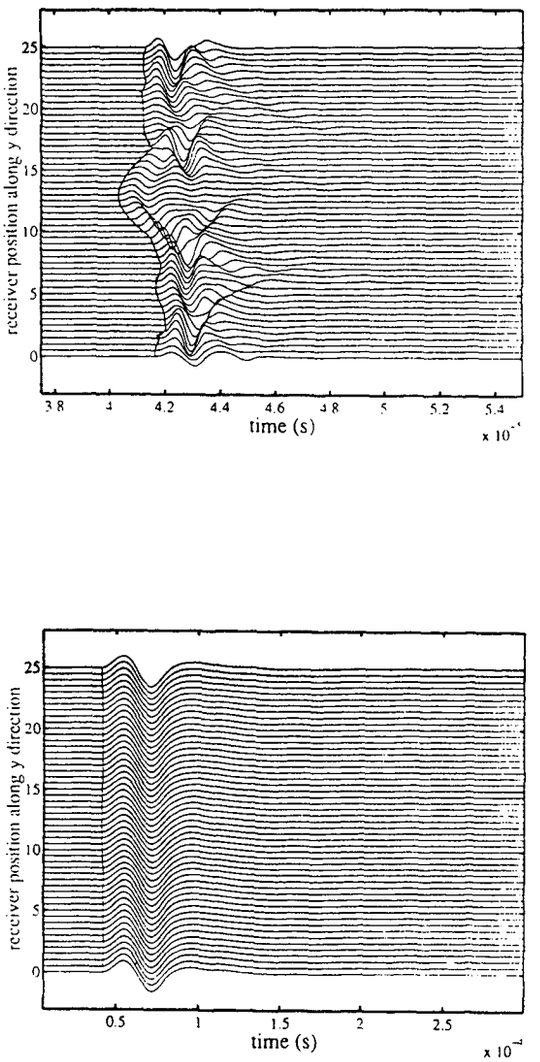

Figure 5.3: Synthetic seismograms computed along the edge of the synthetic medium for (a) $\lambda/a = 0.3$ and (b) $\lambda/a = 9.7$. Picked arrival times are marked.

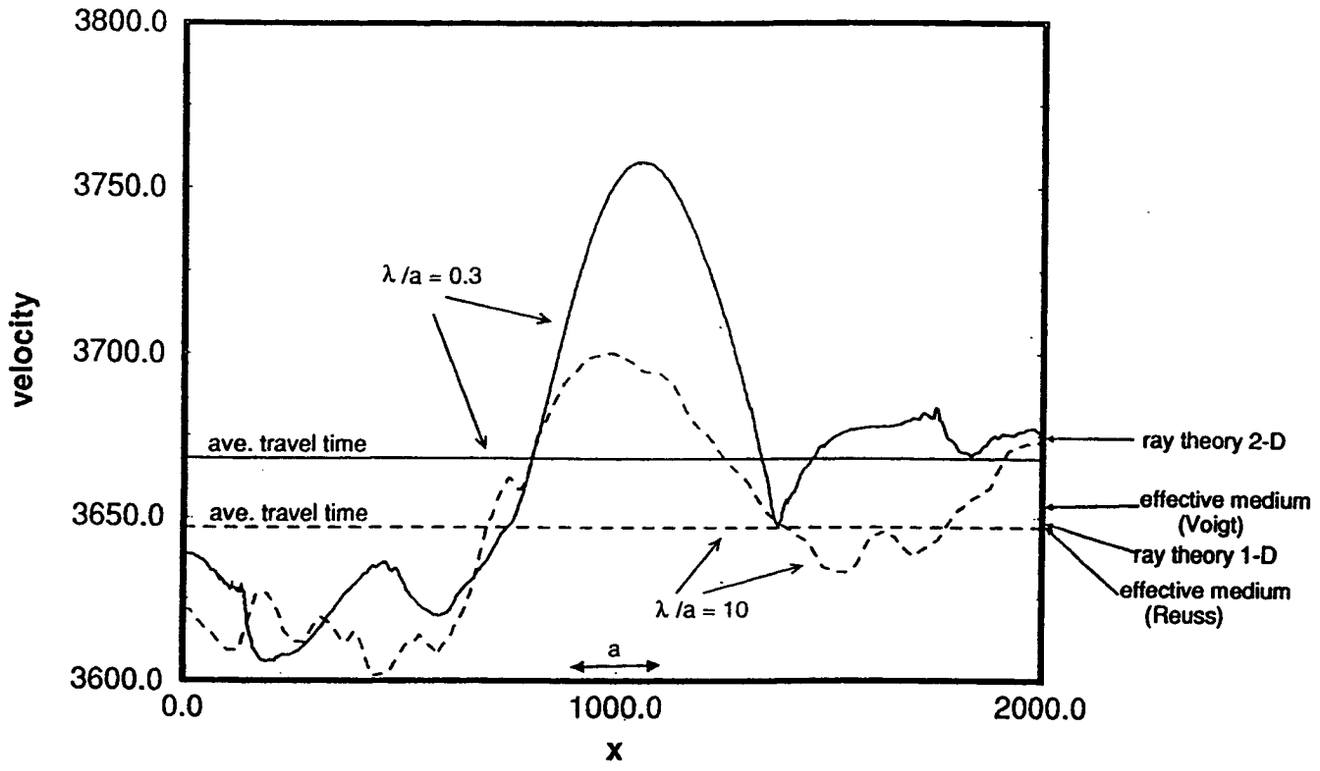

Figure 5.4: Velocities computed from arrival times picked from the traces in Figure 5.3. Horizontal lines indicate the velocities inferred from the average arrival times for each case. Theoretical predictions for 2-D ray theory, effective medium theory (Voigt average), 1-D ray theory (average slowness), and effective medium theory (Reuss average) are marked at the right.

wavelengths that are 100 or even 1000 times the correlation length. The velocities for $\lambda/a \sim 10$ are not everywhere bounded by the Voigt and Reuss bounds, because the wavelengths are not long enough for the effective medium bounds to be applicable. However, the velocity inferred from the average traveltime is close to the effective medium prediction. The shift of average traveltimes from effective medium to ray theory values is clearly evident in the numerical runs. Note that the predicted speed-up from long wavelength to short wavelength velocity is an order of magnitude larger in two dimensions than in one dimension. As explained earlier, this is due to the fast path effect in two dimensions.

An important issue with estimating velocities in heterogeneous media is the receiver array geometry and resolution. In the numerical simulations discussed above, our receiver spacing (spacing between adjacent traces) was always much finer than the correlation length, a, and the spread of receivers (total width of record sections) in the direction transverse to the direction of propagation was much larger than a. Therefore we could estimate fairly well the mean arrival time. This might represent the case in surface seismic, crosswell seismic, or VSP, when the receiver spacing is less than the typical heterogeneity size, and the cable is longer. In the laboratory, ultrasonic measurements are made with a single finite size receiving transducer that is usually larger than the scale of the heterogeneity. If we assume that the transducer is linear, then the recorded signal is approximately the sum of the many individual traces we would have recorded if we could replace the transducer with an array of tiny receivers. Then we pick the arrival time of the mean trace rather than the mean of the individual times. The result is an apparent arrival that is even earlier, because we are picking the earliest of the traces, rather than the mean. We estimate the effect as follows. We consider the mean trace, $S(t)$, to be the sum of the individual traces, $s_i(t)$:

$$S(t) = \sum_i s_i(t) \tag{5.27}$$

Now, if we assume that the $s_i(t)$ are approximately the same except for spatially varying time shifts, as we see in Figure 5.3a, then we can write this as:

$$\begin{aligned} S(t) &\approx \sum_i \delta(t-\tau_i) * s(t) \\ &\approx s(t) * \sum_i \delta(t-\tau_i) \\ &\approx s(t) * F(t), \end{aligned} \tag{5.28}$$

where $\delta(t-\tau)$ is a delta function, which when convolved with $s(t)$ is a time shift operator. The sum over delta functions, F, is essentially the probability distribution function of the delay times. The width or variance of F is given by equation (5.20). In the ray theory limit we assume that the wavelength of $s(t)$ is very small, so that picking the first-break of the mean trace is essentially determined by the variance of F. If, for example, $F(t)$ is Gaussian with variance, σ, then picking with an amplitude criterion of 2 percent would be roughly equivalent to 3σ. There the pick of the mean trace would be 3σ earlier than the mean of the picked traces.

For our numerical simulations the standard deviation, σ_T, of the traveltime fluctuations for the short wavelength case ($\lambda/a = 0.3$) is 1.14 percent, which is close to the theoretically predicted value of 1.26 percent from equation (5.20). It was observed empirically that the earliest traveltimes are approximately two standard deviations earlier than the mean traveltime, i.e. $\langle T \rangle(1 - 2\sigma_T)$. The velocities inferred from the traveltime fluctuations fall within one standard deviation of the velocity fluctuations present in the material. The fastest velocity is approximately $V_{mean}(1 + \sigma_V)$ where V_{mean} and σ_V are the mean and normalized standard deviation of the velocity fluctuations in the random medium.

Figure 5.5 shows velocities obtained from the average picked traveltimes as a function of λ/a for three different realizations of the random medium. The transition from

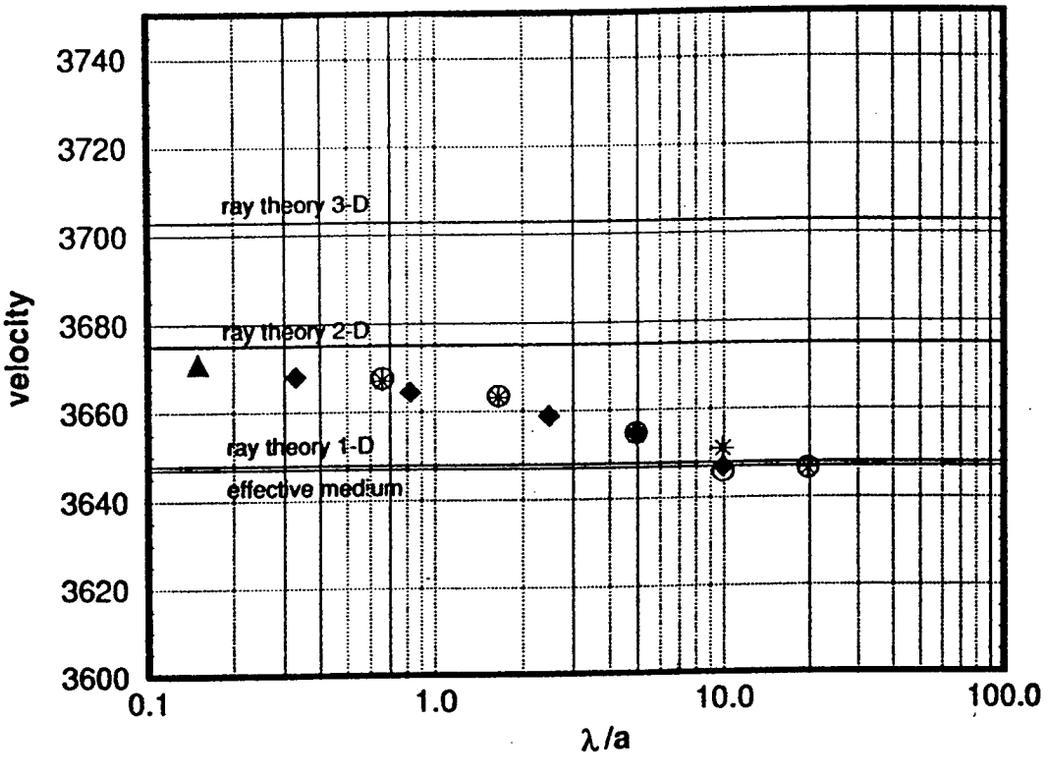

Figure 5.5: Velocities computed from the average arrival times of the finite difference simulations, versus λ/a at the transition from short to long wavelengths. The different symbols indicate three different realizations of the random medium. The result from the eikonal solver is shown by the triangle.

short to long wavelength velocities is clear, and the computed values in the limits agree reasonably well with the theoretical predictions. We see again that the predicted path dependent velocity dispersion in two and three dimensions is much larger than the simple scale effect in one dimension. To verify the results from the finite difference computations at the shortest wavelengths, we also computed the traveltimes for an initially plane wave propagating through one of the realizations of the random medium using a finite-difference eikonal solver (Zhang, 1993). The results matched very well with the picked traveltimes for the short wavelength synthetic seismograms as shown in Figure 5.6. The velocity obtained from the mean of the traveltimes calculated by the eikonal solver is also shown in Figure 5.5 and is in close agreement with the two-dimensional ray theoretical prediction using equation (5.14) with $\alpha = 1/2$. For the eikonal equation, $\lambda/a = 0$. Since the graph is on a semilogarithmic scale, we have plotted the results from the eikonal solver at a suitable, though arbitrary, small λ/a. The transition from short to long wavelength behavior occurs over a range of λ/a values from $\lambda/a = 1.0$ to $\lambda/a = 10$ and is more gradual than that observed in the periodic one-dimensional studies (Figure 5.1) of Marion et al. (1994).

5.5 EXPERIMENTAL OBSERVATIONS

In laboratory measurements on saturated rocks velocity dispersion arises from poroelastic and viscoelastic mechanisms, in addition to the scale-dependent geometric dispersion discussed above. The non-geometric mechanisms are generally associated with soft, crack-like porosity as evidenced from the tremendous decrease of attenuation and dispersion that is usually observed with increasing confining pressure. In fact, at low confining pressures viscoelastic effects often dominate dispersion in laboratory samples. However, at high confining pressure, residual velocity dispersion is sometimes observed which is thought to arise from other mechanisms such as the scale effects analyzed in the previous sections.

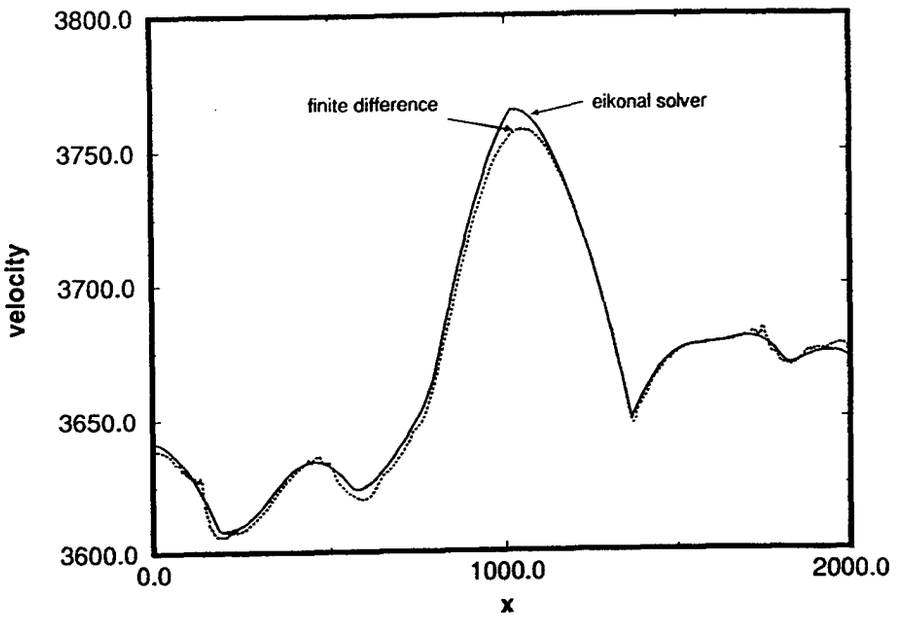

Figure 5.6: Velocities inferred from arrival times picked from traces from the numerical simulation through the synthetic medium, comparing the finite difference simulation at $\lambda/a = 0.3$ and the eikonal solver.

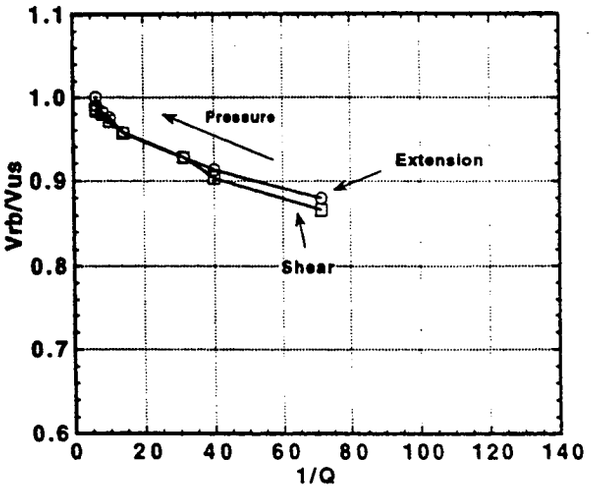

(a)

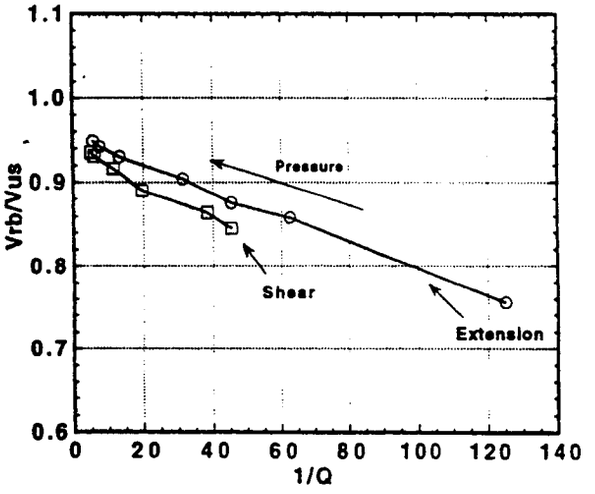

(b)

Figure 5.7: Velocity dispersion (resonant bar velocity over ultrasonic velocity) versus attenuation measured by Lucet (1989) for (a) sandstone and (b) limestone samples.

One of the few extensive studies of velocity dispersion made on the same rocks at widely different frequencies was by Lucet (1989). She measured velocity and attenuation at ultrasonic frequency (0.5 MHz), using the pulse transmission technique, and in the sonic range (2-10 kHz), using the resonant bar technique. Figure 5.7 shows her velocity dispersion vs. resonant bar attenuation for sandstone and limestone samples with porosities of 15 percent and 12 percent, respectively. The vertical axis shows the ratio of low frequency (resonant bar) to high frequency (ultrasonic) velocities, (V_{rb}/V_{us}), and the horizontal axis is attenuation measured at sonic frequency. Departure of V_{rb}/V_{us} from unity is a measure of the velocity dispersion. The direction of increasing confining pressure is shown by the arrow. As expected, both dispersion and attenuation decrease with increasing confining pressure. In fact, for viscoelastic mechanisms in medium to low porosity rocks we generally expect the curve to trend to an intercept of $V_{rb}/V_{us} \rightarrow 1$ as $Q^{-1} \rightarrow 0$. This is the case for the sandstone (Figure 5.7a) and for most of the rocks in the Lucet study. However for the limestone (Figure 5.7b) the intercept is $V_{rb}/V_{us} \approx 0.94$, indicating residual velocity dispersion that is apparently not due to viscous fluid effects.

Lucet (1989) qualitatively interpreted the residual dispersion to be the result of scale effects associated with heterogeneities in the samples. X-ray sections showed that in the sandstone the characteristic scale of the heterogeneities (essentially the grain size) was less than the ultrasonic wavelength, i.e. the measurements were in the effective medium range for both resonant bar and ultrasonic frequencies. For the limestone, however, (Figure 5.8) the ultrasonic wavelength was comparable to the characteristic scale of the heterogeneities (in this case clusters of grains). That is, for the limestone the ultrasonic measurements were in the short wavelength range while resonant bar measurements were in the long wavelength range.

To explore this interpretation we made numerical finite-difference simulations of wave propagation through two-dimensional heterogeneous media constructed from the X-ray image of the limestone in Figure 5.8. We simply assumed for this exercise that the velocity

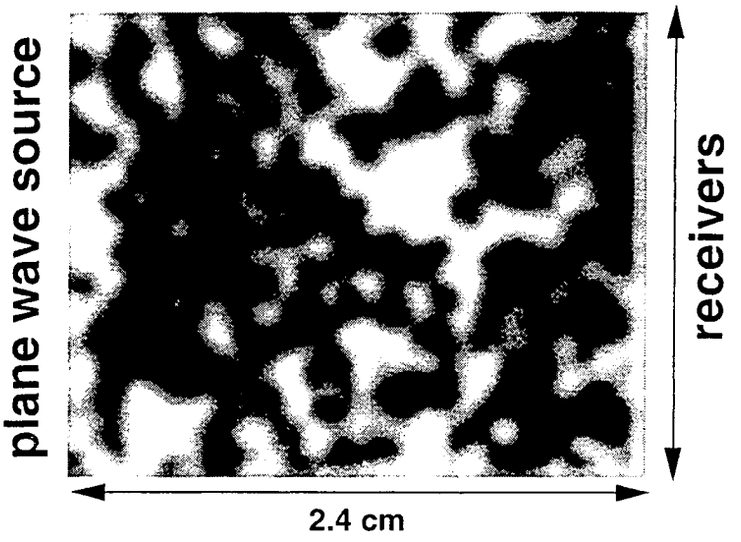

Figure 5.8: X-ray image (Lucet, 1989) of density in a small two-dimensional slice of the limestone in Figure 5.7b. This was assumed to be proportional to velocity for numerical simulations of wave propagation.

fluctuations are proportional to the observed density fluctuations. The mean slowness was taken to be $1/(4955m/s)$ (Lucet, 1989), and the standard deviation of the fluctuations was assumed to be 4 percent, since this gave results consistent with the observed residual dispersion at high pressure. The medium was discretized onto a rectangular grid of 634 by 506 points corresponding to the X-ray image dimensions of 2.4 cm by 1.9 cm.

The correlation length, a, is on the order of a few millimeters, but is difficult to define precisely. On the X-ray image, (Figure 5.8), the typical size of the light (high density) and dark (low density) patches is about 5 mm. The closest fitting Gaussian to the numerically computed autocorrelation function of the image gives an a of about 1 mm while the first zero-crossing of the autocorrelation gives $a \sim 2.5$ mm. This is the scale of the individual grains. In our theoretical modelling we took a to be 3 mm because it lies in the middle of this range, and it gives a reasonable agreement with the results of the numerical simulations.

We suspect this is appropriate within a factor of 2.

The dominant frequency of the input wavelet was varied to span a range of λ/a ratios from $\lambda/a \approx 20$ to $\lambda/a \approx 0.08$. As with the other simulations, an initially plane, band-limited wavelet was propagated, and seismograms were calculated at the far edge of the medium. The finite difference simulations show the same pattern of average traveltime decrease with decreasing wavelength that we observed with the synthetic velocity models. The procedure was the same as before: compute seismograms at each point along the far edge of the model; pick first-break times of each trace; average the pick times to get the mean arrival time.

The velocities derived from the computed average arrival times are plotted versus λ/a in Figure 5.9. The result from the eikonal solver is shown by the square symbol. There is about 1 percent velocity speedup with decreasing λ/a, from 4959 m/s at $\lambda/a > 1$ to 4994 m/sec at $\lambda/a \ll 1$. The short wavelength average velocity is also faster than the mean velocity of the medium, as expected.

Since we do not know the actual point values of material velocity within the limestone sample, the functional form of the autocorrelation of the slowness fluctuations, or the precise a, we cannot predict the measured velocities in detail. Nevertheless, if we assume a Gaussian autocorrelation function, and $a \approx$ 3mm we can use equation (5.26) to predict a plausible two-dimensional dispersion that is in good agreement with the simulation (see Figure 5.9). Furthermore we can use the velocity shift observed in our two dimensional simulations to estimate the expected velocity shift in three dimensional laboratory samples. Using the actual laboratory sample length of 5 cm and material slowness fluctuations with a 4 percent standard deviation, (as used in our numerical simulations), we estimate a velocity shift of the order of 5 percent [equation (26) with $\gamma = 0$]. This is consistent with the actual laboratory observations (Figure 5.7b). The three dimensional velocity shift is shown by the ray theory 3-D line plotted in Figure 5.9.

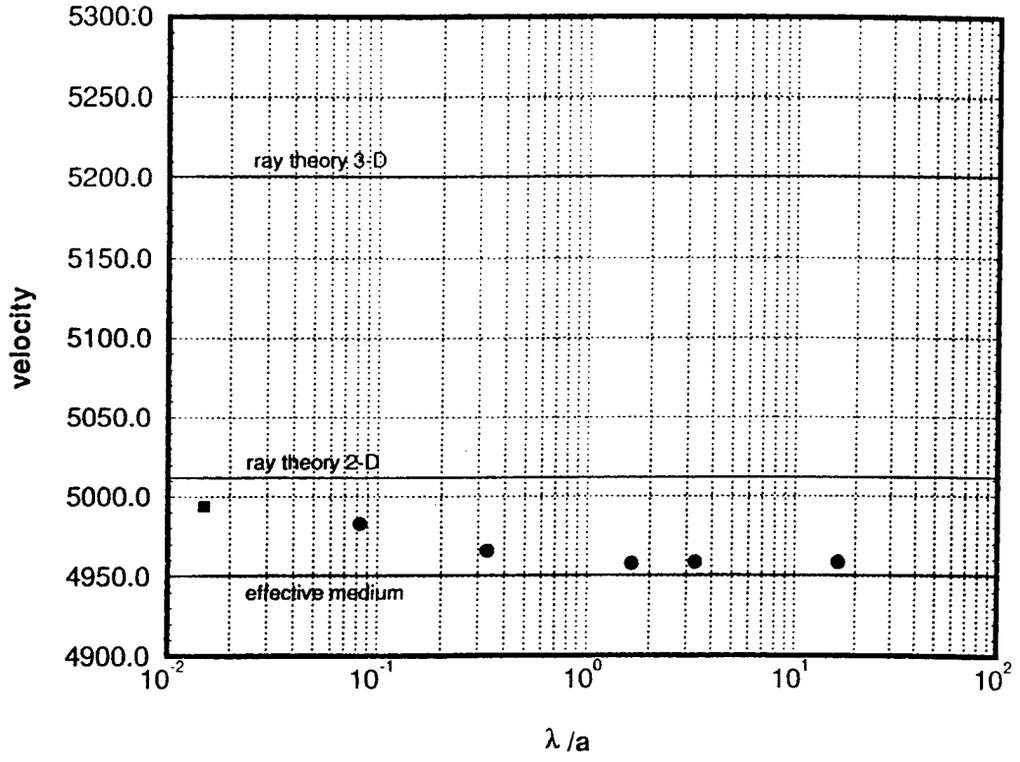

Figure 5.9: Velocities computed from the average arrival times of the finite difference simulations through the medium shown in Figure 5.8, versus λ/a at the transition from short to long wavelengths. The square shows the velocity calculated from the average traveltime given by the eikonal solver. Also shown are theoretical predictions of effective medium velocity (Reuss) and two-dimensional and three dimensional velocities computed assuming $a = 3mm$ and a material velocity fluctuation of 4 percent.

This exercise, though not a proof, demonstrates the plausibility of scale effects producing the laboratory-observed velocity dispersion. One of the remaining research issues is how to define the appropriate scale in various media. In the limestone sample there may in fact be two important scales: the grain scale ($\sim 1 - 2$mm) and the cluster scale ($\sim$ 5mm). This could account for the observed transition value of $\lambda/a \approx 0.1$ in Figure 5.9, which is smaller than the synthetic case in Figure 5.5.

5.6 SUMMARY

Heterogeneities affect seismic wave propagation in ways that both complicate and aid in the interpretation of seismic images. In general, measurable traveltimes decrease with decreasing values of the ratio of seismic wavelength to correlation length of the medium, λ/a. The simplest example is normal incidence wave propagation in stratified media, where in the long wavelength limit the effective average velocity is determined by the average of the elastic compliances (the Backus average), while in the short wavelength limit the effective average velocity is determined by the average of the slownesses. Laboratory, experimental, and theoretical results all confirm the variation, and lead to several conclusions:

(1) Velocities in stratified media, measured at the core scale in the laboratory ($\lambda \sim 1$ cm), in well logs ($\lambda \sim 10 - 100$ cm), and surface seismic methods ($\lambda \sim 10$ m), may be different simply because of the scale of the measurements. The amount of the difference, and the values of λ/a where the transition occurs depend on the individual rock properties and their spatial distributions and scales.

(2) It is not always correct simply to use the Backus average to upscale velocities in stratified geology from lab to logs, and from logs to surface seismic. Depending on the scales of the measurements and the geology it is sometimes correct to use ray theory, sometimes the Backus average, and sometimes both.

In two and three dimensions there is also the path effect, which amplifies the velocity increase with decreasing wavelength. As the seismic wavelength decreases the waves tend to find the faster material, giving generally earlier arrivals, and faster inferred velocities. In fact, in the short wavelength limit the velocity inferred from the mean traveltimes is faster than the mean velocity of the medium. We investigated the scale dependence of measurable seismic velocities using finite-difference simulations of acoustic wave propagation in two-dimensional random media. We have shown that the ray theoretical results of Boyse (1986) can be used to predict the observed velocity shift in one, two, and three dimensions. Our two dimensional simulations agree reasonably well with the theoretical predictions for two-dimensional media while the predictions for three dimensions are consistent with observations in three-dimensional laboratory samples. The velocity depends on the variance of the fluctuations of the medium, its spatial autocorrelation, the seismic wavelength, and the path length [equation (5.18)]. The predicted velocity in three dimensions is faster than in two dimensions, which is, in turn, faster than in one dimension.

The numerical simulations also confirm the spatial fluctuations in traveltime, which can be modeled fairly well in the short wavelength limit using the theory of Müller et al.(1992). The fluctuations have practical implications for recording data and measuring velocities. When the receiver spacing is small enough and the array length is long enough to characterize the fluctuations, then the mean of the traveltimes will yield the fast ray theory velocities predicted by Boyse (1986). Furthermore, the variance of the fluctuations yields information on the slowness variance of the medium. The correlation length of the traveltime fluctuations is a measure of the spatial correlation length of the medium. When arrival times are picked from the stacked trace, or equivalently the output trace of a large seismic group array or from a large laboratory transducer, then the first-break will tend to be even earlier than the mean traveltime.

The scale-dependence of seismic wave propagation impacts reservoir characterization

in many ways. When interpreting images of seismic velocity or impedance in terms of reservoir properties, it is important to recognize that the seismic-to-rock properties transforms derived from the lab or from well logs might require corrections to the surface seismic scale.

ACKNOWLEDGEMENTS

We thank Prof. J. Keller for helpful discussions and for bringing to our notice the work by W. Boyse. We also thank Luis Canales and Greg Beroza for useful discussions and Le-Wei Mo and Jerry Harris for providing L. Zhang's eikonal solver. We acknowledge the many useful comments of the reviewers. This research was funded by the Stanford Rock Physics and Borehole Geophysics Project and Gas Research Institute contract 5093-260-2703. D. Mujica was supported by INTEVEP S. A.

REFERENCES

Backus, G. E., 1962, Long-wave elastic anisotropy produced by horizontal layering: J. Geophys. Res., **67**, 4427-4440.

Bergmann, P. G., 1946, Propagation of radiation in a medium with random inhomogeneities: Phys. Rev., **70**, 486-491.

Berryman, J. G., 1979, Long-wave elastic anisotropy in transversely isotropic media: Geophysics, **44**, 896-917.

Berryman, J. G., 1980, Long-wavelength propagation in composite elastic media II. Ellipsoidal inclusions: J. Acoust. Soc. Am., **68**, 1820-1831.

Berryman, J. G., 1993a, Analysis of ultrasonic velocities in hydrocarbon mixtures: J. Acoust. Soc. Am., **93**, 2666-2668.

Berryman, J. G., 1993b, Mixture theories for rock properties, *in* Ahrens, T. J., ed., AGU Handbook of Physical Constants.

Boyse, W. E., 1986, Wave propagation and inversion in slightly inhomogeneous media: Ph.D. dissertation, Stanford University.

Carcione, J. M., Kosloff, D., and Behle, A., 1991, Long-wave anisotropy in stratified media: Geophysics, **56**, 245-254.

Chernov, L. A., 1960, Wave propagation in random media: McGraw-Hill, New York.

Christensen, R. M., 1975, Wave propagation in layered elastic media: J. Appl. Mech., **42**, 153-158.

Christensen, R. M., 1991, Mechanics of composite materials: Robert E. Krieger Publ. Co., Florida.

Claerbout, J. F., 1985, Imaging the Earth's interior: Blackwell Scientific Publ.

Frankel, A., and Clayton, R. W., 1986, Finite difference simulations of seismic scattering: Implications for the propagation of short-period seismic waves in the crust and models of crustal heterogeneity: J. Geophys. Res., **91**, 6465-6489.

Helbig, K., 1984, Anisotropy and dispersion in periodically layered media: Geophysics, **49**, 364-373.

Hill, R., 1963, Elastic properties of reinforced solids: some theoretical principles: J. Mech. Phys. Solids, **11**, 357-372

Ikelle, L. T., Yung, S. K., and Daube, F., 1993, 2-D random media with ellipsoidal autocorrelation functions: Geophysics, **58**, 1359-1372.

Ishimaru, A., 1978, Wave propagation and scattering in random media, vol. 2: Academic Press, New York.

Jannaud, L. R., Adler, P. M., and Jacquin, C. G., 1991, Spectral analysis and inversion of codas: J. Geophys. Res., **96**, 18215-18231.

Keller, J. B., 1964, Stochastic equations and wave propagation in random media: Proc. Symp. Appl. Math., **16**, 145-170.

Kerner, C., 1992, Anisotropy in sedimentary rocks modeled as random media: Geophysics, **57**, 564-576.

Kneib, G., and Kerner, C., 1993, Accurate and efficient modeling in random media: Geophysics, **58**, 576-588.

Korn, M., 1993, Seismic waves in random media: J. Appl. Geophys., **29**, 247-269.

Lucet, N. M., 1989, Vitesse et atténuation des ondes élastiques soniques et ultrasoniques dans les roches sous pression de confinement: Thèse de Doctorat de l'Université Paris.

Marion, D., Mukerji, T., and Mavko, G., 1994, Scale effects on velocity dispersion: from ray to effective medium theories in stratified media: Geophysics, **59**, 1613-1619.

Marion, D., and Coudin, P., 1992, From ray to effective medium theories in stratified media : An experimental study: 62nd Ann. Intl. Mtg. SEG expanded abstracts, 1341-1343.

Melia, P. J., and Carlson, R. L., 1984, An experimental test of P-wave anisotropy in stratified media: Geophysics, **49**, 374-378.

Müller, G., Roth, M., and Korn, M., 1992, Seismic-wave traveltimes in random media: Geophys. J. Int., **110**, 29-41.

Nolet, G., 1987, Seismic wave propagation and seismic tomography: *in* G. Nolet, ed. Seismic Tomography: Riedel, Dordrecht.

O'Doherty, R. F. and Anstey, N. A., 1971, Reflections on amplitudes: Geophys. Prospect., **19**, 430-458.

Petersen, N. V., 1990, Inverse kinematic problem for a random gradient medium in geometric optics approximation: Pure Appl. Geophys., **132**, 417-437.

Rio, P., Mukerji, T., Mavko, G., and Marion, D., 1995, Velocity dispersion and upscaling in a laboratory-simulated VSP: Geophysics, in press.

Roth, M., and Korn, M., 1993, Single scattering theory versus numerical modeling in two-dimensional random media: Geophys. J. Int., **112**, 124-140.

Roth, M., Müller, G., and Sneider, R., 1993, Velocity shift in random media: Geophys. J. Int., **115**, 552-563.

Shapiro, S. A., and Kneib, G., 1993, Seismic attenuation by scattering: theory and numerical results: Geophys. J. Int., **114**, 373-391.

Sobczyk, K., 1985, Stochastic Wave Propagation: Elsevier Science Publ. Co., New York

Stanke, F. E., and Burridge, R., 1993, Spatial versus ensemble averaging for modeling wave propagation in finely layered media: J. Acoust. Soc. Am., **93**, 36-41.

Sun, C. T., Achenbach, J. D., and Herrmann, G., 1968, Continuum theory for a laminated medium: J. Appl. Mech., **35**, 467-475.

Wang, Z., and Nur, A., 1992, Seismic and acoustic velocities in reservoir rocks, vol 2, theoretical and model studies: Soc. Explor. Geophys., Geophysics reprint series no. 10

Watt, J. P., Davies, G. F., and O'Connell, R. J., 1976, The elastic properties of composite materials: Rev. Geophys. Space Phys., **14**, 541-563.

Wielandt, E., 1987, On the validity of the ray approximation for interpreting delay times: *in* G. Nolet, ed., Seismic Tomography: Riedel, Dordrecht.

Wood, A. W., 1955, A Textbook of Sound: Bell, London.

Wu, R. S., and Aki, K., 1985, Elastic wave scattering by a random medium and small-scale inhomogeneities in the lithosphere: J. Geophys. Res., **90**, 10261-10273.

Zhang, L., 1993, Imaging by the wavefront propagation method: Ph. D. dissertation, Stanford.